STUDY OF SEASONAL VARIATIONS IN THERMOPHYSICAL CHARACTERISTICS OF GALE CRATER, MARS

A Thesis

Submitted in the partial fulfilment of the requirements for the award of the degree of

MASTER OF TECHNOLOGY

IN

REMOTE SENSING

BY

VIDHYA GANESH R

(MT/RS/10001/2015)

DEPARTMENT OF REMOTE SENSING

BIRLA INSTITUTE OF TECHNOLOGY

MESRA-835215, RANCHI

2017

DECLARATION CERTIFICATE

This is to certify that the work presented in the thesis entitled "**Study of Seasonal Variations in Thermophysical Characteristics of Gale crater, Mars**" in partial fulfilment of the requirement for the award of Degree of **Master of Technology in Remote Sensing** of Birla Institute of Technology, Mesra, Ranchi is an authentic work carried out under my supervision and guidance.

To the best of my knowledge, the content of this thesis does not form a basis for the award of any previous Degree to anyone else.

Date:

Dr. Mili Ghosh

(Assistant Professor and Guide)

Department of Remote Sensing

Birla Institute of Technology

Mesra, Ranchi

Head

Department of Remote Sensing

Birla Institute of Technology

Mesra, Ranchi – 835215

Dean

(Post Graduate Studies)

Birla Institute of Technology

Mesra, Ranchi – 835215

CERTIFICATE OF APPROVAL

The foregoing thesis entitled "**Study of Seasonal Variations in Thermophysical Characteristics of Gale crater, Mars**", is hereby approved as a creditable study of research topic and has been presented in satisfactory manner to warrant its acceptance as prerequisite to the degree for which it has been submitted.

It is understood that by this approval, the undersigned do not necessarily endorse any conclusion drawn or opinion expressed therein, but approve the thesis for the purpose for which it is submitted.

(Internal Examiner) **(External Examiner)**

(Chairman)

Head of the Department

ACKNOWLEDGEMENTS

I express my deep gratitude to **Dr. Mili Ghosh**, Assistant Professor, Department of Remote Sensing, Birla Institute of Technology, Mesra for her valuable guidance, sportive encouragement, and valuable suggestions throughout my course and dissertation work. I wish to put on record my deep reverence and esteemed thanks to her.

I express my sincere thanks to **Dr. A. P. Krishna**, Professor and Head, Department of Remote Sensing, Birla Institute of Technology, Mesra for extending the facilities in the department throughout my dissertation work. I am also thankful to **Dr. C. Jeganathan**, Professor, **Dr. N. Patel**, Professor, **Dr. V. S. Rathore**, Assistant Professor and **Mrs. Richa Sharma**, Assistant Professor, Department of Remote Sensing, Birla Institute of Technology, Mesra for their valuable guidance, moral support and suggestions throughout my course and dissertation work.

I also extend my sincere thanks to **Dr. Ashwin Vasavada**, Project Scientist, MSL Curiosity Team, NASA, **Dr. German Martinez**, Research Scientist, University of Michigan, **Dr. Jennifer Piatek**, Associate Professor, Geological Sciences, Central Connecticut State University, and **Dr. Hannu Savijarvi**, Research Scientist, University of Finland for taking time from their busy schedule and helping me with valuable inputs during the course of my thesis. I am extremely indebted to them for their valuable guidance.

My special thanks to all my **classmates** for their everlasting support and encouragement throughout my course and dissertation work. I also thank my **juniors** for their support in completing my dissertation work. I express earnest thanks to all the **teaching** and **non-teaching staff**, Department of Remote Sensing, Birla Institute of Technology, Mesra for their direct or indirect help during the course of study.

I also express my deep gratitude to my beloved **parents** and **sister** for their moral support and constant encouragement throughout my course and dissertation work.

VIDHYA GANESH R

ABSTRACT

Surface energy budget and thermal inertia are two major thermophysical parameters that play an important role in understanding the thermal behaviour and habitability of a planet. The estimation of surface energy balance is important to study the energy exchange processes and boundary layer dynamics of any planetary body since radiative transfer processes play a significant role in regulating the near surface thermal weather on the planet. For planetary surface materials, thermal inertia is the key property controlling the diurnal and seasonal surface temperature variations and is typically dependent on the physical properties of near-surface geologic materials. Thermal inertia, on the other hand, determines the capability of the surface to store heat.

The surface energy budget and radiative transfer of Mars is primarily dependent on the characteristics of the Martian atmosphere, which change with the change in season of the Martian year. A study of its seasonal variation would enable a greater understanding of the thermal environment in each season on Mars.

Many scientists and researchers have developed various methods and numerical models to partially compute energy budgets using various orbiter thermal infrared data. With the advancement of space technology and the landing of rovers on the Martian surface, work in the direction of understanding the thermal environment of Mars has substantially increased. Here, the best methods for efficient calculation of each surface energy budget component have been assimilated and an attempt is made to enhance computational accuracy using in situ rover observational data from MSL Curiosity across twelve sols for four locations near the Gale crater.

The amount of flux stored by the ground for conduction is thereby estimated from the equilibrium of surface energy transfer, which otherwise is difficult to compute directly. Ground heat flux is also computed by solving the one-dimensional heat conduction equation with inputs from Curiosity GTS measurements and compared with the former value to estimate thermal inertia. Thermal inertia is also calculated by running a thermal model on THEMIS thermal infrared night-time imagery and compared with the rover derived thermal inertia.

Observations reveal that the nature of variations are similar to that of Earth, except for the magnitudes of surface forcing. However, spring and autumn tend to be the seasons experiencing extreme weather conditions unlike the case with our planet. Thermal inertia from Curiosity inputs was calculated by incorporating the effects of diurnal variation of atmospheric dust opacity and wind turbulence with an uncertainty of around 8.85%. THEMIS thermal inertia was also calculated within an error of less than 20%.

However, it was also observed that thermal inertia is not constant for a particular surface with respect to time, as thought of previously. A plot of the thermal inertia at different solar longitudes at the four locations showed a sinusoidal variation of thermal inertia peaking at L_s = 95° to 100° and dipping at around L_s = 250° to 270°, roughly near the perihelion of the Martian year.

The thermal inertia generated was used to derive particle sizes to enable surface characterization of the study area using an empirical equation developed by Presley (2002). The thermal inertia ranges for different particle sizes based on USGS soil classification system at an average atmospheric pressure of 6 torr and average volumetric heat capacity of 1.3×10^{6} J m^{-3} K^{-1} were calculated and the THEMIS derived thermal inertia images were reclassified based on the ranges obtained. It was seen that the surface is covered by dust and fine sand owing to deposition during the dust seasons which gradually reduces as the global wide dust storms recede.

This study provides a rough idea of the thermal behaviour of each season on Mars and aims to help future Mars missions in efficient mission scheduling and rover design. This study could also be enhanced by using multi-dimensional thermal models and accounting for sub-surface layering of the ground so that thermal inertia can be estimated more precisely and accurately.

CONTENTS

LIST OF TABLES

LIST OF FIGURES

LIST OF ABBREVIATIONS

Acronym	**Explanation**
ATS	Air Temperature Sensor
AU	Astronomical Units
BTR	Brightness Temperature Record
CT	Coopers Town
CTX	Context Imager
GTS	Ground Temperature Sensor
HiRISE	High Resolution Imaging Science Experiment
LMST	Local Mean Solar Time
MCD	Mars Climate Database
MOLA	Mars Orbiter Laser Altimeter
MR	Mount Remarkable
MSL	Mars Science Laboratory
PDS	Planetary Data System
PL	Point Lake
PS	Pressure Sensor
RDR	Reduced Data Record
REMS	Rover Environmental Monitoring Station
TES	Thermal Emission Spectrometer
THEMIS	Thermal Emission Imaging System
TI	Thermal Inertia
TIU	Thermal Inertia Units
YKB	Yellowknife Bay

LIST OF SYMBOLS

Symbol	**Explanation**
L_s	Solar longitude
A	Albedo
S↓	Downwelling shortwave radiation
L↓	Downwelling longwave radiation
L↑	Upwelling longwave radiation
H	Sensible heat flux
λE	Latent heat flux
G	Ground heat flux (From SEB measurements)
G*	Ground heat flux (From heat conduction equation)
I	Thermal inertia
T_g	Ground temperature
T_a	Ambient air temperature
u	Windspeed
R_b	Bulk Richardson number
T_b	Brightness temperature
λ	Thermal conductivity
ρ	Surface density
C	Specific heat capacity
ρ_a	Atmospheric density
k	von Karman constant
z_a	Height at which atmospheric temperature and windspeed are recorded

z_0	Surface roughness
g	Acceleration due to gravity
μ	Cosine of solar zenith angle
z	Solar zenith angle
$\bar{r}$	Mean Sun - Mars distance
S_0	Solar irradiance at mean Sun – Mars distance
E	Solar irradiance at TOA (Top of atmosphere)
θ	Latitude
δ	Solar declination angle
h	Hour angle
p	Period of Martian solar day
L_{sp}	Solar longitude at perihelion
e	Orbit eccentricity
f (μ, τ, A)	Normalized net irradiance function
τ	Atmospheric dust opacity
T_d	Constant subsurface temperature at a depth z_d
L	Penetration depth
ω	Angular speed of planet's rotation
λ_i	Wavelength
c	Speed of light in vacuum
B_i	Spectral radiance
h_p	Planck's constant
d	Particle size
P	Atmospheric pressure

Chapter 1

INTRODUCTION

1.1 Background

Mars has been an area of extensive study for quite some time now. Mars is the fourth planet from the Sun and is the second smallest planet in the solar system. Named after the Roman god of war, Mars is also often described as the “Red Planet” due to its reddish appearance. Mars is a terrestrial planet with a thin atmosphere composed primarily of carbon dioxide. Table 1.1 describes the salient features of the planet.

Table 1.1 Salient features of Mars

Equatorial diameter	6792 km
Polar diameter	6752 km
Mass	6.42×10^{23} kg (10.7% of Earth)
Moons	2, Phobos and Deimos
Orbit distance	227,943,824 km
Orbit period	687 days (1.9 Earth years)
Surface temperature	-153 to 20°C

Mars has only 15% of the Earth’s volume and just over 10% of the Earth’s mass. Martian surface gravity is only 37% of the Earth’s. Mars is home to Olympus Mons, a shield volcano 21km high and 600km in diameter (Mars Space Facts, 2017).

1.2 Martian year and cycle of seasons

Mars has a highly elliptical orbit when compared to the Earth with an eccentricity of 25.2°. Mars has an orbit with a semimajor axis of 1.524 astronomical units (228 million kilometres) and an eccentricity of 0.0934. It orbits the Sun in 687 days and travels 9.55 AU in doing so at an average orbital speed of 24 km/s.

Martian Solar Longitude (L_s) is defined as the Mars-Sun angle at an instant, measured from the Northern hemisphere spring equinox where L_s = 0°. Consequently, L_s = 90°, L_s = 180° and L_s = 270° correspond to the summer solstice, autumnal/ vernal equinox and winter solstice for the Northern hemisphere respectively. Conversely, for the

Southern hemisphere, $L_s = 0°$, $L_s = 90°$, $L_s = 180°$ and $L_s = 270°$ represent the vernal equinox, winter solstice, spring equinox and summer solstice respectively.

Mars is closest to the Sun at $L_s = 251°$ (Perihelion) at 1.38 AU and farthest at $L_s = 71°$ (Aphelion) at 1.666 AU. For the Southern hemisphere, it is to be noted that the perihelion and aphelion occur in the spring and autumn seasons, unlike that in Earth where it occurs in the summer and winter seasons respectively (Mars Climate Database, 2017).

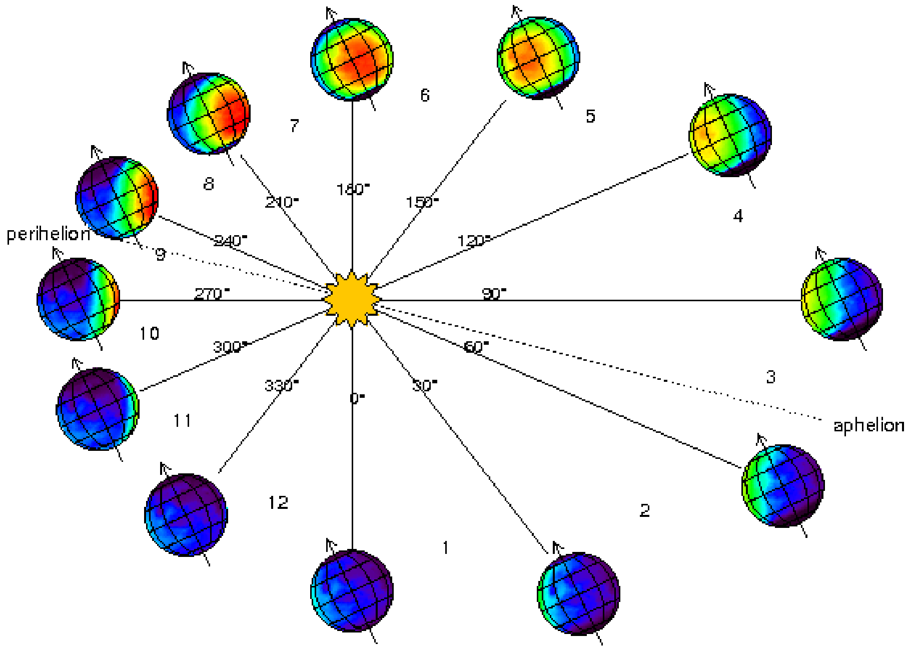

Fig 1.1 Martian seasons and Solar longitude

1.3 Energy Interactions between the Surface and the Atmosphere

Advances in space exploration require an insight into the environments of the bodies of the solar system. The study of energy interactions at the surface and sub-surface level determines the near-surface thermal environment and therefore presents a significant role in understanding the habitability and physical processes on Mars (Martinez et al., 2014).

At the surface-atmosphere interface, there is a significant amount of energy transfer taking place. The entire continuum can be divided into three components namely - space, atmosphere and surface. From Planck's radiation law, all objects having temperatures greater than 0K emit longwave radiation. Hence, emission of longwave radiation can be expected from both surface and atmosphere.

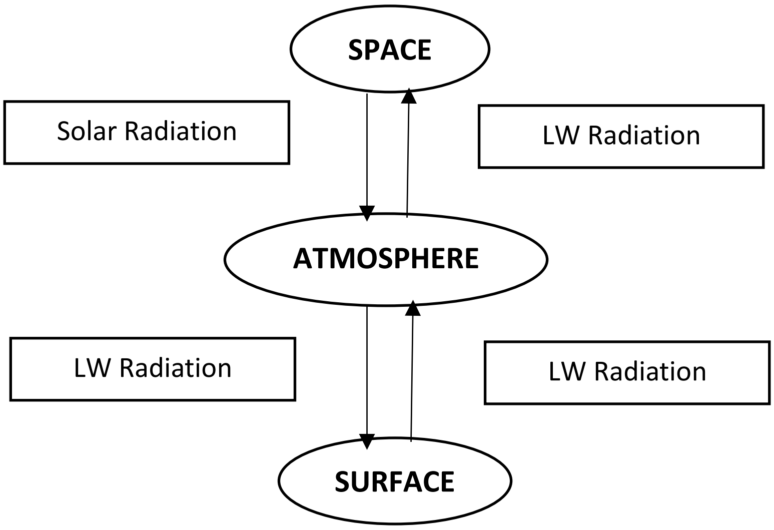

Fig 1.2 Energy interactions at the atmosphere

Consider the energy interactions taking place at the atmospheric level (Fig 1.2). The atmosphere has two sources of inward flux:

- Solar radiation
- Emitted longwave radiation from the surface

Similarly, the atmosphere also emits longwave radiation into both, the surface and space. Hence, outward fluxes from the atmospheric layer include:

- Longwave radiation emitted to the surface
- Longwave radiation emitted to space

In the case of Earth, the approximate values of these fluxes are 67W/m^2 (solar radiation absorbed by the atmosphere), 350W/m^2 (emitted longwave radiation from the surface), 324W/m^2 (Emitted longwave radiation to the surface) and 195W/m^2 (Emitted longwave radiation to the atmosphere). The net radiation at the atmospheric level is found to be -102W/m^2 (negative) which implies that energy is leaving the atmosphere (Bonan, 2002).

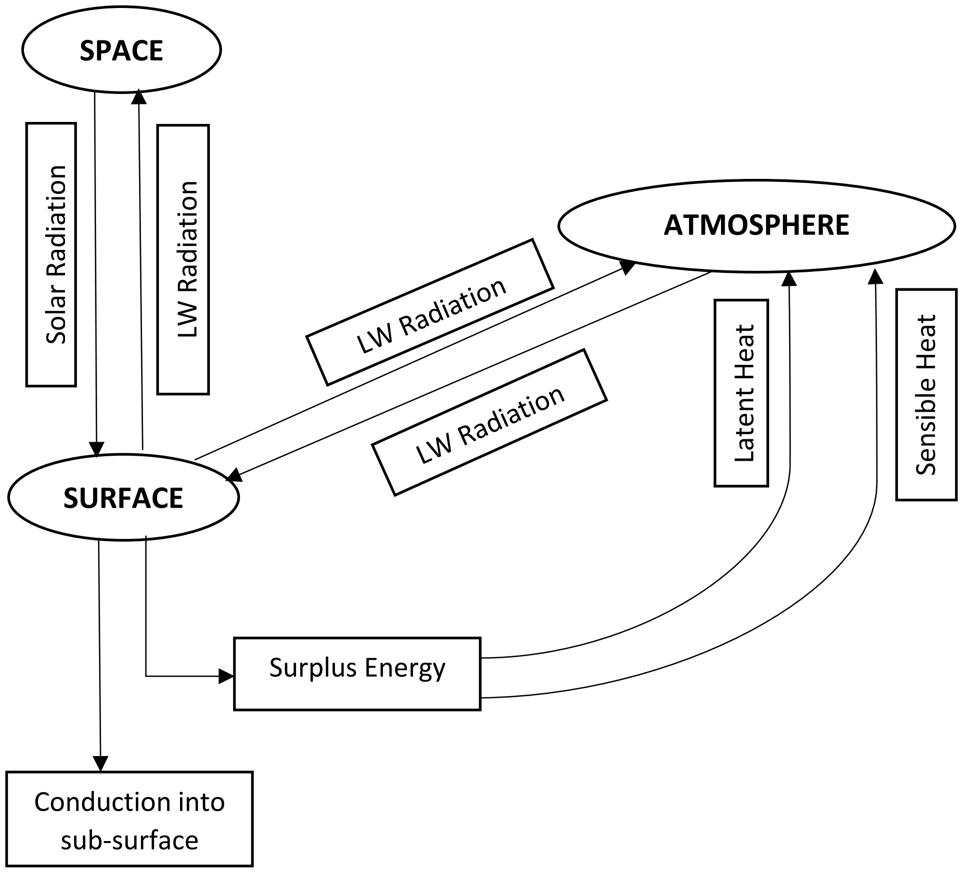

Fig 1.3 Energy interactions at the surface

Considering the energy interactions at the surface level (Fig 1.3), there are two sources of inward heat flux, namely the heat from the Sun and emitted longwave radiation from the atmosphere. Some amount of the incoming energy is passed on to the sub-surface by conduction of heat through the soil grains. The surface, owing to its temperature also emits a longwave radiation, whose magnitude is quite lesser when compared to the incoming energy at the surface from both its sources, thereby resulting in a surplus of energy at the surface. This surplus energy is returned to the atmosphere in two forms:

- Sensible heat (heat transfer from surface to atmosphere by convection)
- Latent heat (heat transfer from surface to atmosphere by change of state from liquid to vapor)

1.4 Surface Energy Budget

By law of conservation of energy, energy can neither be created nor be destroyed in a system. Hence, total incoming radiation onto the surface must be equal to the total outgoing radiation. This constitutes the basis for generation of the surface energy budget of the system.

The surface energy budget equation can be written as:

$$(1 - \mathrm{A})\mathrm{S}\downarrow + \mathrm{L}\downarrow = \mathrm{L}\uparrow + \mathrm{H} + \lambda\mathrm{E} + \mathrm{G} \quad (1)$$

where,

A – albedo of the surface

S↓ – downwelling short-wave radiation (solar radiation)

L↓ – downwelling longwave radiation (emission from atmosphere)

L↑ - upwelling longwave radiation (emission from surface)

H – sensible heat flux

λE – latent heat flux

G – heat exchange by conduction into ground

The terms on the LHS indicate incoming radiation onto the surface and those on the RHS denote energy coming out of the surface. In the case of Mars, the effect of latent heat flux is negligible (of the order of 1 W/m^2), as there is no confirmed presence of water or water vapour in the Martian surface or atmosphere. Hence, the latent heat component of the budget may be neglected (Martinez et al., 2014)

The amount of energy transferred depends on the temperatures of the surface and atmosphere, the surface composition that plays a role in regulating surface temperature diurnally and the atmospheric composition that regulates the amount of energy received by the surface.

1.5 Thermal Inertia

Thermal inertia is a measure of the sub-surface's ability to store heat during the day and re-radiate it during the night. It may be defined as the degree of slowness with which the temperature of a body approaches that of its surroundings. This would obviously control the amplitude of surface temperature variations and is closely related to the thermal conductivity of the surface. Thermal inertia is given by Eqn.2.

$$I = \sqrt{\rho\lambda C} \tag{2}$$

where,

I – thermal inertia of the surface (J m^{-2} K^{-1} $s^{-1/2}$)

ρ – density of the surface (kg m^{-3})

λ – thermal conductivity of the surface (W m^{-1} K^{-1})

C – specific heat capacity of the surface (J kg^{-1} K^{-1})

Thermal inertia of materials is closely dependent on thermal conductivity which depends upon several factors:

1. Average particle size of grains comprising the surface
2. Size and abundance of rocks on or near the surface
3. Degree of induration of duricrust
4. Exposure of underlying bedrock

Higher night time temperatures represent larger soil grains or higher abundance of rocks on the surface. This provides for greater surface area for heat absorption and the higher density of rocks when compared to fine grained particles allows greater amount of heat to be trapped in the rocks. Therefore, greater particle sizes result in greater values of thermal inertia (Christensen et al., 2001).

Thermal inertia plays a significant role in planetary remote sensing applications. For planetary surface materials, thermal inertia is the key property controlling the diurnal and seasonal surface temperature variations and is typically dependent on the physical properties of near-surface geologic materials. A rough approximation to thermal inertia is sometimes obtained from the amplitude of the diurnal temperature curve. The temperature of a material having low thermal inertia changes significantly during the day whereas that of a material having high thermal inertia does not change drastically. In remote sensing applications, thermal inertia represents a complex combination of particle size, rock abundance, bedrock outcropping and degree of hardening (Volumetric Heat Capacity, 2017).

1.6 List of various Mars missions

Mars has always been a planet of significant interest to scientists and researchers owing to its similarity to Earth. Hence, missions to survey the Red planet had begun way back in the 1960s. Thermal remote sensing of Mars became very significant when researchers wanted to gain a detailed idea of the nature of the surface, its geology, its atmosphere and various surface-atmosphere interactions.

Table 1.2 List of various thermal sensors to Mars

Sl. No	Sensor	Mission	Type	Launch Date	Launching Agency
1	Two Channel IR Radiometer	Mariner 6	Flyby	Feb 25, 1969	NASA
2	Two Channel IR Radiometer	Mariner 7	Flyby	Mar 27, 1969	NASA
3	IR Radiometer	Mars 2	Orbiter	May 19, 1971	Soviet Union
4	IR Radiometer	Mars 3	Orbiter	May 28, 1971	Soviet Union
5	Infrared Interferometer Spectrometer (IRIS)	Mariner 9	Orbiter	May 30, 1971	NASA
6	Infrared Radiometers for Thermal Mapping (IRTM)	Viking 1	Orbiter and Lander	Aug 20, 1975	NASA
7	Infrared Radiometers for Thermal Mapping (IRTM)	Viking 2	Orbiter and Lander	Sep 09, 1975	NASA

8	Thermal Emission Spectrometer (TES)	Mars Global Surveyor	Orbiter	Nov 7, 1996	NASA
9	Mars Pathfinder and Sojourner	Mars Environmental Survey Program	Lander and Rover	Dec 4, 1996	NASA
10	Thermal Emission Imaging System (THEMIS)	Mars Odyssey Mission	Orbiter	Apr 7, 2001	NASA
11	Visible and Infrared Mineralogical Mapping Spectrometer (OMEGA) and Planetary Fourier Spectrometer (PFS)	Mars Express	Orbiter	Jun 2, 2003	ESA
12	Mini-TES	MER-A (Spirit)	Rover	Jun 10, 2003	NASA
13	Mini-TES	MER-B (Opportunity)	Rover	Jul 8, 2003	NASA
14	Visible and Infrared Thermal Imaging Spectrometer (VIRTIS)	Rosetta	Gravity Assist to 67P, Churyumov/ Gerosimenko	Mar 2, 2004	ESA

15	Thermal and evolved gas analyser and Meteorological Station (MET)	Phoenix	Lander	Aug 4, 2007	NASA
16	Visible and Infrared Spectrometer (VIR)	Dawn	Gravity Assist to Ceres	Sep 27, 2007	NASA
17	Rover Environmental Monitoring Station (REMS)	Mars Science Laboratory (MSL) Curiosity	Rover	Nov 26, 2011	NASA
18	Thermal Infrared Imaging Spectrometer (TIS)	Mars Orbiter Mission	Orbiter	Nov 5, 2013	ISRO
19	Imaging Ultraviolet Spectrometer	Mars Atmosphere and Volatile Evolution missioN (MAVEN)	Orbiter	Nov 18, 2013	NASA

1.7 Significance of the Study

The surface energy budget gives an insight to the atmospheric conditions near the surface and the various energy interactions taking place there. The surface energy budget concept can be used to estimate the amount of energy passed on from the surface to the sub-surface by conduction, resulting in ground heat storage which otherwise, is difficult to measure directly. There is still no clear picture as to how the various components of the surface energy budget over the Martian surface vary with season. This work attempts to throw some light on the same. Computation of thermal inertia has been widely done using orbiter thermal imagery at medium and coarse resolutions. With availability of high resolution, near real-time ground truth data in the form of rover observations, it is possible to enhance the computational accuracy of measurement of thermal inertia. This work uses Mars Science Laboratory Curiosity rover observations to compute thermal inertia and compares the measurements with computations using available orbiter data.

1.8 Research Objectives

- To calculate surface energy budget components and study their seasonal variations.
- To calculate thermal inertia from the solution of heat conduction equation with inputs from Curiosity REMS measurements.
- To derive thermal inertia using orbiter thermal imagery and validate and assess its accuracy with Curiosity derived thermal inertia.

1.9 Organization of Thesis

Chapter 1 gives a brief introduction to the research topic and highlights the objectives of the study. In Chapter 2, review of various literature for the work is described and the research gap is highlighted. A brief description of the data used and the area under study is described in Chapter 3. The detailed methodology adopted for the study is described in Chapter 4. Results, inferences and discussions are presented in Chapter 5. Chapter 6 presents the conclusions and future scope of the work undertaken.

Chapter 2

LITERATURE REVIEW

2.1 Surface Energy Fluxes

Surface energy fluxes on Mars were previously calculated based on numerical models. Sutton et al. (1978) was among the first to calculate boundary layer parameters and energy fluxes for a non-Earth planet. He calculated sensible heat flux at the Viking lander sites whose work was subsequently improvised by Haberle et al. (1993). Haberle and Pollack et al. (1993) developed a radiative transfer model to calculate incoming solar fluxes on the Martian surface in an attempt to understand how effectively solar energy could be utilized as a power source for future Mars missions. Meadows and Crisp (1996) developed a comprehensive spectrum resolving radiative transfer model to determine net shortwave radiations on the surface. This was further improvised by Savijarvi et al. (2005) since the former was computationally extensive. Savijarvi (1999) and Savijarvi and Maattanen (2010) determined various terms of the surface energy budget at Mars Pathfinder and Phoenix lander sites.

Davy et al. (2010) calculated sensible heat flux using an alternative approach utilizing air temperature profiles and Monin-Obukhov similarity theory. A comprehensive radiative transfer model named COMMIMART to study the solar irradiance reaching the Martian surface was developed by Vicente-Retortillo et al. (2015).

Mars Climate Database, developed by Laboratoire de Meteorologie Dynamique du CNRS, Paris in collaboration with European Space Agency provides a database of meteorological fields derived from General Circulation Models (Forget et al., 1999) numerical simulations of the Martian atmosphere, validated using available satellite observations. The values given by the model is found to give results on par with conventional numerical models (Millour et al., 2015).

With the advancement of space technology and landing of rovers on the Martian surface, work in the direction of understanding the thermal environment of Mars has substantially increased. Martinez et al. (2014) computed the surface energy budget components using in situ measurements of ground and air temperatures, surface pressure and wind speed from the Rover Environmental Monitoring Station (REMS) on-board MSL Curiosity rover, in an attempt to calculate thermal inertia at the Gale crater using Curiosity measurements.

2.2 Thermal Inertia

2.2.1 Theoretical Computations

As highlighted earlier, thermal inertia is a property of significant interest to planetary remote sensing scientists. Fourier (1822) first derived the the heat conduction which he then called the thermal diffusion equation.

Wesselink (1948) first demonstrated the use of the heat conduction equation to planetary surfaces while explaining lunar temperature observations. He used the heat flux at the surface as one boundary condition and the presumption of no horizontal heat flow or no heat flow at great depths as the second boundary condition.

The heat diffusion equation was also solved by Wang et al. (2010) to obtain space-time distribution of soil temperature and soil heat flux so as to derive a relation between the two.

2.2.2 Satellite based computations

Thermal inertia has been previously calculated on regional and global levels using various orbiter thermal data. With the advances in space technology, thermal imagery could be acquired at increasing spatial resolutions right upto 100m, thereby enhancing accuracy of thermal inertia measurements.

Thermophysical measurements and mapping of Mars started right from the Mariner and the Mars missions in the early 1970s. Measurements with the 8 to 40 µm radiometers on Mars 3 and Mars 5 (Moroz and Ksanfomaliti, 1972; Ksanfomaliti and Moroz, 1975; Moroz et al., 1976) led to estimation of thermal properties which were well within the range as ascertained from the 8 to 12 µm and 18 to 24 µm measurements from Mariner 6, Mariner 7 and Mariner 9 (Neugebauer et al., 1971; Kieffer et al., 1973).

The Viking missions were among the first used to study thermophysical parameters on Mars in a detailed perspective. Kieffer et al. (1976) provided the first thermal mapping results of the Martian surface and atmosphere. He studied the diurnal variation of surface temperature in the 20 µm channel as it provided the best temperature resolution below 170 K. Kieffer et al., (1977) further extended his work and calculated thermal inertia over the Tharsis region using Viking VO-1 data. He reported thermal inertias varying from 1.6 to ~ 12 cal cm^{-2} $s^{-1/2}$ K^{-1} and generated a global thermal inertia contour map based on a grid of thermal inertia values computed for 2° latitude x 2° longitude bins. Large continent like regions of low thermal inertia were observed and they were most likely attributed to deposits of loose unconsolidated air fall dust. However, the thermal model developed by Kieffer et al. (1977) failed to include the total radiative effect of clouds, non-Lambertian emission, latent heat of water ice, subsurface inhomogeneity and variable conductance at air-surface boundary.

Jakosky et al. (2000) presented the preliminary results for data obtained from the science-phasing orbit at coarse resolution and compared them with Viking results. Initial global results from the mapping orbit, including a global map and a high-resolution analysis was discussed by Mellon et al. (2000) and more detailed analysis on regions of exobiological relevance was described by Jakosky and Mellon (2001). The thermal inertia model developed by Mellon et al. (2000) relied on finding the thermal inertia that produces model temperatures that best fit TES single night-time temperature measurements. The global map discussed by Mellon et al. (2000) was obtained by binning thermal inertia values derived from the first six months of the mapping mission to a spatial resolution of roughly 0.25° in latitude and longitude.

Christensen et al., (2001) generated thermal inertia from the Thermal Emission Spectrometer data onboard the Mars Global Surveyor on a global scale at 3 km spatial resolution. He plotted TES derived bolometric albedo with thermal inertia and obtained three modes. He predicted that low thermal inertia and high albedo correspond to dusty areas and those having intermediate values of thermal inertia and albedo may be areas having well indurated duricrust (Jakosky and Christensen, 1986; Presley and Arvidson, 1988, Christensen and Moore, 1992). Christensen et al. (2001) also determined the Petitt wind streak, Coprates Chasma in Valles Marineris and Kasei Valles and ascertained that floors of low lying topographic features like catastrophic outflow channels, Valles Marineris and large impact craters in the Southern hemisphere were regions of high thermal inertia with inputs from observations made by Zimbelman and Kieffer, (1979), Christensen and Kieffer, (1979) and Edgett and Christensen, (1991).

Mena-Fernandez (2005) described a detailed method of applying thermal correction on a THEMIS dataset and thereby generate surface temperature layers, describing its structure and processing software. Fergason et al. (2006) calculated thermal inertia from THEMIS data with 20% accuracy and 10-15% precision at Tharsis, Nili Patera and Ares Vallis regions using the KRC model. THEMIS single temperature measurements were used to derive thermal inertia. The KRC model was a development to the Viking thermal model developed by Kieffer et al. (1977) with the constant atmospheric thermal radiation being replaced with a one-layer atmosphere that is spectrally grey at solar wavelengths. Direct and diffuse illuminations were computed using a two-stream delta-Eddington model. THEMIS Band 9 temperatures were converted into thermal inertia by interpolation within a six-parameter lookup table which included latitude, local solar time, atmospheric dust opacity, elevation, atmospheric pressure and albedo.

Putzig et al. (2005) and Putzig et al. (2007) studied the thermal inertia and surface heterogeneity of Mars on a global perspective and in different solar longitudes to obtain a seasonal perspective of thermal inertia using MGS TES data. He found that at mid latitudes (60°S to 60°N), seasonal maps show a general sinusoidal trend of thermal inertia in time, with a night-side maximum near L_s = 110° and minimum near L_s = 260° and a dayside maximum near L_s = 220° and minimum near L_s = 0°.

2.3 Research Gaps

It is to be noted that many models have been developed to calculate components of the surface energy budget. However, the variation of these components on a seasonal timescale is yet to be determined. In the present research, an attempt is made to study this variation and understand the factors influencing the same.

An attempt is also made to generate high resolution thermal inertia using Curiosity REMS measurements using the procedure adopted by Martinez et al. (2014). Accuracy assessment of orbiter derived thermal inertia with respect to in-situ rover observational data is also presented in this work. Seasonal trends of thermal inertia on a global scale was studied by Putzig et al. (2005) using coarser resolution TES data (3 km). This study is attempted to be made using a comparatively finer resolution THEMIS data and possible reasons for the variation is discussed.

Chapter 3

STUDY AREA AND DATA PRODUCTS

3.1 Study Area

The current study deals with a crater in the equatorial region of the southern hemisphere of Mars, namely the Gale crater. Gale is a crater on Mars near the north-western part of the Aeolis quadrangle at 5.4°S 137.8°E. It is 154 km (96 mi) in diameter and estimated to be about 3.5-3.8 billion years old.

The crater was named after Walter Frederick Gale, an amateur astronomer from Sydney, Australia, who observed Mars in the late 19th century. Aeolis Mons is a mountain in the centre of Gale and rises 5.5 km (18,000 ft) high. Aeolis Palus is the plain between the northern wall of Gale and the northern foothills of Aeolis Mons. Peace Vallis, a nearby outflow channel, 'flows' down from the Gale crater hills to the Aeolis Palus below and seems to have been carved by flowing water. The NASA Mars rover, Curiosity, of the Mars Science Laboratory (MSL) mission, landed in "Yellowknife" Quad 51 of Aeolis Palus in Gale at 05:32 UTC August 6, 2012. NASA named the landing location Bradbury Landing on August 22, 2012. Curiosity is expected to explore Aeolis Mons and surrounding areas (Gale (crater), 2017)

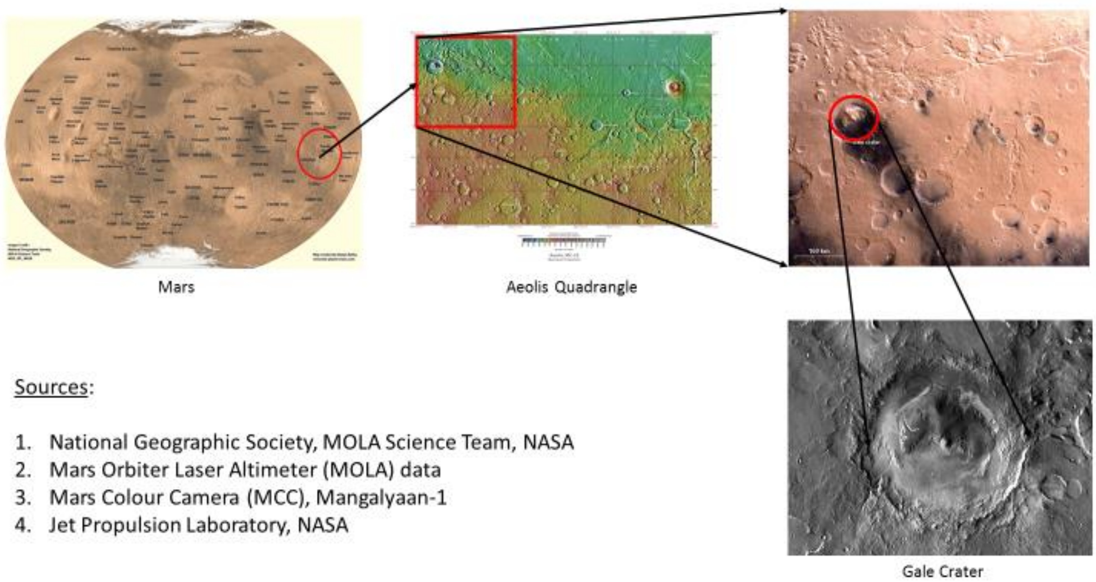

Fig 3.1 Location of Gale crater

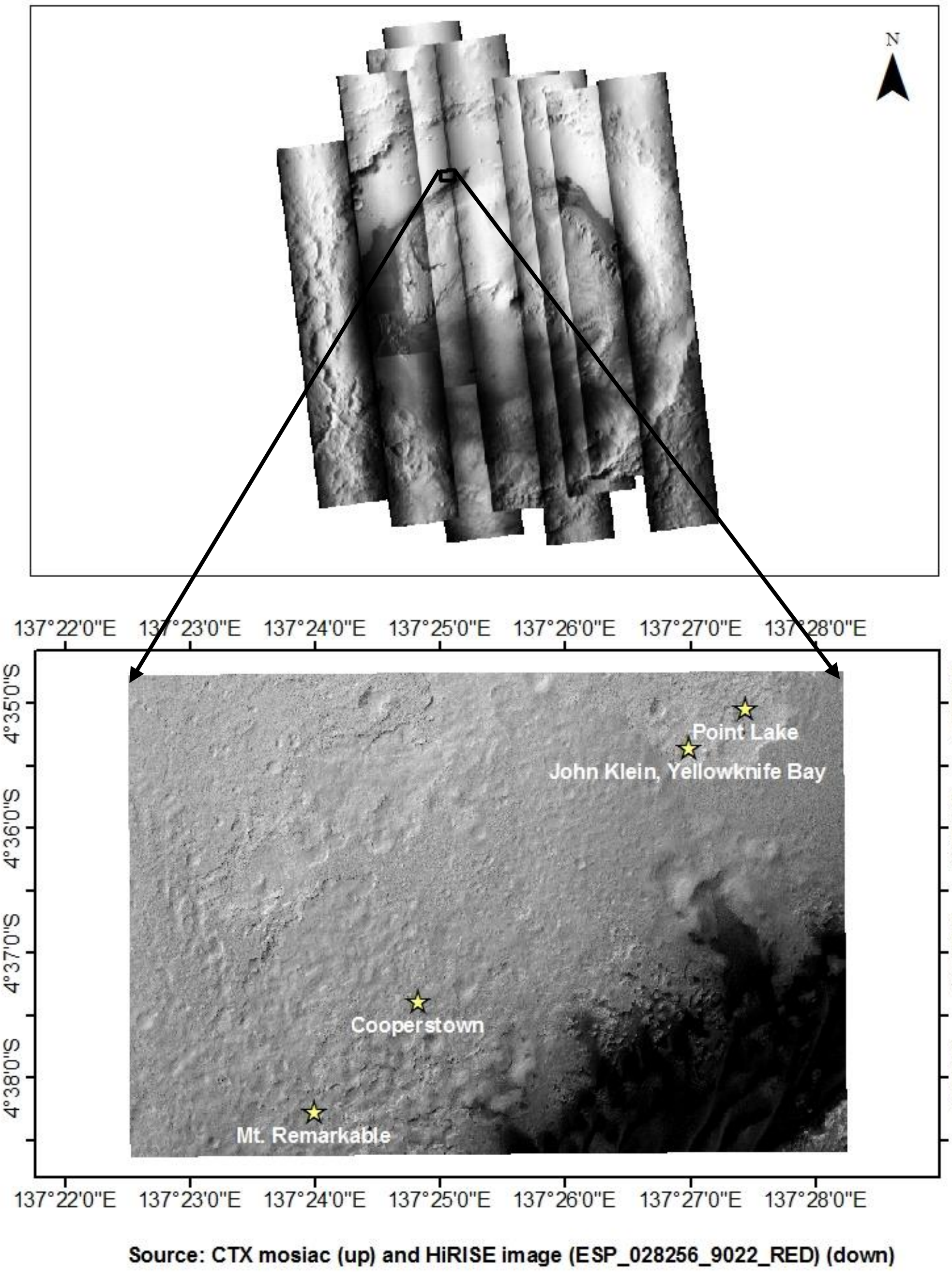

Fig 3.2 Location map of the sols chosen for study

3.2 Time of Study

The study is conducted for twelve Martian sols, namely Sol 108, Sol 110, Sol 112, Sol 234, Sol 251, Sol 270, Sol 440, Sol 441, Sol 443, Sol 610, Sol 620 and Sol 631. These sols were carefully chosen based on two major considerations:

3.2.1 Solar longitude

A Martian year is divided into four seasons – spring, summer, autumn and winter, each comprising of three months. The division of seasons is not based on number of days but based on the solar longitudes (Mars Climate Database, 2017). The division of a Martian year into months and thereby seasons in the Southern hemisphere and the grouping of Curiosity sol numbers into different months for the first year of Curiosity observations is also shown in Table 3.1.

Table 3.1 Martian months and seasons

Month	Season in Southern Hemisphere	L_s (°)	Duration (sols)	Remarks	Curiosity Sols
1	Autumn	0-30	61.2	Equinox at $L_s = 0°$	352 – 413
2		30-60	65.4		414 – 479
3		60-90	66.7	Aphelion at $L_s = 71°$	480 – 547
4	Winter	90-120	64.5	Solstice at $L_s = 90°$	548 – 613
5		120-150	59.7		614 - 674
6		150-180	54.4	Dust storm season begins	0 – 53
7	Spring	180-210	49.7	Equinox at Ls = 180° Dust storm season	54 - 102
8		210-240	46.9	Dust storm season	103 - 150
9		240-270	46.1	Perihelion at $L_s = 250°$	151 – 196

10	Summer	270-300	47.4	Solstice at $L_s = 270°$ Dust storm season	197 – 243
11		300-330	50.9	Dust storm season	244 – 295
12		330-360	55.7	Dust storm season ends	296 - 351

To provide a better and effective representation of each season, the sols were chosen to lie in the 2nd month of each 3-month season period, when peak characteristics of each season are experienced.

3.2.2 Movement of the rover

More accurate measurements of environmental parameters are possible when the rover is stationary as the velocity of the rover, if in motion and instantaneous change in location of the rover within the sol would give reason for ambiguity. Hence, the drive log of the Curiosity rover is used to select sols wherein the rover is stationary so that rover measurements are of high confidence level and are of a particular location alone.

The rover was found to be stationary between Sol 102 – 111 at Point Lake, Sol 133 – 297 at Yellowknife Bay, Sol 440 – 453 at Coopers Town and Sol 609 – 630 at Mt. Remarkable from the Curiosity rover drive log (Curiosity Rover Drive Log, 2017).

The locational information and other details of the sols chosen for the study is described in Table 3.2 and Table 3.3 respectively.

Table 3.2 Locational information of the sols chosen for study

Sols	Latitude	Longitude	Location
108, 110, 112	4°35’2.57’’S	137°27’25.89’’E	Point Lake
234, 251, 270	4°35’21.55’’S	137°26’58.69’’E	John Klein, Yellowknife Bay
440, 441, 443	4°37’23.37’’S	137°24’48.76’’E	Coopers Town
610, 620, 631	4°38’16.25’’S	137°23’58.81’’E	Mt. Remarkable

Table 3.3 Details of the sols chosen for study

Sol	Earth Date	Solar Longitude L_s (°)	Distance to Sun (A.U)	Season
108	23/11/2012	212	1.40837	Spring
110	25/11/2012	213.4	1.40674	
112	27/11/2012	214.3	1.40516	
234	30/03/2013	291.7	1.41024	Summer
251	15/04/2013	301.3	1.42507	
270	04/05/2013	312.4	1.44552	
440	21/10/2013	38.5	1.63936	Autumn
441	22/10/2013	39	1.64006	
443	24/10/2013	39.9	1.64143	
610	09/04/2014	113.9	1.62179	Winter
620	19/04/2014	118.5	1.61254	
631	30/04/2014	123.8	1.60153	

The Earth date – Mars date conversions and solar longitude for the chosen sols of study was obtained from Mars Climate Database v5.2. The Mars-Sun distance for each of these days is obtained from Planetary Ephemeris Data 2012, 2013 and 2014, courtesy of Dr. Fred Espenak (Geocentric Ephemeris for the Sun, Moon and Planets, 2017).

3.3 Data products used

3.3.1 Curiosity rover measurements

Curiosity was launched from Cape Canaveral on November 26, 2011, at 15:02 UTC aboard the MSL spacecraft and landed on Aeolis Palus in Gale Crater on Mars on August 6, 2012, 05:17 UTC. The Bradbury Landing site was less than 2.4 km (1.5 mi) from the centre of the rover's touchdown target after a 563,000,000 km (350,000,000 mi) journey (Curiosity (rover), 2016).

The rover's goals include: investigation of the Martian climate and geology; assessment of whether the selected field site inside Gale Crater has ever offered environmental conditions favourable for microbial life, including investigation of the role of water; and planetary habitability studies in preparation for future human exploration.

The various sensors built into Curiosity are as follows:

- Mast Camera (MastCam) – 2nos.
- Chemistry and Camera complex (ChemCam) – 1no.
- Navigation cameras (NavCams) – 4nos.
- Rover Environmental Monitoring Station (REMS)
- Hazard avoidance cameras (HazCams) – 8 nos.
- Mars Hand Lens Imager (MAHLI) – 1 no.
- Alpha Particle X-ray Spectrometer (APXS)
- Chemistry and Mineralogy (CheMin)
- Sample Analysis at Mars (SAM)
- Dust Removal Tool (DRT)
- Radiation assessment detector (RAD)
- Dynamic Albedo of Neutrons (DAN)
- Mars Descent Imager (MARDI) – 1no.

The sensor used for the present study is the **Rover Environmental Monitoring Station and MastCam**. The Rover Environmental Monitoring Station (REMS) investigates environmental factors directly tied to current habitability at the Martian surface during the Mars Science Laboratory (MSL) mission. Three major habitability factors are addressed by REMS: the thermal environment, ultraviolet irradiation, and water cycling. REMS is composed of four units: Boom 1, Boom 2, Ultraviolet Sensor (UVS) and Instrument Control Unit (ICU). Boom 1 accommodates a Wind Sensor (WS), an Air Temperature Sensor (ATS) and the Ground Temperature Sensor (GTS), while Boom 2 accommodates a Humidity Sensor (HS) along with a second Wind Sensor and Air Temperature Sensor. The ICU includes the instrument electronics and the Pressure Sensor (PS) (Gómez-Elvira et al., 2012).

For the present study, measurements from Ground Temperature Sensor, Air Temperature Sensor and Pressure Sensor are used. Since measurements from Wind Sensor are not available, to present the worst-case scenario, maximum and minimum wind speeds obtained during calibration of the sensor are used.

3.3.1.1 Structure of the Curiosity REMS dataset

Curiosity REMS RDRs are ASCII formatted tables that contain instrument's processed data. Each RDR file contains data of every sensor. There are several RDRs for various reduction levels. The most processed RDRs contain physical magnitudes measured by REMS with necessary corrections applied: wind speed and direction, air temperature, ground temperature, ultraviolet radiation, humidity and pressure.

In addition to the highest-level data product, two intermediate processing levels are also provided. An effort has been made to integrate results from all sensors in each RDR, in order to facilitate data analysis. However, the complexity of data processing is not the same for all sensors, so there are a greater number of transformations between RDR types for some sensors compared to others. The RDRs provided are:

TELRDR (Thermal and Electrical RDR)

This is the result of the first processing step. It contains data where counts recorded by the instrument have been converted to thermal and electrical values using calibration information. Temperatures for PT1000 sensors are given instead of resistances since the conversion between them is straightforward and temperatures are more helpful.

ENVRDR (Environmental Magnitudes RDR)

ENVRDRs are the second processing step. At this level, data has been converted from electrical to environmental magnitudes provided by each engineering sensor (e.g. data for each air temperature PT1000 sensor instead of a unique air temperature, or data for each ground temperature sensor thermophile instead of a unique ground temperature). Minimal corrections exist for some sensors to compensate their degradation due to exposure to Martian conditions.

MODRDR (Models RDR)

This level is the third and final processing level. It contains data where ENVRDRs are corrected and modelled to provide a best estimate of the environmental magnitudes. Numerous tests and data analysis have been done to ensure that their value is as accurate as possible within the project constrains.

ADR (Ancillary Data Record)

The Ancillary Data Record provides the additional data required for producing the highest level RDRs, such as rover location data (from NAIF) and the signal attenuation caused by dust deposited over the ultraviolet sensor. The sources of these data are external to REMS.

For this study, the **MODRDR** data product is used. The REMS instrument is a meteorological suite of sensors designed to provide measurements of air and ground temperatures, wind speed and direction, pressure, humidity and ultraviolet radiation.

The REMS MODRDR data set contains processed REMS data converted to environmental magnitudes and corrected by factors having an influence in the measurements (such as rover heat sources, shadows and dust, among others). The corrections at this level have been applied either by models, by removing invalid data, or by selecting the most representative data (e.g. minimum of several sensors). In the case of the Wind Sensor, modelling includes not only corrections but also the estimation of the wind data itself. All the original data can be found in the previous processing levels. Data is a time ordered sequence of rows organized into a table, taken at a maximum resolution of one second. Each data product contains one sol worth of activity and has information from all sensors. Like in the ENVRDR there is a confidence level code for each sensor.

This data set is the highest processing level produced by the REMS team. It should be of interest to anyone wanting to know Mars environmental information at the rover's location.

This data set includes the following information:

Table 3.4 Structure of Curiosity REMS MODRDR data

Columns	Description of data contained
1 - 3	**Time References**: REMS clock, Local Mean Solar Time (LMST) and Local True Solar Time (LTST)
4 - 7	**Wind Sensor**: horizontal and vertical wind speed, wind direction
8 - 11	**Ground Temperature Sensor**: brightness temperature of thermopile A (band 8-14 um) and its estimated uncertainty
12 - 17	**Air Temperature Sensor**: local air temperature around each boom and an estimated ambient temperature around the rover, calculated after a filtering of both local air temperatures
18 – 30	**Ultraviolet Sensor**: ultraviolet radiation for each band and their estimated uncertainties
31 – 37	**Humidity Sensor**: local relative humidity, volume mixing ratio, their estimated calibration uncertainties and the sensor operating temperature
38 - 40	**Pressure Sensor**: pressure and its uncertainty, pressure sensor configuration (oscillator and low/high resolution mode)

Sampling is at 1Hz maximum, with a baseline operation of 5 minutes every hour. Additional measurements can be taken on an on-demand basis beyond those hourly observations. For these additional measurements, and besides tactical day to day conditions and resources, there is a general pattern that covers selected hours of the day built by the scientific team during operations. That pattern is shifted from sol to sol to cover the whole 24 hours after a few sols. Additionally, extended measurements can also be triggered automatically if event mode is activated, in which case the REMS computer will decide or not to continue measuring after the regular cadence, by comparing the previous measurements with the expected trend. The objective is to capture any ongoing transitory atmospheric event.

During the first 72 sols, for each 5-minute block, the following measurement strategy was used: Wind Sensor is switched off for 60 seconds, then it is switched on for 235 seconds, and then it is switched off again for the final 5 seconds. The rest of the sensors are switched on all the time. This strategy was based on results obtained during pre-flight testing. However, after evaluating flight data, it was determined that this strategy was not necessary, so from sol 73 onwards all sensors are switched on for each 5-minute block.

From sol 793 onwards, a new measurement strategy for Humidity Sensor was introduced. It is called HS HRIM (Humidity Sensor High Resolution Interval Mode) and is only used on selected one-hour long observations. This new strategy intends to minimize heating of the Humidity Sensor, and consists of alternately switching on and off the sensor at periodic intervals. At the same time, Boom 2 is switched off, which means that there are no Wind Sensor and Air Temperature Sensor measurements. Curiosity REMS data can be downloaded from PDS Geosciences Node.

3.3.2 THEMIS imagery

The Thermal Emission Imaging System (THEMIS) captures images in the infrared portions of the electromagnetic spectrum to obtain thermal properties of the Martian surface. It detects thermal infrared energy emitted by the Martian surface in 10 bands (nine different wavelengths), of which 8 bands are in the 6 µm to 13 µm range (Thermal Infrared range) and one at 14.9 µm (CO_2 absorption band) to monitor Mars' atmosphere.

The shortest infrared wavelength band (6.78 µm) is measured twice to improve the Peak Signal to Noise Ratio (PSNR) (Burch, 2009). The spatial and spectral resolutions of the various THEMIS bands are given in Table 3.5.

Table 3.5 THEMIS band information

Band No.	Central Wavelength (μm)	Spatial Resolution (m)
1	6.62	100
2	6.62	100
3	7.88	100
4	8.56	100
5	9.30	100
6	10.11	100
7	11.03	100
8	11.78	100
9	12.58	100
10	14.96	100

THEMIS was primarily used to locate potential landing sites for the Mars Exploration Rovers (Spirit and Opportunity). Hence, it does not have systematic pole to pole coverage like TES usually has. However, where full 10 band IR images are taken, atmospheric properties can be retrieved regardless of the primary purpose of taking the image at a certain location.

3.3.2.1 Structure of the THEMIS dataset

THEMIS datasets are collected as QUBE objects, which comply with the Planetary Data System (PDS) standards. A QUBE is an array of sample values in two dimensions. The "core" of a THEMIS QUBE is three-dimensional, with two spatial dimensions (samples and lines) and one spectral dimension (bands). The QUBE format allows THEMIS data to simultaneously a set of images (at different wavelengths) of the same target area, and also a multi-point spectrum at each spatially registered pixel target area.

Additional information may be stored in “suffix” planes (back, side, or bottom) as conceptually depicted in Figure 3.3 (Selene, 2005).

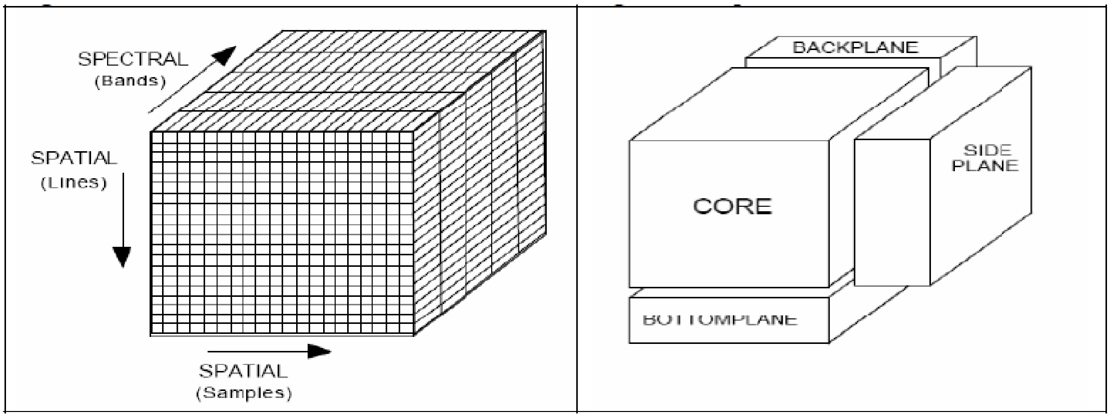

Fig 3.3 QUBE data structure of THEMIS IR data

THEMIS IR data exist as different records based on their level of processing:

EDR (Experiment Data Record)

This file contains the raw THEMIS science data at the full resolution returned from the spacecraft, time ordered with duplicates and transmission errors removed. This file is a PDS SPECTRAL_QUBE object with an attached PDS label.

RDR (Reduced Data Record)

This file contains the radiometrically calibrated version of the THEMIS EDR standard data products. This file is a PDS SPECTRAL_QUBE object with an attached PDS label.

BTR (Brightness Temperature Record)

The BTR is derived from Band 9 of a IR RDR QUBE (or first available band of the highest calibration product available).

THEMIS IR data can be downloaded from PDS Geosciences Node, THEMIS Image Explorer or Planetary Image Locator Tool (PILOT).

3.3.3 Other auxiliary data used

3.3.3.1 Mars Orbiter Laser Altimeter Digital Elevation Model (MOLA–DEM)

The DEM represents more than 600 million measurements gathered between 1999 and 2001, adjusted for consistency (Neumann et al., 2001; Neumann et al., 2003) and converted to planetary radii. These have been converted to elevations above the areoid as determined from a Martian gravity field solution GMM-2B (Lemoine et al., 2001), truncated to degree and order 50, and oriented according to current standards. The MOLA measurements were converted into a digital elevation model (Neumann et al., 2001; Smith et al., 2001) using Generic Mapping Tools software (Wessel and Smith, 1998), with a resolution of 128 pixels per degree. In projection, the pixels are 463 meters in size at the equator.

3.3.3.2 MGS TES Global Albedo Mosaic

The Mars Global Surveyor Thermal Emission Spectrometer (TES) acquired a variety of observations, including broadband visible/near-IR data (0.3 to 2.9 µm) and broadband thermal IR data (5.1 to 150 µm) using bolometers, in addition to spectrometer observations covering 5.8 to 50 µm in wavelength (Christensen et al., 2001). The VISIR data have been reduced to Lambert albedo values and gridded at 8 pixels/degree.

3.3.3.3 Context Imager (CTX)

The Mars Reconnaissance Orbiter (MRO) Context Camera (CTX) is currently orbiting Mars and acquiring grayscale (black & white) images at 6 meters per pixel scale over a swath 30 kilometres wide. CTX provides context images for the MRO HiRISE and CRISM, is used to monitor changes occurring on the planet, acquires stereo-pairs of select, critical science targets, and has (as of February 2010) covered more than 50% of the planet. Here CTX images are used for better visualization of the study area.

3.3.3.4 High Resolution Imaging Science Experiment (HiRISE)

High Resolution Imaging Science Experiment is a camera on board the Mars Reconnaissance Orbiter. The instrument was built under the direction of the University of Arizona's Lunar and Planetary Laboratory by Ball Aerospace & Technologies Corp. It consists of a 0.5 m (19.7 in) aperture reflecting telescope, the largest so far of any deep space mission, which allows it to take pictures of Mars with resolutions of 0.3 m/pixel (about 1 foot), resolving objects below a meter across. HiRISE has imaged Mars landers on the surface, including the ongoing Curiosity and Opportunity rover missions (Lunar and Planetary Science Laboratory, 2017). Here HiRISE images are used to accurately locate our points of study and get a brief idea of the geologic features near the study area.

3.3.3.5 Curiosity Drive Log

The Curiosity drive log is used to determine the days on which Curiosity was stationed at a particular location. More accurate measurements of environmental parameters are possible when the rover is stationary as the velocity of the rover, if in motion and instantaneous change in location of the rover within the sol would give reason for uncertainty in rover measurements.

3.4 Software used

3.4.1 THMPROC (THEMIS Processing web interface)

THMPROC is a web based interactive tool that greatly simplifies THEMIS data processing, while eliminating the need for users to install a software by using the THEMIS data processing system at Arizona State University. It is compatible with Firefox 1.x, Microsoft Internet Explorer 6.x, Netscape 7, Safari 1.3 browsers (and higher versions). THEMIS radiance images can be obtained in ISIS cube format via THMPROC website using rectify, deplaid and unrectify options. THMPROC is essentially used for pre-processing of THEMIS data.

3.4.2 ENVI Classic 5.1 + IDL

ENVI (an acronym for "ENvironment for Visualizing Images") is a software application used to process and analyze geospatial imagery. It is commonly used by remote sensing professionals and image analysts.

ENVI bundles together several scientific algorithms for image processing a lot of which are contained in automated, wizard-based approach that walks users through complex tasks. It was originally developed by Better Solutions Consulting, LLC, a partnership of five individuals in Boulder, CO. IDL (Interactive Data Language), is a programming language used for data analysis. It is used in particular areas of science, such as astronomy and medical imaging. ENVI supports a huge variety of image file formats thus making it a compact and robust software for remote sensing analysts.

ENVI is used in this study to run the thermal model on THEMIS images and subsequently generate thermal inertia. It is also used to visualize PDS images as captured by Curiosity (Mastcam, Navcam, etc.).

3.4.3 MS Office

The Access and Excel packages of MS Office have been extensively used in this study. The Access package is used to recover Curiosity REMS RDRs which are essentially ASCII formatted tables. The Excel package is used to perform calculations and plot ascertained variations of various parameters.

3.4.4 Mars Climate Database v5.2

The Mars Climate Database (MCD) is a database of atmospheric statistics compiled from state-of the art Global Climate Model (GCM) simulations of the Martian atmosphere. The GCM computes in 3D, the atmospheric circulation taking into account radiative transfer through the gaseous atmospheres as well as through dust and ice aerosols, includes a representation of the CO_2 ice condensation and sublimation on the ground and in the atmosphere, simulates the water cycle (with modelling of cloud microphysics), the dust multisize particle transport, the atmospheric composition controlled by the photochemistry and the local non-condensable gas enrichment and depletion induced by CO_2 condensation and sublimation. It has been extended into the thermosphere and model the ionospheric processes (Millour et al, 2015).

The model used to compile the statistics has been extensively validated using available observational data and aims at representing the current best knowledge of the state of the Martian atmosphere given the observations and the physical laws which govern the atmospheric circulation and surface conditions on the planet. The Mars Climate Database access software adds several capabilities to better represent the Martian environment variability and accurately compute the surface pressure at high spatial resolution.

Mars Climate Database v5.2 is used in the present study to calculate downwelling longwave radiations and ascertain the diurnal variation of dust optical depth for the chosen sols of study.

3.4.5 QGIS 2.18.1

QGIS (previously known as Quantum GIS) is a cross-platform free and open-source desktop geographic information system (GIS) application that provides data viewing, editing, and analysis. QGIS functions as geographic information system (GIS) software, allowing users to analyze and edit spatial information, in addition to exporting graphical maps. QGIS supports both raster and vector layers; vector data is stored as either point, line, or polygon features. Multiple formats of raster images are supported, and the software can georeference images.

QGIS supports shapefiles, coverages, personal geodatabases, dxf, MapInfo, PostGIS, and other formats. Web services, including Web Map Service and Web Feature Service, are also supported to allow use of data from external sources. QGIS integrates with other open-source GIS packages, including PostGIS, GRASS GIS, and MapServer. Plugins written in Python or C++ extend QGIS's capabilities. Plugins can geocode using the Google Geocoding API, perform geoprocessing using fTools, which are similar to the standard tools found in ArcGIS, and interface with PostgreSQL/PostGIS, SpatiaLite and MySQL databases.

The ISIS and PDS image cube formats are not supported by ERDAS Imagine and ENVI. The Semi-Automatic Classification plugin in QGIS 2.18.1 is used to open the cube datasets and convert them into a format like .tiff that can be widely used across multiple platforms.

3.4.6 ArcMap 10.1

ArcGIS is a geographic information system (GIS) for working with maps and geographic information. It is used for: creating and using maps; compiling geographic data; analyzing mapped information; sharing and discovering geographic information; using maps and geographic information in a range of applications; and managing geographic information in a database. ArcMap 10.1 is used primarily for map generation and data visualization in this study.

3.4.7 Erdas Imagine 2014

ERDAS Imagine is a remote sensing application with raster graphics editor abilities designed by ERDAS for geospatial applications. Imagine is aimed mainly at geospatial raster data processing and allows users to prepare, display and enhance digital images for mapping use in geographic information system (GIS) and computer-aided design (CAD) software. It is a toolbox allowing the user to perform numerous operations on an image and generate an answer to specific geographical questions.

Erdas Imagine is used for mosaicking of CTX imagery and also to extract thermal inertia values at the locations of study from the processed THEMIS thermal inertia image.

Chapter 4

METHODOLOGY

The entire methodology adopted for the study may be classified into different segments:

- Determination of surface energy budget from Curiosity REMS measurements and study the seasonal variations of each component of the budget.
- Calculation of thermal inertia from Curiosity measurements
- Processing of THEMIS images to generate thermal inertia layers and compare their values with those determined using Curiosity measurements.

Fig 4.1 describes the detailed methodology adopted for the study.

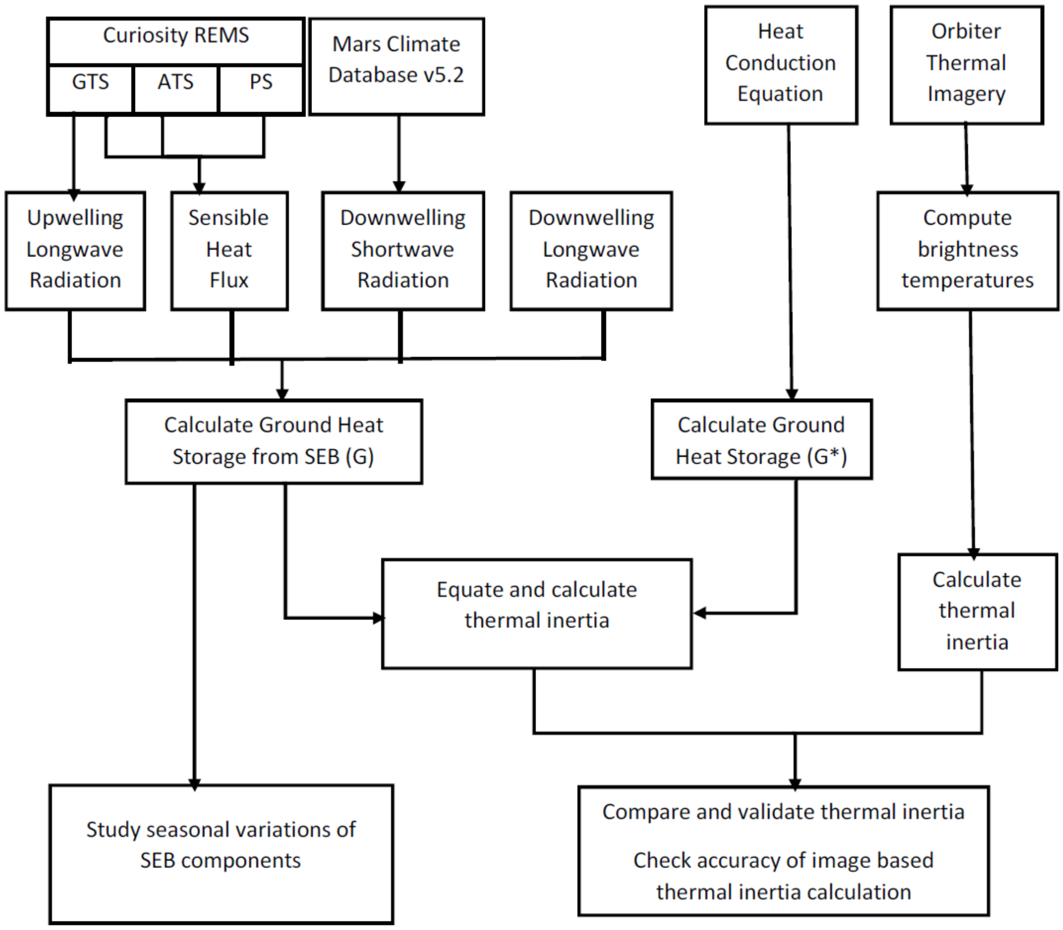

Fig 4.1 Methodology adopted for the study

4.1 Determination of Surface Energy Budget from Curiosity measurements

4.1.1 Upwelling Longwave Radiation

The surface of Mars behaves as a grey body and radiates longwave radiation owing to its temperature. This amount of longwave radiation emitted by the surface to the atmosphere can be quantified using Stefan-Boltzmann law.

$$L\uparrow = \varepsilon\sigma T_g^4 \tag{3}$$

where,

$L\uparrow$ - upwelling longwave radiation (emission from surface) (W/m^2)
ε – surface emissivity
σ – Stefan-Boltzmann constant (=5.67×10^{-8} W m^{-2} K^{-4})
T_g – ground temperature (K)

The values of ground temperature T_g is determined from measurements made by the Ground Temperature Sensor (GTS) housed in Rover Environmental Monitoring Station (REMS) on-board Curiosity rover. The surface emissivity is varied from 0.9 to 1 to determine the upper and lower bounds of the magnitude of upwelling longwave energy (Martinez et al., 2014)

4.1.2 Downwelling Longwave Radiation

Martinez et al. (2014) calculated downwelling longwave radiation based on a radiative transfer model developed by Savijarvi et al. (2005). The downwelling longwave radiation for the same sol as calculated by Martinez et al. (2014) was recalculated by running the Mars Climate Database v5.2 model. The values obtained by the latter were found to be in par with the values obtained by Martinez et al. (2014), with an error not exceeding 5%.

Hence, for this study, downwelling longwave radiations were calculated using the Mars Climate Database v5.2. Since the results are based on a statistical model, there exists only one value of this component unlike the two limiting values of the other components of the energy budget.

4.1.3 Sensible Heat Flux

Sensible heat refers to the heat carried by movement of air. The process by which heat is transferred from the surface to the overlying atmosphere by the moving air over the surface is called convection and the amount of heat thus exchanged is called sensible heat flux.

This type of exchange is like an electrical network, wherein current flows between two points having a potential difference. Now, if current has to flow between two points, it depends upon two factors:

- Potential difference (Greater the potential difference, more will be the flow of current)
- Resistance along the path (Greater the resistance to flow of current along the path, lesser will be the amount of current flowing)

Similarly, in this scenario, the sensible heat flux is directly proportional to the temperature difference between the surface and surrounding air and inversely proportional to a transfer resistance. The transfer resistance is an aerodynamic resistance to heat and represents a turbulent process.

As the particles of air move over the surface, they carry with them their heat, moisture and momentum. Wind mixes air and transports heat and water vapor in relation to the temperature and moisture of the parcels of the air being mixed (Bonan, 2002).

The sensible heat can thereby be formulated as:

$$H = \rho C_p \frac{(T_g - T_a)}{R_{th}} \qquad (4)$$

where,

H – sensible heat flux (W/m^2)

ρ – atmospheric density (kg/m^3)

C_p – specific heat of the atmospheric constituents at constant pressure ($J\ kg^{-1}\ K^{-1}$)

T_g – ground temperature (K)

T_a – atmospheric temperature (K)

R_{th} – resistance to transfer of heat

The term, ρ indicates the density of the air over the surface that is responsible for convection and C_p refers to the specific heat capacity of air. The transfer resistance R_{th} depends upon wind speed, turbulence and surface characteristics.

Turbulence is generated whenever wind blows over the Earth's surface. The ground exerts a retarding force on the flow of air. This imparts frictional drag on the movement of air as it encounters rough surfaces, thereby slowing down the movement of air near the ground. Because of reduction in wind speed, a momentum is imparted or transferred from the atmosphere to the surface, creating turbulence that mixes the air and transports heat from the surface to the lower atmosphere. When height increases from the surface, eddies are larger so that transfer or transport of heat and momentum is more efficient and less turbulent (Bonan, 2002).

By parameterizing transfer resistance components into the equation, sensible heat flux can be calculated using Eqn.5 (Martinez et al., 2014; Bose et al., 2015):

$$H = k^2 C_p u \, \rho_a \, f(R_b) \frac{(T_g - T_a)}{\ln^2\left(\frac{z_a}{z_0}\right)} \tag{5}$$

where,

H – sensible heat flux (W/m^2)
ρ_a – atmospheric density (kg/m^3)

$$\rho_a = \frac{P}{RT_a} \tag{6}$$

P – surface pressure (Pa)
R – gas constant of Martian air (=189 J kg^{-1} K^{-1})
C_p – specific heat of CO_2 at constant pressure (= 736 J kg^{-1} K^{-1})
T_g – ground temperature (K)
T_a – atmospheric temperature (K)
k – von Karman constant (= 0.4)
Z_a – height at which atmospheric temperature and wind speed 'u' are recorded (= 1.6m)
Z_0 – surface roughness (varies from 0.5cm to 1.5cm)
$f(R_b)$ – function of Bulk Richardson number 'R_b'

$$f(R_b) = \begin{cases} (1 - 40R_b)^{0.5}, & T_g > T_a \\ \max(0.007, \left(1 + 5R_b + 44R_b^2\right)^{-2}), & T_g < T_a \end{cases} \quad (7)$$

The functions of Bulk Richardson number were proposed by Savijarvi et al. (2008) for unstable conditions and Savijarvi and Maattanen (2010) for stable conditions respectively. The former condition ($T_g > T_a$) is possible during the day time when the surface is exposed to solar insolation. The dust activity in the atmosphere and blowing of winds speed up during the day time thereby causing the transfer of heat from the surface to the atmosphere in an unstable fashion. Conversely, absence of high turbulent wind activity in the night renders smooth heat transfer and so the latter condition ($T_g < T_a$) corresponds to stable, night-time conditions (Martinez, personal communication, 2016).

Bulk Richardson number approximates the Gradient Richardson number. It is in fact, a dimensionless ratio in meteorology related to consumption of turbulence by shear production (generation of turbulent kinetic energy caused by wind shear). It is used to show dynamic stability and formation of turbulence (Roland, 1988). It is incorporated in the calculation of sensible heat flux to account for turbulence of wind which resists smooth transfer of heat from surface to atmosphere.

According to Sutton et al. (1978),

$$R_b = \frac{g z_a (T_a - T_g)}{\bar{T} u^2} \quad (8)$$

where,

g – acceleration due to gravity on Mars (= 3.72 m/s^2)

$\bar{T}$ - mean of atmospheric and ground temperatures (K)

T_g – ground temperature (K)

T_a – atmospheric temperature (K)

u – horizontal wind speed (m/s)

z_a – height at which atmospheric temperature is measured = 1.6 m

From Martinez (personal communication, 2016),

$$R_b = \frac{gz_a(T_a - T_g)}{T_a u^2} \tag{9}$$

where,

g – acceleration due to gravity on Mars (= 3.72 m/s^2)
T_g – ground temperature (K)
T_a – atmospheric temperature (K)
u – horizontal wind speed (m/s)
Z_a – height at which atmospheric temperature is measured = 1.6 m

It was found that the difference between values of R_b estimated from the above two formulations is negligible. Thereby, owing to a stronger authenticity of source, the method suggested by Sutton et al. (1978) is adopted for this study.

The values of atmospheric temperature (T_a), ground temperature (T_g) and surface pressure (P) are obtained from measurements made by the Atmospheric Temperature Sensor (ATS) and Ground Temperature Sensor (GTS) in the Rover Environmental Monitoring Station (REMS) on-board Mars Science Laboratory Curiosity Rover. Since horizontal wind speed measurements are not available for the sols under study, the maximum and minimum values of wind-speed used for calibration of the wind sensor (10m/s and 4m/s respectively) are used to generate worst case scenarios (Martinez et al., 2014). The surface roughness length is assumed to vary from 0.5cm to 1.5cm.

4.1.4 Downwelling Shortwave Radiation

A black body is a surface that absorbs all of the Sun's radiation that is incident over it. All other bodies other than perfect black bodies, reflect some portion of the sunlight. So, the actual fraction of energy that goes into the surface is only the absorbed portion.

If S↓ is the incoming solar irradiance, a fraction AS↓ is reflected and therefore only (1-A) S↓ is absorbed by the surface and acts as incoming energy to the system. Here, the fraction of energy that gets reflected from the surface, A, is called the albedo of the surface (Bonan, 2002).

Here, we need to determine the maximum amount of irradiance at a given location, season and time of the day. A comprehensive radiative transfer model developed by Haberle et al., (1993), to study the solar irradiance that reaches the surface is used for this study. This model was also used by Vicente-Retortillo et al., (2015).

We define 'E' as the solar irradiance at the top of the atmosphere.

$$E = \mu S_0 \left(\frac{\bar{r}}{r}\right)^2 \tag{10}$$

where,

S_0 – solar irradiance at mean Mars-Sun distance (1.52 AU) (=590 W/m^2)
μ - cosine of the solar zenith angle 'z'
r – Sun-Mars distance on a particular day (AU)
$\bar{r}$ – mean Sun-Mars distance (= 1.52 AU)

The cosine of the solar zenith angle 'μ' can be found out by:

$$\mu = \cos z = \sin\theta\sin\delta + \cos\theta\cos\delta\cos h \tag{11}$$

where,

θ – latitude
δ – solar declination angle
h – hour angle

The solar declination angle (δ) depends upon the obliquity of the orbit of Mars (ε = 25.2°) and orbital position in terms of its solar longitude (L_s). It can be formulated as:

$$\sin\delta = \sin\varepsilon \sin L_s \tag{12}$$

The hour angle (h), on the other hand depends upon the time of the day and can be written as:

$$h = \left(\frac{2\pi t}{p}\right) \tag{13}$$

where,

h – hour angle
t – time of the day measured from local noon (s)
p – length of a Martian solar day (=88775 s)
Finally, the Sun-Mars distance ‘r’ can be found out from Eqn. 14.

$$\left(\frac{\bar{r}}{r}\right) = \left(\frac{1+e\cos\left(L_s - L_{sp}\right)}{1-e^2}\right) \tag{14}$$

where,
e – orbit eccentricity (= 0.0934)
L_{sp} – areocentric/solar longitude at perihelion (= 250°)
L_s – areocentric/solar longitude at a point

It is to be noted that the highly elliptical orbit of Mars results in a high difference of magnitude of solar insolation between perihelion and aphelion. It is found that the insolation at perihelion (L_s = 250°) is as high as 717W/m^2 as compared to 493W/m^2 at aphelion (L = 71°) (Haberle et al., 1993).

The total downwelling solar irradiance reaching the surface and serving as an input to the system then depends upon the albedo of the surface, the solar zenith angle and the atmospheric dust opacity, which dominates all scattering activity in the Martian atmosphere. Haberle et al. (1993) accounts for the amount of solar energy lost due to dust scattering and surface albedo and calculates the net downwelling solar irradiance as follows:

$$S\downarrow = E\, f(\tau, \mu, A) \tag{15}$$

where,

S↓ - net downwelling solar irradiance (W/m^2)
E – solar irradiance at the top of atmosphere (W/m^2)
f (τ, μ, A) – normalized net irradiance function as a function of optical depth (τ) and zenith angle (z) for a particular albedo value(A).

The values of atmospheric dust opacity for the four sols under study were obtained by running the model Mars Climate Database v5.2 prepared by Laboratoire de Météorologie Dynamique du CNRS (Paris, France) in collaboration with the Open University (UK), the Oxford University (UK) and the Instituto de Astrofisica de Andalucia (Spain) with support from the European Space Agency (ESA) and the Centre National d'Etudes Spatiales (CNES) (Forget et al., 1999; Madeleine et al., 2011; Millour et al., 2015).

The MCD is a database of meteorological fields derived from General Circulation Model (GCM) numerical simulations of the Martian atmosphere and validated using available observational data (Millour et al., 2015).

The albedo is varied from 0.20 to 0.25 in the model which is a satisfactory approximation of the range of albedo values for dry land (Martinez et al., 2014). The normalized net irradiance function is provided for albedo 0.1 and 0.4 in tables provided by Haberle et al. (1993). A linear interpolation can extend the results to surfaces of arbitrary albedo.

4.2 Calculation of thermal inertia from Curiosity measurements

4.2.1 Estimation of Ground Heat Flux using SEB Equation

Once the four prime components of the surface energy budget are computed, the SEB equation is then used to determine the magnitude of heat flux stored in the ground. Eqn.1 can thus be modified as:

$$G = (1 - A)S\downarrow + L\downarrow - L\uparrow - H \tag{16}$$

where,

A – albedo of the surface

$S\downarrow$ – downwelling short-wave radiation (solar radiation)

$L\downarrow$ – downwelling longwave radiation (emission from atmosphere)

$L\uparrow$ - upwelling longwave radiation (emission from surface)

H – sensible heat flux

G – heat exchange by conduction into ground

4.2.2 Estimation of Ground Heat Flux using Curiosity Observations

The thermal inertia is calculated by solving the heat conduction equation applied to the soil. The heat conduction into the ground is described as:

$$\rho C_p \frac{\partial T}{\partial t} = \frac{\partial}{\partial z}\left(\lambda \frac{\partial T}{\partial z}\right) \tag{17}$$

Now, we also know that thermal inertia I can be described by Eqn. 18.

$$I = \sqrt{\lambda \rho C_p} \tag{18}$$

where,

I – thermal inertia (J m^{-2} K^{-1} $s^{-1/2}$)

ρ – soil density (kg m^{-3})

C_p – soil specific heat (J kg^{-1} K^{-1})

λ – thermal conductivity (W m^{-1} K^{-1})

Assuming thermal conductivity to be constant with depth ‘z’, Eqn. 17 can be rewritten as:

$$\rho C_p \frac{\partial T}{\partial t} = \lambda \left(\frac{\partial^2 T}{\partial z^2}\right) \tag{19}$$

Substituting Eqn. 18 in Eqn. 19, we get,

$$\frac{\partial T}{\partial t} = \left(\frac{I}{\rho C_p}\right)^2 \left(\frac{\partial^2 T}{\partial z^2}\right) \tag{20}$$

The boundary conditions used to solve the above conduction equation are as follows:

1. At the surface, z = 0 ⇒ T (0, t) = T_g (t) (21)

2. At a surface z = z_d, a depth at which subsurface temperature is fairly constant,

$$T\,(z_d, t) = T_d \tag{22}$$

Solving the above equation will provide the temperature profile of the sub-surface from which the net heat flux into the ground can be computed using the equation:

$$G^* = \left[-\lambda \frac{\partial T(z,t)}{\partial z}\right]_{z=0}^{z=z_d} \simeq \frac{I^2}{\rho C_p}\left[\frac{T(\delta,t) - T(0,t)}{\delta}\right] \tag{23}$$

where δ is the depth of topmost soil layer of the numerical model

For reasonable values of ρ, C_p, δ and T_d, we can reduce G^* to a function of I.

4.2.2.1 Volumetric heat capacity of Martian soil (ρC_p)

The planetary surface is covered by iron-rich sand and basaltic rocks. Several values of ρC_p have been suggested by various researchers. Mohlmann (2004) suggested a value of 1.255×10^6 J m^{-3} K^{-1}. Blake et al. (2013) suggested a density of around 3000 kg m^{-3} and a specific heat of 560 J kg^{-1} K^{-1} for soils experiencing temperatures around 200K giving an overall ρC_p value of around 1.7×10^6 J m^{-3} K^{-1}. For sandy soils and aeolian dunes on the Martian surface, Edgett and Christensen (1991) suggested ρC_p values from 0.8 to 1.3×10^6 J m^{-3} K^{-1} which was further established by Savijarvi (1999).

Hence, it can be thus concluded that values between 0.8 to 1.7×10^6 J m^{-3} K^{-1} are reasonable approximations for volumetric heat capacity, values increasing with the density of rock on the surface.

4.2.2.2 Depth at which subsurface temperature is considered to be invariant (z_d)

Z_d is considered to be 2 to 3 times larger than the diurnal e-folding or penetration depth (Martinez et al., 2014), given by:

$$L = \left(\frac{I}{\rho C_p}\right)\sqrt{\frac{2}{\omega}} \tag{24}$$

where,
L – penetration depth (m)
ω – angular speed of the planet's rotation (= 7.0774×10^{-5} s^{-1})

Taking I to be a few hundred units and ρC_p in the range previously estimated, the value of L is found to be a few centimetres. It can be concluded that z_d is roughly around 10 cm.

4.2.2.3 Values for T_d at $Z = Z_d$

The values of T_d are analysed from hourly GTS measurements and their standard deviation. T_d must be higher than the minimum ground daily temperature to ensure upward heat flux from deep soil. Subsequently, T_d must be slightly lower than daily average ground temperature as it is known to provide the most accurate solution to the heat conduction equation at diurnal scales (Savijarvi, 1995; Savijarvi and Maattanen, 2010).

4.2.3 Computation of Thermal Inertia

The G^* as obtained from the heat conduction equation is compared with G at different values of thermal inertia I. The value of thermal inertia at which the maximum values of G and G^* are equal, irrespective of the time of peaking is assigned as the TI value for that area.

Using the above procedure, Martinez at al. (2014) computed thermal inertia at Sols 82, 112 and 139 at an overall uncertainty of around 12%.

4.3 Computation of thermal inertia from THEMIS imagery

Processing of THEMIS images to obtain thermal inertia is done using the jENVI software developed by Dr. Jennifer Piatek, Central Connecticut State University. The jENVI plugin is installed in ENVI Classic 5.1. An additional menu "Mars" is added after the installation. THEMIS Processing occurs in three stages:

1. Pre-processing of the THEMIS data to get RDR
2. Generation of brightness temperature images from RDR data
3. Generation of thermal inertia layer from brightness temperature images.

Only night-time temperatures are used in the study because the effects of albedo and sun-heated slopes would have dissipated through the night and thermal contrast due to particle sizes are at a maximum. Band 9 temperatures are generally chosen to calculate thermal inertia as it possesses the highest signal-to-noise ratio and is relatively transparent to atmospheric dust (Fergason et al., 2006).

4.3.1 THEMIS Pre-processing

THEMIS pre-processing is done using the THMPROC web interface developed by Arizona State University. Pre-processing is done on the THEMIS image by applying the following functions:

Undrift/ Dewobble (UDDW)

The Undrift/ Dewobble filter is applied to the THEMIS IR-RDR QUBE to remove data fluctuations caused by changes in the IR detector array. Band 10 temperatures remain unchanged when this filter is applied.

Rectify

Rectify eliminates most of the black space present in a projected THEMIS IR image by shearing the image to produce a rectangle in both X and Y directions. This step produces a much smaller uncompressed image and is necessary for the Deplaid processing to occur.

Deplaid

The Deplaid filter is applied to remove row and line correlated radiance spikes from the ISIS projected THEMIS IR radiance data. Deplaid uses spectral information to remove line and row correlated noise that is not correlated between spectral bands. The effectiveness of the Deplaid filter is associated with the number of surface radiance bands available from the image.

Radiance correction (Radcorr)/ Automatic radiance correction (Auto – radcorr)

Radcorr and Auto-radcorr remove atmospheric emitted radiance from the THEMIS radiance images. Radcorr requires a user defined box within the image. Auto-radcorr automatically generates and removes atmospheric emitted radiance with no user input required. Radcorr algorithm should only be used on projected 10 band THEMIS IR images and will have no effect on other band combinations.

Unrectify

The Unrectify filter returns a rectified THEMIS IR image to its original projected state. This adds considerably to the file size.

The UDDW, Rectify, Deplaid and Unrectify filters are used in the present case. Simple Cylindrical projection is adopted. The pre-processed data is then downloaded.

4.3.2 Generation of brightness temperatures from THEMIS RDR data

Planck's law is used to calculate brightness temperatures from the RDR data. According to Planck's law, spectral radiant exitance (W m^{-2} μm^{-1}) is given by:

$$B_i(T_b) = \frac{2h_p c^2}{\lambda_i^5\left(e^{\frac{h_p c}{\lambda_i K_B T_b}}-1\right)} \tag{25}$$

Where,

B_i = spectral radiance (W m^{-2} μm^{-1})
h_p = Planck's constant = 6.626 x 10^{-34} J s
c = speed of light in vacuum = 3 x 10^8 m s^{-1}
K_B = Boltzmann constant = 1.38 x 10^{-23} J K^{-1}
T_b = Brightness temperature (K)
λ_i= wavelength (µm)

Using the Process THEMIS option, the pre-processed RDR file is opened. Turn on the "temperature" and "mask" file options. Select the option to save the local solar time to the image header. Band 9 brightness temperatures are then generated.

4.3.3 Generation of thermal inertia layer from THEMIS brightness temperature images

Thermal inertia calculation from THEMIS imagery is done by analysis of single point temperature measurements. Here, a 7D lookup table with values of parameters like albedo, thermal inertia, surface pressure, dust opacity, latitude, longitude and time of the day is used. The brightness temperatures generated as in Section 4.3.2 is compared with the brightness temperatures interpolated using the 7D lookup table and the corresponding thermal inertia in the lookup table is assigned as the TI value of that pixel.

The brightness temperature image and the appropriate band mask is selected. The appropriate locations for the output files are selected. The output files are a stack of the utb, elevation, and albedo images (masked by the input mask file); and a thermal inertia image. The “stack” image contains 3 or 4 bands, depending on inputs (temperature, elevation, albedo and local solar time, if included as a backplane).

An elevation image band (i.e. MOLA), and an albedo band (i.e. TES) are served as inputs. These images must be georeferenced for the stacking process to work correctly. Else ENVI cannot determine a common location for all the images. Hence, subsets of the elevation and albedo images that are confirmed to overlap the THEMIS image were used to avoid errors. The thermal inertia image is then generated along with the lookup tables used to interpolate the same (a series of files ending in ‘.tbl##’).

4.4 Particle size estimation from THEMIS thermal inertia

The THEMIS thermal inertia images generated can be used to derive particle sizes to enable surface characterization of the study area. Understanding the spatial distribution and variation of Mars’ surface materials is an important task as it can be used to plan site selection for future Mars missions. It can provide detailed information on:

- Engineering requirements for landing instrumentation so as to enable safe landing and take-off
- Selection of sites of scientific interest. (i.e. Places where outcrops are present are more likely to be chosen as landing sites as significant amount of geologic data can be obtained)

It also gives an idea of the geological and atmospheric processes that occurred in the recent past that have shaped the present surface condition.

Presley (2002) performed laboratory studies on variation of thermal conductivity with thermal inertia and derived an empirical relationship based on Presley and Christensen (1997) and Presley (1995).

$$\lambda = \left(\frac{I^2}{\rho C_p}\right) = \left(aP^{\frac{2}{3}}\right) d^{(0.52-KP)} \tag{26}$$

where,

λ – thermal conductivity (W m^{-1} K^{-1})
I – thermal inertia (J m^{-2} K^{-1} $s^{-1/2}$)
ρC_p – volumetric heat capacity (J m^{-3} K^{-1})

a, K - laboratory constants (=0.0014 and 0.01 respectively)

P – atmospheric pressure (torr)

d – particle size (µm)

Jones et al. (2014) derived particle sizes from thermal inertia images using the particle size classification scale developed by Wentworth (1922) using an average volumetric heat capacity of $1x10^{6}$ J m^{-3} K^{-1}. This scale however gives a broader soil classification without differentiating between fine and medium sand and also fine-grained soil. Hence, this study was modified by adopting the USGS grain size distribution scheme which gives a much better picture of soil classification.

Chapter 5

RESULTS AND DISCUSSIONS

5.1 Surface energy budget measurements

The various components of the surface energy budget i.e. upwelling longwave radiation, downwelling longwave radiation, downwelling shortwave radiation and sensible heat flux are computed as per Section 4.1 and their results are described below.

5.1.1 Upwelling Longwave Radiation

The hourly values of upwelling longwave radiation for the three sols representing spring season are shown in Table 5.1

Table 5.1 Upwelling longwave radiation for Spring

LMST (h)	Sol 108 (W/m^2)		Sol 110 (W/m^2)		Sol 112 (W/m^2)		Average (W/m^2)	
	Max	Min	Max	Min	Max	Min	Max	Min
0	109.830	80.656	107.807	77.990	110.854	82.660	109.497	80.435
1	108.007	76.637	103.299	73.459	104.315	74.600	105.207	74.899
2	100.572	71.819	104.914	74.449	100.124	70.805	101.870	72.358
3	99.415	71.332	98.295	68.453	99.559	70.591	99.089	70.125
4	97.084	68.366	96.753	67.487	95.101	65.348	96.313	67.067
5	94.859	64.774	93.552	65.704	93.496	63.161	93.969	64.547
6	104.526	75.895	116.943	82.703	102.585	73.677	108.018	77.425
7	134.397	102.653	132.845	102.948	176.193	123.793	147.812	109.798
8	200.465	166.309	200.764	165.273	200.333	165.270	200.521	165.617
9	264.885	223.756	299.203	238.145	262.265	221.058	275.451	227.653
10	318.043	273.989	316.507	272.587	340.230	280.488	324.927	275.688
11	360.828	312.192	366.125	318.087	373.360	317.508	366.771	315.929
12	385.946	336.812	387.254	337.583	381.558	332.878	384.919	335.758
13	388.808	338.190	386.274	336.628	389.419	338.166	388.167	337.661
14	355.118	294.856	370.740	322.305	375.077	327.597	366.978	314.919
15	316.660	273.269	310.652	243.882	329.791	286.142	319.034	267.765
16	262.623	223.075	260.684	223.071	253.789	192.175	259.032	212.774
17	199.644	157.764	214.077	177.752	210.313	175.616	208.011	170.378
18	180.625	147.362	173.950	138.749	180.820	145.706	178.465	143.939
19	161.073	129.201	165.411	132.572	164.213	127.996	163.566	129.923
20	142.989	111.592	144.862	113.470	143.864	112.803	143.905	112.622
21	139.052	108.959	135.304	104.368	134.934	103.751	136.430	105.693
22	122.140	92.174	124.759	93.241	126.410	94.760	124.436	93.392
23	113.950	84.879	114.182	83.945	113.162	82.904	113.764	83.909

The hourly values of upwelling longwave radiation for the three sols representing summer season are shown in Table 5.2

Table 5.2 Upwelling longwave radiation for Summer

LMST (h)	Sol 234 (W/m^2)		Sol 251 (W/m^2)		Sol 270 (W/m^2)		Average (W/m^2)	
	Max	Min	Max	Min	Max	Min	Max	Min
0	131.764	99.289	124.768	94.619	127.857	97.337	128.129	97.082
1	121.093	91.225	121.809	92.072	122.669	94.032	121.857	92.443
2	117.532	87.012	117.971	86.815	121.075	91.250	118.859	88.359
3	113.061	83.506	111.956	84.483	117.486	87.113	114.168	85.034
4	107.801	77.789	105.634	76.753	110.613	80.555	108.016	78.366
5	102.929	72.270	105.750	77.855	106.727	76.933	105.135	75.686
6	103.357	73.277	102.684	72.564	106.315	75.219	104.119	73.687
7	105.852	76.453	107.918	75.384	110.216	80.844	107.995	77.561
8	126.038	96.474	122.687	93.568	121.551	91.685	123.425	93.909
9	166.650	135.791	161.431	128.759	148.756	116.518	158.946	127.023
10	225.746	189.208	223.632	186.371	204.163	169.057	217.847	181.545
11	274.301	233.680	267.848	227.775	267.130	218.529	269.760	226.661
12	323.380	273.467	304.009	259.815	277.611	236.422	301.667	256.568
13	325.844	280.480	321.942	276.488	303.031	259.484	316.939	272.151
14	328.460	283.379	330.293	284.802	310.314	266.671	323.022	278.284
15	322.552	277.198	321.234	276.606	304.887	261.844	316.225	271.883
16	292.803	249.567	294.186	251.657	270.370	220.858	285.787	240.694
17	243.171	191.844	252.649	214.825	233.907	188.240	243.242	198.303
18	215.341	180.599	218.761	181.796	202.492	160.745	212.198	174.380
19	185.444	150.656	187.869	152.495	182.524	149.473	185.279	150.875
20	163.981	132.469	165.739	132.175	163.540	131.364	164.420	132.003
21	144.409	112.412	153.609	121.822	144.470	112.387	147.496	115.540
22	137.422	106.788	139.424	106.650	139.032	108.591	138.626	107.343
23	129.387	98.989	132.281	101.842	127.161	97.678	129.610	99.503

The hourly values of upwelling longwave radiation for the three sols representing autumn season are shown in Table 5.3

Table 5.3 Upwelling longwave radiation for Autumn

LMST (h)	Sol 440 (W/m^2)		Sol 441 (W/m^2)		Sol 443 (W/m^2)		Average (W/m^2)	
	Max	**Min**	**Max**	**Min**	**Max**	**Min**	**Max**	**Min**
0	106.093	77.953	105.090	76.268	103.306	73.692	104.830	75.971
1	103.758	74.306	102.627	74.642	101.708	73.035	102.697	73.994
2	98.495	70.971	97.791	67.829	99.267	71.249	98.518	70.016
3	95.643	66.209	96.420	67.191	98.616	68.798	96.893	67.400
4	92.773	63.138	95.740	66.336	93.674	63.758	94.062	64.411
5	93.868	64.637	92.513	62.772	92.155	63.250	92.845	63.553
6	92.576	63.941	93.013	63.920	94.302	64.812	93.297	64.224
7	102.696	73.822	103.289	74.151	102.628	74.359	102.871	74.111
8	122.844	90.663	150.292	109.624	131.014	100.255	134.717	100.181
9	169.868	127.776	165.354	134.366	161.054	128.647	165.426	130.263
10	181.384	147.761	194.216	159.233	194.143	160.528	189.914	155.841
11	204.133	168.795	230.847	193.498	232.257	194.113	222.412	185.469
12	226.235	187.752	251.946	212.172	249.678	210.111	242.620	203.345
13	237.946	195.414	254.827	215.612	251.633	211.715	248.135	207.580
14	247.687	208.929	243.966	203.463	248.563	211.557	246.739	207.983
15	227.195	184.264	234.232	196.569	237.822	199.176	233.083	193.336
16	212.303	176.238	214.419	177.860	203.814	162.653	210.179	172.250
17	185.537	151.542	184.676	151.138	185.001	151.654	185.072	151.445
18	152.353	119.189	151.928	120.258	146.103	112.541	150.128	117.329
19	128.381	98.424	129.174	100.526	136.266	105.148	131.274	101.366
20	123.499	91.502	118.509	88.571	122.309	92.836	121.439	90.970
21	113.734	83.509	114.740	85.675	116.513	86.363	114.996	85.182
22	111.390	81.080	110.613	82.055	110.681	81.617	110.895	81.584
23	106.602	77.436	106.481	79.754	108.615	78.731	107.233	78.640

The hourly values of upwelling longwave radiation for the three sols representing winter season are shown in Table 5.4

Table 5.4 Upwelling longwave radiation for Winter

LMST (h)	Sol 610 (W/m^2)		Sol 620 (W/m^2)		Sol 631 (W/m^2)		Average (W/m^2)	
	Max	**Min**	**Max**	**Min**	**Max**	**Min**	**Max**	**Min**
0	82.272	51.685	84.163	53.134	91.768	61.002	86.068	55.274
1	77.954	46.541	79.282	51.887	90.584	59.902	82.607	52.777
2	74.682	43.488	77.963	48.153	88.634	58.703	80.426	50.115
3	76.269	43.090	75.938	43.089	88.157	56.583	80.121	47.587
4	76.110	42.655	71.621	39.041	82.345	52.418	76.692	44.705
5	73.934	41.429	76.230	45.545	80.387	49.865	76.850	45.613
6	78.749	47.966	81.287	52.121	81.939	52.071	80.658	50.719
7	130.434	88.743	109.876	79.686	106.471	75.718	115.594	81.382
8	155.436	122.500	171.872	136.269	139.339	108.540	155.549	122.436
9	208.929	174.047	237.631	191.113	185.718	150.532	210.759	171.897
10	244.447	205.570	252.269	212.604	261.799	214.292	252.838	210.822
11	272.877	230.096	276.873	234.975	281.880	236.455	277.210	233.842
12	276.011	234.817	284.004	242.452	291.329	248.293	283.781	241.854
13	272.326	227.736	284.521	242.856	285.742	243.919	280.863	238.170
14	259.696	219.679	257.617	210.715	274.680	233.310	263.998	221.235
15	235.691	197.727	223.611	176.878	250.380	211.718	236.561	195.441
16	195.204	161.207	184.902	139.386	202.545	157.155	194.217	152.583
17	157.360	125.009	158.965	126.469	175.886	142.035	164.070	131.171
18	115.764	87.553	114.210	84.545	136.360	105.583	122.111	92.560
19	101.637	71.550	105.646	75.038	115.716	86.761	107.666	77.783
20	98.202	66.941	100.655	69.968	109.715	80.003	102.857	72.304
21	94.140	65.463	89.668	58.667	103.267	73.862	95.692	65.997
22	89.372	60.641	87.477	57.567	96.063	65.833	90.971	61.347
23	84.409	52.975	85.343	57.029	93.801	64.593	87.851	58.199

The diurnal and seasonal variation of maximum and minimum upwelling longwave radiation is shown in Fig 5.1 and Fig 5.2 respectively.

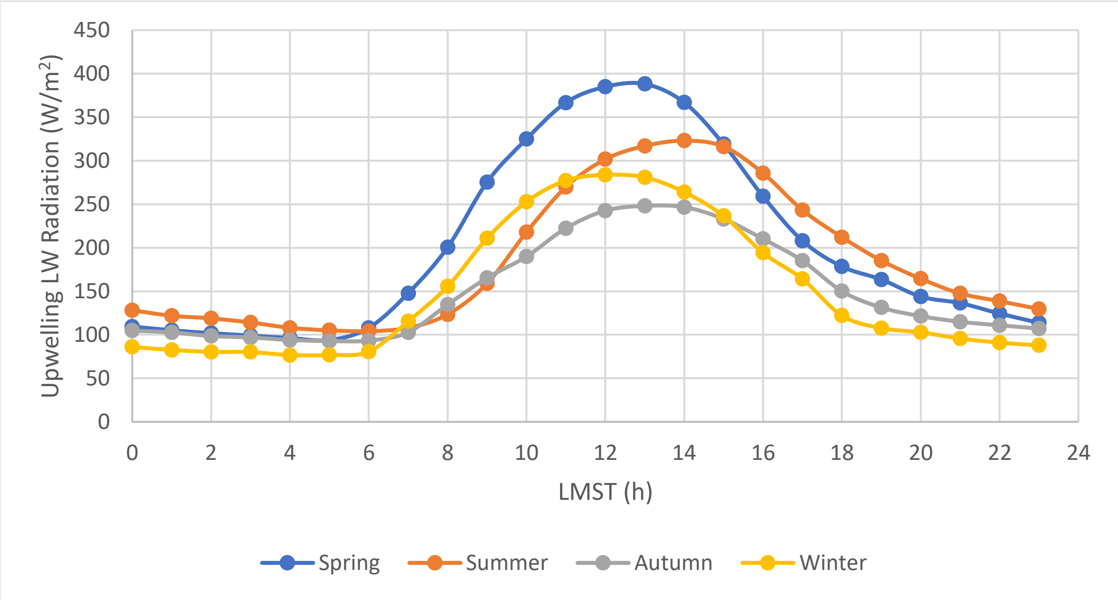

Fig 5.1 Diurnal variation of maximum upwelling longwave radiation

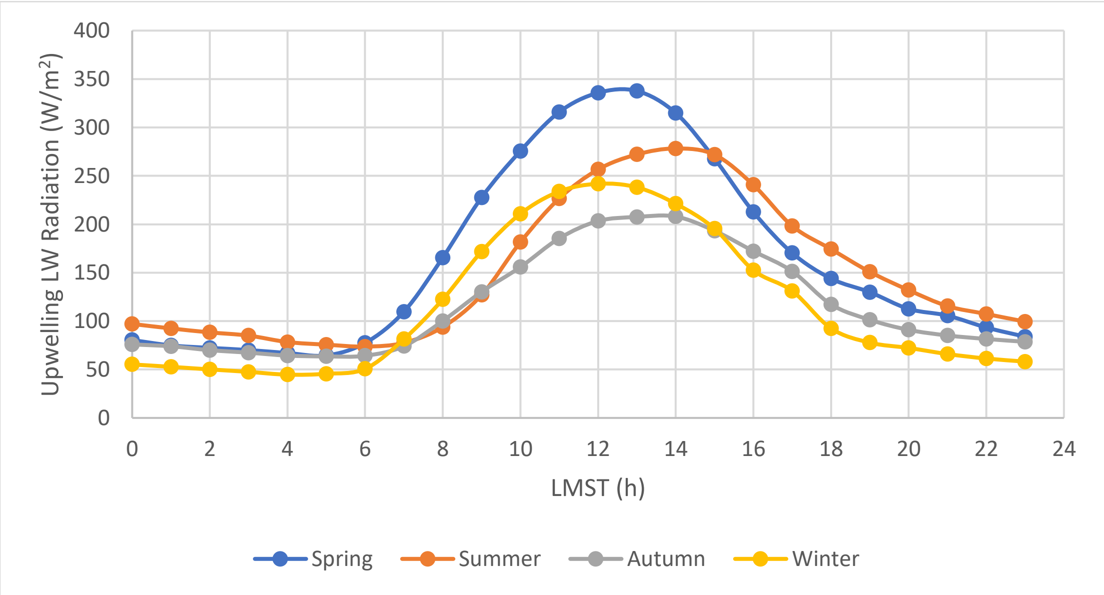

Fig 5.2 Diurnal variation of minimum upwelling longwave radiation

Upwelling longwave radiation is directly dependent on the ground temperature. The plot of GTS measurements of surface temperature for each of the twelve sols is shown in Fig 5.3.

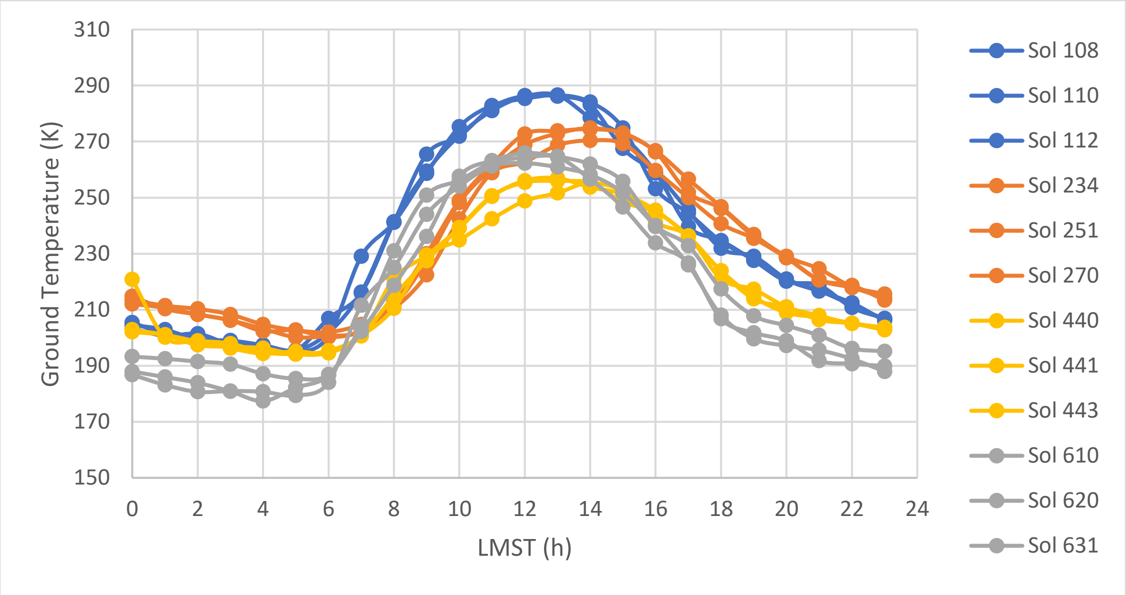

Fig 5.3 Diurnal variation of surface temperature from GTS measurements

It is seen that spring (Sol 108, Sol 110, Sol 112) experiences the highest surface temperature followed by summer (Sol 234, Sol 251, Sol 270), winter (Sol 610, Sol 620, Sol 631) and the minimum surface temperature occurs in autumn (Sol 440, Sol 441, Sol 443).

Seasonal variations are dependent on temperature of the surface during the day, which is closely dependent on the Mars-Sun distance. Mars is found to be closest during the spring season and farthest in the autumn season when compared to summer and winter respectively (Table 3.4). This is accounted for by the highly elliptical orbit of Mars that force the perihelion and aphelion to lie in spring and autumn respectively.

Quite evidently, spring and autumn are found to have the highest and lowest upwelling longwave radiation respectively (Fig 5.1 and Fig 5.2).

5.1.2 Sensible Heat Flux

The hourly values of sensible heat flux for the three sols representing spring season are shown in Table 5.5

Table 5.5 Sensible heat flux for Spring

LMST (h)	Sol 108 (W/m^2)		Sol 110 (W/m^2)		Sol 112 (W/m^2)		Average (W/m^2)	
	Max	Min	Max	Min	Max	Min	Max	Min
0	-18.167	-1.188	-20.865	-0.434	-19.646	-1.123	-19.559	-0.915
1	-20.961	-1.179	-18.502	-0.711	-19.852	-1.148	-19.772	-1.013
2	-19.346	-1.201	-17.746	-0.479	-21.165	-1.511	-19.419	-1.064
3	-21.275	-1.595	-20.866	-0.822	-19.268	-0.879	-20.470	-1.099
4	-20.566	-1.266	-20.557	-1.177	-22.907	-0.876	-21.343	-1.106
5	-23.725	-1.603	-24.851	-1.967	-23.731	-1.431	-24.102	-1.667
6	-19.715	-1.393	-18.629	0.393	-17.978	-0.768	-18.774	-0.589
7	-9.413	0.216	-7.064	0.613	-11.778	1.041	-9.418	0.623
8	23.887	5.938	23.934	5.717	17.795	1.084	21.872	4.246
9	34.280	7.821	44.508	10.225	25.047	8.894	34.612	8.980
10	45.013	15.635	44.186	15.063	44.874	13.400	44.691	14.699
11	42.832	14.736	43.790	15.140	43.265	12.966	43.296	14.281
12	35.986	10.182	36.071	10.084	38.960	14.088	37.006	11.451
13	32.419	10.774	31.728	10.424	32.241	9.729	32.129	10.309
14	17.963	2.994	21.076	5.170	24.924	7.849	21.321	5.338
15	14.678	2.812	13.237	0.507	14.539	3.980	14.151	2.433
16	5.245	0.305	4.816	0.303	12.602	0.719	7.554	0.442
17	-10.614	-0.615	-4.311	0.038	4.438	-0.099	-3.496	-0.225
18	4.822	-0.236	-7.971	-0.269	-6.830	-0.026	-3.326	-0.177
19	-9.197	-0.388	-7.777	-0.017	-10.096	-0.197	-9.023	-0.201
20	-16.407	-1.525	-15.523	-1.377	-9.142	-0.177	-13.691	-1.026
21	-12.113	-0.275	-14.488	-0.636	-15.324	-0.863	-13.975	-0.591
22	-16.798	-1.012	-16.177	-0.742	-17.738	-0.646	-16.904	-0.800
23	-19.415	-1.332	-19.988	-1.290	-21.113	-1.151	-20.172	-1.258

The hourly values of sensible heat flux for the three sols representing summer season are shown in Table 5.6

Table 5.6 Sensible heat flux for Summer

LMST (h)	Sol 234 (W/m^2)		Sol 251 (W/m^2)		Sol 270 (W/m^2)		Average (W/m^2)	
	Max	Min	Max	Min	Max	Min	Max	Min
0	-16.950	-1.207	-11.803	-0.204	-12.844	-0.489	-13.866	-0.633
1	-11.414	-0.061	-14.775	-0.668	-15.393	-0.882	-13.861	-0.537
2	-11.199	0.278	-15.898	-0.214	-16.847	-0.663	-14.648	-0.200
3	-13.284	-0.192	-10.299	0.086	-15.184	-0.593	-12.922	-0.233
4	-15.404	0.273	-12.774	0.134	-12.775	0.154	-13.651	0.187
5	-15.413	0.079	-11.806	0.195	-13.736	0.055	-13.652	0.110
6	-15.867	-0.173	-14.014	0.350	-13.062	0.551	-14.314	0.243
7	-12.707	0.363	-15.870	0.020	-8.412	1.291	-12.330	0.558
8	-8.533	0.432	6.543	-1.154	-9.159	0.577	-3.716	-0.048
9	11.089	0.437	8.287	0.064	14.612	1.386	11.329	0.629
10	25.235	5.997	25.299	4.628	17.956	2.824	22.830	4.483
11	42.129	11.235	29.235	7.578	34.896	7.149	35.420	8.654
12	36.886	13.961	37.268	11.070	33.930	11.033	36.028	12.021
13	30.313	4.937	26.835	6.701	26.176	6.571	27.775	6.070
14	17.878	1.886	17.062	3.609	20.091	2.640	18.344	2.712
15	17.364	3.357	9.613	0.298	12.078	1.325	13.018	1.660
16	8.883	0.332	10.859	-0.220	6.538	0.280	8.760	0.131
17	-13.218	-0.923	4.983	-0.239	6.564	0.063	-0.557	-0.366
18	-2.568	0.424	-4.761	-0.033	9.169	0.554	0.613	0.315
19	-7.037	-0.229	-9.342	-0.308	6.052	0.153	-3.442	-0.128
20	-9.414	-0.193	-8.030	-0.011	-5.423	0.290	-7.622	0.029
21	-10.560	0.044	-9.587	-0.032	-8.260	0.064	-9.469	0.025
22	-13.113	-0.771	-15.099	-0.550	-15.099	-1.134	-14.437	-0.818
23	-16.846	-0.602	-14.458	-0.423	-13.019	-0.213	-14.774	-0.413

The hourly values of sensible heat flux for the three sols representing autumn season are shown in Table 5.7.

Table 5.7 Sensible heat flux for Autumn

LMST (h)	Sol 440 (W/m^2)		Sol 441 (W/m^2)		Sol 443 (W/m^2)		Average (W/m^2)	
	Max	**Min**	**Max**	**Min**	**Max**	**Min**	**Max**	**Min**
0	-10.078	0.269	10.341	-1.021	13.491	-0.574	4.585	-0.442
1	-12.193	1.755	-13.015	0.185	24.469	-1.146	-0.246	0.265
2	-8.451	1.909	18.060	0.076	8.549	-2.081	6.053	-0.032
3	17.681	-0.011	12.785	-1.196	9.204	-1.962	13.223	-1.056
4	16.954	-0.669	-11.010	1.565	-12.716	1.355	-2.257	0.750
5	11.766	-1.677	-11.706	1.731	-12.212	1.327	-4.051	0.460
6	-11.600	1.433	13.001	-2.098	13.695	-1.090	5.032	-0.585
7	9.220	-1.521	-9.059	1.527	-15.560	0.404	-5.133	0.137
8	12.545	-0.338	31.601	2.860	17.957	1.009	20.701	1.177
9	33.999	4.656	36.689	10.117	33.499	7.888	34.729	7.554
10	32.207	8.269	37.616	10.471	34.204	9.715	34.676	9.485
11	25.241	5.355	37.905	10.039	38.911	10.993	34.019	8.796
12	26.332	4.853	30.703	7.070	32.418	8.183	29.818	6.702
13	19.622	1.833	27.517	7.453	29.963	7.897	25.701	5.728
14	15.836	3.299	16.911	2.278	20.830	4.970	17.859	3.516
15	11.139	0.291	15.175	2.877	13.900	1.206	13.405	1.458
16	11.641	0.566	12.464	0.188	8.678	0.320	10.928	0.358
17	6.875	0.230	7.817	0.302	6.334	-0.104	7.009	0.143
18	9.425	0.001	8.397	-0.052	10.713	0.227	9.512	0.059
19	-7.334	0.650	-4.823	1.095	7.229	-0.691	-1.643	0.351
20	6.541	-1.507	7.423	1.500	-12.583	0.322	0.460	0.105
21	-8.240	1.209	-6.616	1.364	7.070	-1.415	-2.595	0.386
22	-9.531	0.988	-9.915	0.553	8.009	-1.285	-3.812	0.085
23	-8.037	1.510	-11.782	-0.063	-7.798	1.604	-9.206	1.017

The hourly values of sensible heat flux for the three sols representing winter season are shown in Table 5.8

Table 5.8 Sensible heat flux for Winter

LMST (h)	Sol 610 (W/m^2)		Sol 620 (W/m^2)		Sol 631 (W/m^2)		Average (W/m^2)	
	Max	Min	Max	Min	Max	Min	Max	Min
0	-21.900	-0.516	-20.796	-0.336	-14.477	0.363	-19.058	-0.163
1	-24.460	-0.350	-19.309	-0.346	-15.737	0.095	-19.835	-0.200
2	-25.308	-0.376	-23.545	-0.408	-15.231	0.232	-21.361	-0.184
3	-25.636	-0.288	-28.995	-0.600	-13.484	1.147	-22.705	0.086
4	-24.659	-0.051	-29.392	-0.817	-18.174	-0.026	-24.075	-0.298
5	-24.167	0.077	-26.306	-0.439	-20.409	-0.264	-23.627	-0.209
6	-21.403	-0.098	-18.325	-0.113	-16.825	0.505	-18.851	0.098
7	13.209	-0.816	-15.143	-0.516	-10.041	0.736	-3.992	-0.199
8	20.252	3.182	25.356	5.392	18.442	2.811	21.350	3.795
9	31.357	8.689	34.186	6.405	22.385	4.701	29.309	6.598
10	30.979	9.047	30.879	8.689	32.478	7.233	31.445	8.323
11	33.747	7.729	30.702	8.099	33.476	8.976	32.642	8.268
12	25.370	6.582	25.974	6.441	33.515	10.915	28.286	7.979
13	27.068	5.557	27.217	8.145	12.026	2.308	22.104	5.337
14	21.399	4.652	16.723	2.186	10.321	1.892	16.148	2.910
15	5.388	0.060	-5.848	0.232	5.655	0.589	1.732	0.294
16	-5.109	-0.153	-13.281	-0.800	7.995	0.086	-3.465	-0.289
17	-9.811	-0.833	-6.354	-0.018	6.188	0.124	-3.326	-0.242
18	-15.679	-0.977	-14.883	-1.077	-7.903	-0.072	-12.822	-0.709
19	-18.632	-0.383	-15.357	-0.658	-9.911	-0.137	-14.633	-0.393
20	-17.331	-0.622	-17.179	-0.436	-10.180	0.158	-14.897	-0.300
21	-18.210	-0.838	-21.848	-0.222	-14.359	-0.116	-18.139	-0.392
22	-18.125	-0.620	-25.178	-0.880	-16.821	0.189	-20.041	-0.437
23	-22.440	-0.783	-19.895	-0.915	-15.700	0.006	-19.345	-0.564

The diurnal and seasonal variation of maximum and minimum sensible heat flux is shown in Fig 5.4 and Fig 5.5 respectively.

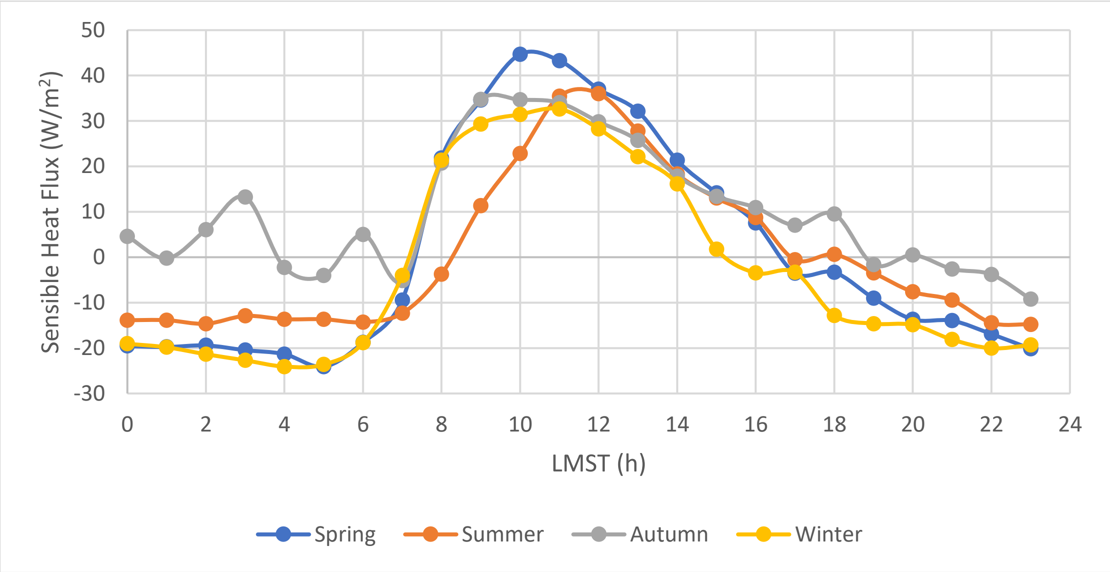

Fig 5.4 Diurnal variation of maximum sensible heat flux

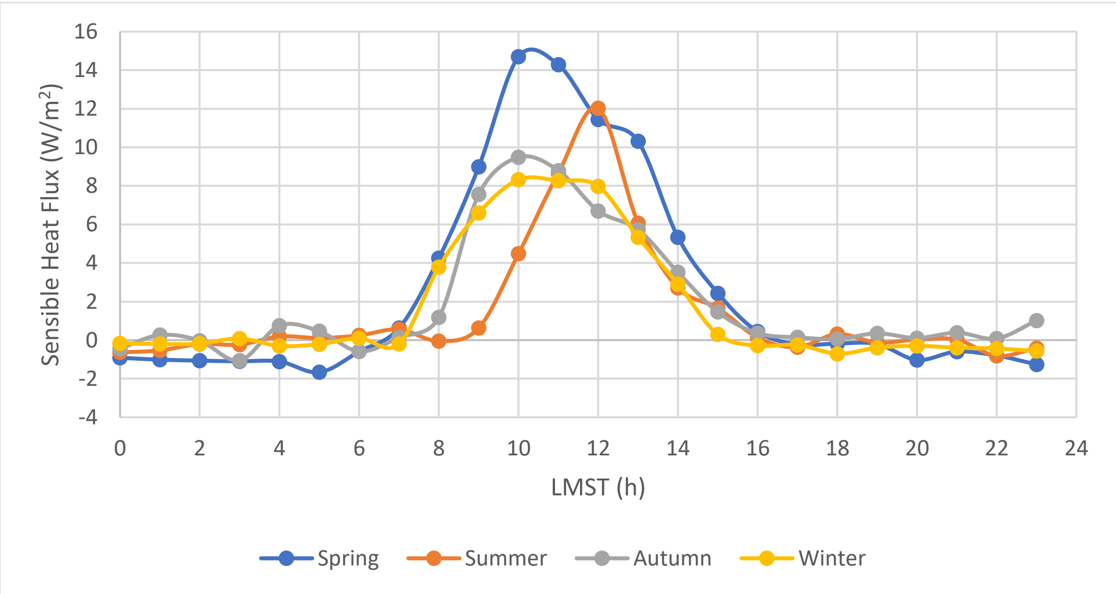

Fig 5.5 Diurnal variation of minimum sensible heat flux

The sensible heat flux depends upon atmospheric temperature at 1.6m (T_a), surface temperature (T_g), wind speed (u) and surface pressure (P). Since a predefined worst case scenario is used for the wind speed term (varying from 4 to 10 m/s), effect of sudden variations is negated. The nature of variation between seasons is roughly similar, except for autumn (Fig 5.4). This variation is probably due to greater turbulence caused due to erratic atmospheric heating and cooling or due to incompetent measurements from the ATS sensor. The high values of function of Bulk Richardson number at these local times substantiate the assumption.

Greater sensible heat flux is found to occur in spring and autumn seasons when compared to summer and winter (Fig 5.4 and Fig 5.5). It can be assumed that turbulence in wind is minimum as the days are closer to the equinox when compared to the solstice (extreme conditions – due to longer day or night).

5.1.3 Downwelling Shortwave Radiation

The hourly values of downwelling shortwave radiation for the three sols representing spring season are shown in Table 5.9.

Table 5.9 Downwelling Shortwave Radiation for Spring

LMST (h)	Sol 108 (W/m^2)		Sol 110 (W/m^2)		Sol 112 (W/m^2)		Average (W/m^2)	
	Max	Min	Max	Min	Max	Min	Max	Min
0	0	0	0	0	0	0	0	0
1	0	0	0	0	0	0	0	0
2	0	0	0	0	0	0	0	0
3	0	0	0	0	0	0	0	0
4	0	0	0	0	0	0	0	0
5	0	0	0	0	0	0	0	0
5.93	0	0	0	0	0	0	0	0
6	2.741	2.599	2.907	2.757	3.035	2.863	2.894	2.740
7	66.269	62.732	66.764	63.034	65.392	61.843	66.142	62.536
8	174.039	164.292	174.36	164.596	171.887	162.454	173.429	163.781
9	281.89	266.284	281.703	266.107	278.806	263.669	280.800	265.353
10	370.493	350.306	368.368	348.167	367.858	347.62	368.906	348.698
11	428.9	405.109	424.613	401.464	426.059	402.868	426.524	403.147
12	450.558	425.945	444.775	420.826	447.884	423.229	447.739	423.333
13	432.865	408.413	424.613	401.464	430.035	406.181	429.171	405.353
14	377.618	356.837	368.368	348.167	375.001	354.167	373.662	353.057
15	291.814	275.738	281.703	266.107	289.059	272.946	287.525	271.597
16	182.74	172.646	174.36	164.596	180.621	170.839	179.240	169.360
17	71.108	67.199	66.764	63.034	70.063	66.14	69.312	65.458
18	2.882	2.717	2.907	2.757	3.167	2.995	2.985	2.823

18.07	0	0	0	0	0	0	0	0
19	0	0	0	0	0	0	0	0
20	0	0	0	0	0	0	0	0
21	0	0	0	0	0	0	0	0
22	0	0	0	0	0	0	0	0
23	0	0	0	0	0	0	0	0

The hourly values of downwelling shortwave radiation for the three sols representing summer season are shown in Table 5.10

Table 5.10 Downwelling Shortwave Radiation for Summer

LMST (h)	**Sol 234 (W/m^2)**		**Sol 251 (W/m^2)**		**Sol 270 (W/m^2)**		**Average (W/m^2)**	
	Max	**Min**	**Max**	**Min**	**Max**	**Min**	**Max**	**Min**
0	0	0	0	0	0	0	0	0
1	0	0	0	0	0	0	0	0
2	0	0	0	0	0	0	0	0
3	0	0	0	0	0	0	0	0
4	0	0	0	0	0	0	0	0
5	0	0	0	0	0	0	0	0
5.87	0	0	0	0	0	0	0	0
6	5.408	5.110	5.006	4.733	4.211	4.091	4.875	4.645
7	72.346	68.297	71.733	67.758	70.433	66.393	71.504	67.483
8	178.360	168.619	177.828	167.894	176.567	166.812	177.585	167.775
9	281.294	265.459	280.213	264.569	268.734	253.706	276.747	261.245
10	364.508	344.132	362.700	342.581	351.699	331.648	359.636	339.454
11	417.333	394.078	415.669	392.059	418.318	394.733	417.107	393.623
12	436.671	411.978	434.549	410.122	438.174	413.117	436.465	411.739
13	419.848	395.964	418.155	394.544	420.800	397.216	419.601	395.908
14	369.036	348.660	367.171	346.493	356.034	335.984	364.080	343.712
15	287.814	271.514	286.654	270.550	274.922	259.452	283.130	267.172
16	184.406	173.993	183.789	173.523	182.746	172.340	183.647	173.285
17	75.660	71.426	75.347	71.010	73.946	69.730	74.984	70.722
18	5.898	5.280	5.161	4.869	4.392	4.146	5.150	4.765
18.13	0	0	0	0	0	0	0	0
19	0	0	0	0	0	0	0	0
20	0	0	0	0	0	0	0	0
21	0	0	0	0	0	0	0	0
22	0	0	0	0	0	0	0	0
23	0	0	0	0	0	0	0	0

The hourly values of downwelling shortwave radiation for the three sols representing autumn season are shown in Table 5.11

Table 5.11 Downwelling Shortwave Radiation for Autumn

LMST (h)	Sol 440 (W/m^2)		Sol 441 (W/m^2)		Sol 443 (W/m^2)		Average (W/m^2)	
	Max	Min	Max	Min	Max	Min	Max	Min
0	0	0	0	0	0	0	0	0
1	0	0	0	0	0	0	0	0
2	0	0	0	0	0	0	0	0
3	0	0	0	0	0	0	0	0
4	0	0	0	0	0	0	0	0
5	0	0	0	0	0	0	0	0
6	0	0	0	0	0	0	0	0
6.09	0	0	0	0	0	0	0	0
7	55.294	52.062	55.118	51.903	55.113	51.905	55.175	51.957
8	145.886	137.483	145.675	137.065	145.275	136.703	145.612	137.084
9	229.212	215.827	229.000	215.647	228.492	215.188	228.901	215.554
10	293.694	276.394	293.079	276.226	292.496	275.290	293.090	275.970
11	334.032	314.681	333.835	314.063	332.748	313.498	333.538	314.081
12	349.063	328.530	347.915	327.421	346.899	326.493	347.959	327.481
13	334.953	315.602	334.295	314.982	333.664	313.498	334.304	314.694
14	295.342	278.041	294.723	277.459	294.135	276.929	294.733	277.476
15	231.554	217.835	231.003	217.310	230.487	216.851	231.015	217.332
16	148.220	139.583	147.770	139.159	147.361	138.788	147.784	139.177
17	56.910	53.562	56.726	53.395	56.718	53.395	56.785	53.451
17.91	0	0	0	0	0	0	0	0
18	0	0	0	0	0	0	0	0
19	0	0	0	0	0	0	0	0
20	0	0	0	0	0	0	0	0
21	0	0	0	0	0	0	0	0
22	0	0	0	0	0	0	0	0
23	0	0	0	0	0	0	0	0

The hourly values of downwelling shortwave radiation for the three sols representing winter season are shown in Table 5.12

Table 5.12 Downwelling Shortwave Radiation for Winter

LMST (h)	Sol 610 (W/m^2)		Sol 620 (W/m^2)		Sol 631 (W/m^2)		Average (W/m^2)	
	Max	**Min**	**Max**	**Min**	**Max**	**Min**	**Max**	**Min**
0	0	0	0	0	0	0	0	0
1	0	0	0	0	0	0	0	0
2	0	0	0	0	0	0	0	0
3	0	0	0	0	0	0	0	0
4	0	0	0	0	0	0	0	0
5	0	0	0	0	0	0	0	0
6	0	0	0	0	0	0	0	0
6.13	0	0	0	0	0	0	0	0
7	53.045	49.925	54.033	50.848	57.947	54.538	55.008	51.770
8	155.016	145.926	144.505	135.858	148.958	140.058	149.493	140.614
9	223.335	210.121	227.958	214.471	234.330	220.486	228.541	215.026
10	300.260	282.841	292.747	275.694	300.637	282.707	297.881	280.414
11	326.900	307.697	333.159	313.588	341.710	321.636	333.923	314.307
12	340.603	320.241	347.026	326.280	356.684	335.873	348.104	327.465
13	327.346	308.143	333.614	314.043	342.176	322.103	334.379	314.763
14	301.919	284.085	293.965	276.912	301.888	283.958	299.257	281.652
15	225.268	212.055	229.931	216.445	236.018	222.175	230.406	216.892
16	156.930	147.600	146.553	137.906	150.832	141.932	151.438	142.479
17	54.336	51.109	55.351	52.166	57.379	53.970	55.689	52.415
17.87	0	0	0	0	0	0	0	0
18	0	0	0	0	0	0	0	0
19	0	0	0	0	0	0	0	0
20	0	0	0	0	0	0	0	0
21	0	0	0	0	0	0	0	0
22	0	0	0	0	0	0	0	0
23	0	0	0	0	0	0	0	0

The diurnal and seasonal variation of maximum and minimum downwelling shortwave radiation is shown in Fig 5.6 and Fig 5.7 respectively.

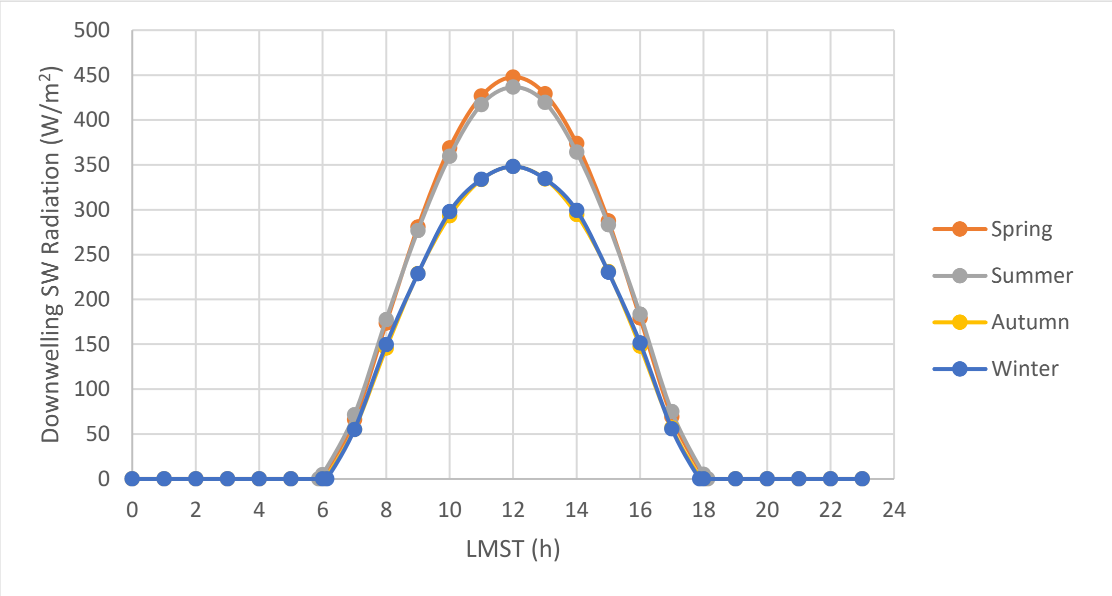

Fig 5.6 Diurnal variation of maximum downwelling shortwave radiation

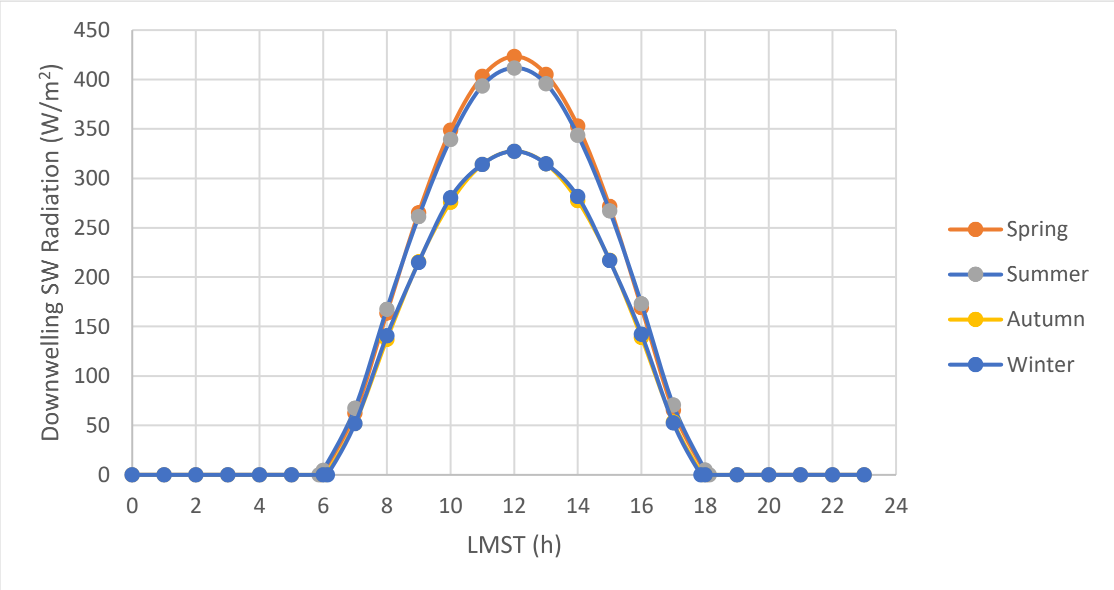

Fig 5.7 Diurnal variation of minimum downwelling shortwave radiation

Solar insolation at the top of the atmosphere is dependent mainly upon the distance between Mars and the Sun and the solar declination angle. Spring, therefore receives greatest solar insolation when compared to summer. Though the distance between Mars and Sun is lesser in winter when compared to autumn, its higher solar declination angle and thereby greater zenith angle causes reduction in its incoming solar energy. Hence, autumn tends to receive slightly larger amount of solar energy at the top of the atmosphere than winter.

The amount of shortwave energy reaching the surface is also dependent upon how much of this incoming radiation is scattered by dust and aerosol particles (Haberle et al., 1993; Savijarvi et al., 2005). Hence, atmospheric dust opacity plays an important role in the same. Spring and summer are dust seasons of the Martian year cycle (Table 1.2). Hence, a greater amount of energy is lost due to absorption by dust in these seasons when compared to winter and autumn. Table 5.13 gives an idea of the solar insolation at the top of the atmosphere and the effect of dust absorption at 1200 hrs LMST on the chosen sols for study.

Table 5.13 Effect of atmospheric dust on solar insolation at 1200 hrs LMST

Sol	Season	Solar irradiance at TOA (W/m^2)	Atmospheric dust Opacity τ_{vis}	Percent absorption by dust (%)
108	Spring	683.700	0.9458	34.10
110		684.270	0.9678	34.40
112		684.838	0.9824	34.60
234	Summer	649.809	0.8027	32.80
251		642.825	0.7825	32.40
270		642.485	0.7663	31.80
440	Autumn	477.515	0.4299	26.90
441		476.596	0.4274	27.00
443		474.555	0.4232	26.90
610	Winter	462.777	0.3623	26.40
620		471.504	0.3671	26.40
631		483.968	0.3715	26.30

Solar irradiance will be zero beyond sunset and before sunrise owing to absence of the Sun. The time at which sun rises and sets for the twelve sols can be found out by determining the hour angle for which solar irradiance at TOA will be zero. Table 5.14 shows the sunrise and sunset times calculated in local times in hours. It is seen that summers have the longest and winters have the shortest diurnal insolation period in a Martian year.

Table 5.14 Sunrise and sunset times calculated for the sols under study

Sol	Season	Sunrise (local time in hrs)	Sunset (local time in hrs)
108	Spring	05:57	18:04
110		05:57	18:04
112		05:57	18:04
234	Summer	05:54	18:08
251		05:55	18:07
270		05:56	18:06
440	Autumn	06:06	17:56
441		06:06	17:56
443		06:06	17:56
610	Winter	06:08	17:54
620		06:08	17:54
631		06:07	17:55

5.1.4 Downwelling Longwave Radiation

The hourly values of downwelling longwave radiation for the three sols representing spring season are shown in Table 5.15

Table 5.15 Downwelling longwave radiation for Spring

LMST (h)	Sol 108 (W/m^2)	Sol 110 (W/m^2)	Sol 112 (W/m^2)	Average (W/m^2)
0	41.73	42.2028	42.517	42.150
1	39.657	40.1411	40.463	40.087
2	38.076	38.5591	38.881	38.505
3	36.591	37.0711	37.39	37.017
4	35.469	35.9398	36.253	35.887
5	34.418	34.8784	35.185	34.827

6	34.479	34.9356	35.239	34.885
7	34.759	35.2118	35.513	35.161
8	37.485	37.9363	38.237	37.886
9	40.69	41.1403	41.44	41.090
10	45.136	45.597	45.904	45.546
11	49.825	50.2991	50.615	50.246
12	54.708	55.2059	55.537	55.150
13	59.63	60.1528	60.5	60.094
14	62.914	63.4544	63.814	63.394
15	65.877	66.4337	66.804	66.372
16	65.47	66.0244	66.393	65.962
17	64.403	64.9515	65.316	64.890
18	60.974	61.5196	61.883	61.459
19	57.081	57.6256	57.988	57.565
20	53.518	54.0322	54.374	53.975
21	50.019	50.4978	50.816	50.444
22	46.945	47.4136	47.725	47.361
23	43.954	44.4176	44.726	44.366

The hourly values of downwelling longwave radiation for the three sols representing summer season are shown in Table 5.16.

Table 5.16 Downwelling longwave radiation for Summer

LMST (h)	Sol 234 (W/m^2)	Sol 251 (W/m^2)	Sol 270 (W/m^2)	Average (W/m^2)
0	32.794	32.990	33.199	32.994
1	31.184	31.364	31.557	31.368
2	30.111	30.240	30.375	30.242
3	29.142	29.213	29.284	29.213
4	28.425	28.434	28.436	28.432
5	27.756	27.704	27.636	27.699
6	27.898	27.776	27.631	27.768
7	28.197	28.007	27.782	27.995
8	30.171	30.024	29.851	30.015
9	32.472	32.391	32.293	32.385
10	35.442	35.425	35.399	35.422
11	38.544	38.590	38.635	38.590
12	41.454	41.562	41.677	41.564
13	44.326	44.496	44.681	44.501
14	46.147	46.378	46.631	46.385

15	47.764	48.054	48.375	48.064
16	47.553	47.873	48.228	47.885
17	46.985	47.329	47.711	47.342
18	45.057	45.351	45.673	45.360
19	42.863	43.091	43.338	43.097
20	40.727	40.990	41.276	40.998
21	38.603	38.921	39.268	38.931
22	36.535	36.812	37.113	36.820
23	34.477	34.696	34.930	34.701

The hourly values of downwelling longwave radiation for the three sols representing autumn season are shown in Table 5.17

Table 5.17 Downwelling longwave radiation for Autumn

LMST (h)	Sol 440 (W/m^2)	Sol 441 (W/m^2)	Sol 443 (W/m^2)	Average (W/m^2)
0	24.700	24.597	24.448	24.582
1	23.925	23.834	23.702	23.820
2	22.990	22.911	22.800	22.900
3	22.024	21.958	21.867	21.950
4	20.960	20.898	20.815	20.891
5	19.877	19.818	19.739	19.811
6	19.320	19.255	19.166	19.247
7	18.863	18.792	18.691	18.782
8	20.163	20.082	19.960	20.068
9	21.801	21.709	21.569	21.693
10	24.139	24.036	23.881	24.019
11	26.611	26.499	26.331	26.480
12	28.802	28.675	28.484	28.654
13	30.939	30.797	30.580	30.772
14	32.368	32.216	31.981	32.188
15	33.662	33.499	33.247	33.469
16	33.639	33.475	33.223	33.446
17	33.362	33.200	32.948	33.170
18	31.651	31.494	31.256	31.467
19	29.664	29.514	29.288	29.489
20	28.501	28.357	28.138	28.332
21	27.496	27.357	27.147	27.333
22	26.501	26.375	26.185	26.354
23	25.509	25.395	25.228	25.377

The hourly values of downwelling longwave radiation for the three sols representing winter season are shown in Table 5.18

Table 5.18 Downwelling longwave radiation for Winter

LMST (h)	Sol 610 (W/m^2)	Sol 620 (W/m^2)	Sol 631 (W/m^2)	Average (W/m^2)
0	24.492	25.080	25.670	25.081
1	23.881	24.339	24.790	24.337
2	22.964	23.293	23.599	23.285
3	21.990	22.188	22.349	22.176
4	20.715	20.890	21.023	20.876
5	19.383	19.554	19.681	19.539
6	18.608	18.808	18.966	18.794
7	17.938	18.176	18.370	18.161
8	18.899	19.191	19.446	19.179
9	20.171	20.528	20.841	20.513
10	22.316	22.788	23.229	22.778
11	24.628	25.229	25.805	25.221
12	26.415	27.172	27.925	27.171
13	28.102	29.018	29.959	29.026
14	29.380	30.378	31.411	30.390
15	30.581	31.644	32.753	31.659
16	30.791	31.845	32.942	31.859
17	30.812	31.837	32.912	31.854
18	29.547	30.519	31.523	30.530
19	28.036	28.944	29.875	28.952
20	27.046	27.918	28.881	27.948
21	26.155	26.999	27.865	27.006
22	25.590	26.368	27.166	26.375
23	25.086	25.794	26.515	25.798

The diurnal and seasonal variation of downwelling longwave radiation is shown in Fig 5.8.

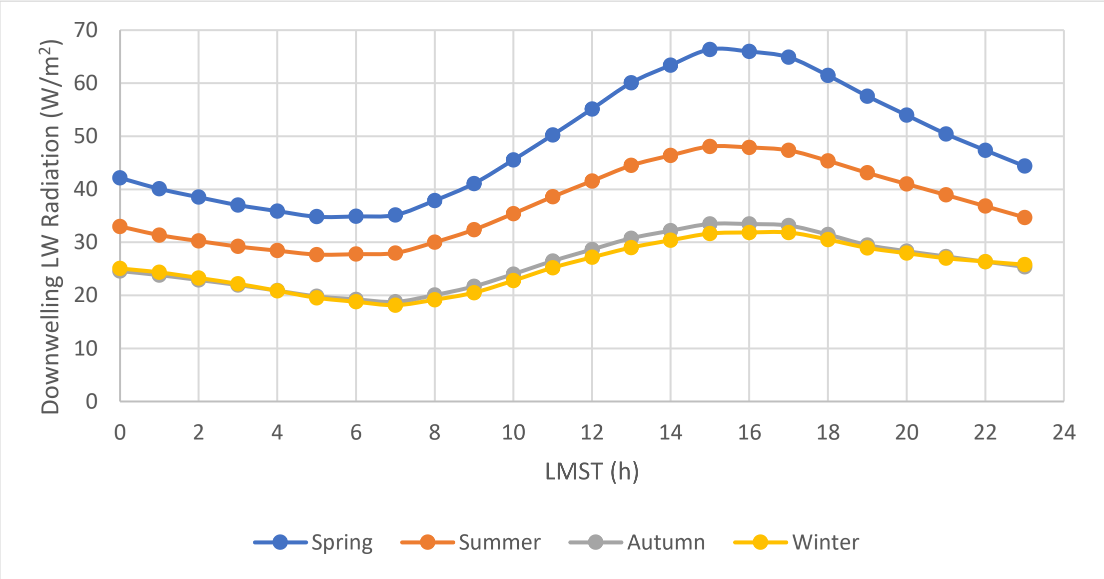

Fig 5.8 Diurnal variation of downwelling longwave radiation

It is seen that maximum downwelling longwave radiation occurs in the spring season and the lowest in the winter season. The nature of variation follows the pattern of variation of atmospheric temperatures in each of the seasons which is greatly responsible for longwave emission (Fig 5.9).

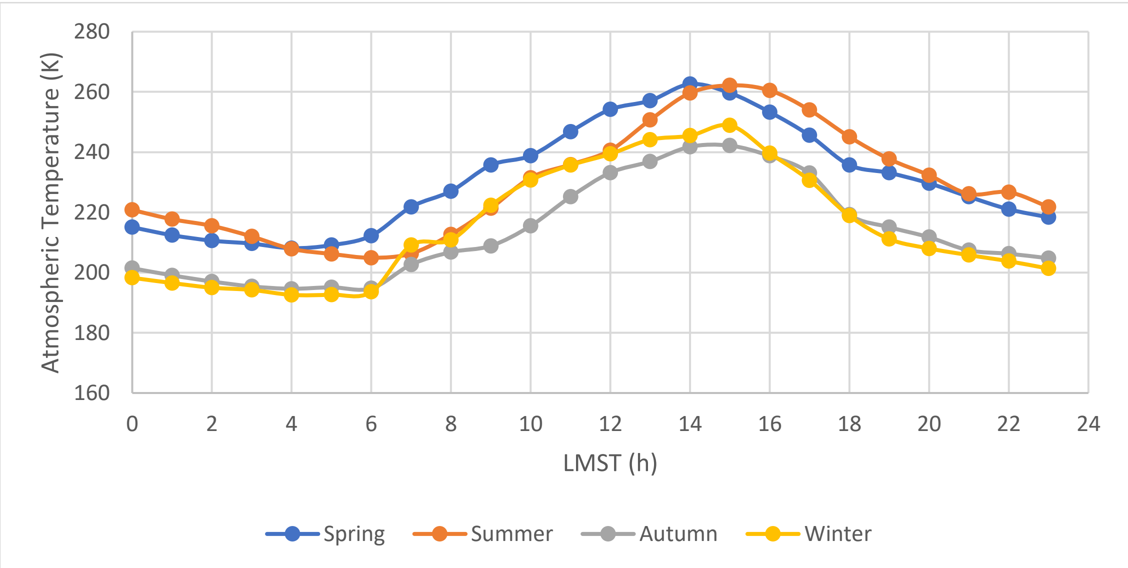

Fig 5.9 Diurnal variation of atmospheric temperatures measured by ATS

The maximum emission is found to occur around 1500 hrs to 1600 hrs LMST which is in concordance to previous observations made by Maattanen and Savijarvi (2004) in the Pathfinder lander site and Savijarvi (1995) in the Viking lander site.

5.1.5 Ground Heat Flux

The hourly values of ground heat flux as calculated by solving the surface energy budget equation for the three sols representing spring season are shown in Table 5.19.

Table 5.19 Ground Heat Flux for Spring

LMST (h)	Sol 108 (W/m^2)		Sol 110 (W/m^2)		Sol 112 (W/m^2)		Average (W/m^2)	
	Max	Min	Max	Min	Max	Min	Max	Min
0	-37.738	-49.933	-35.353	-44.739	-39.020	-48.691	-37.371	-47.788
1	-35.801	-47.389	-32.608	-44.656	-32.989	-44.000	-33.799	-45.348
2	-32.542	-43.150	-35.411	-48.610	-30.413	-40.078	-32.789	-43.946
3	-33.146	-41.549	-30.560	-40.358	-32.322	-42.901	-32.009	-41.603
4	-31.631	-41.049	-30.370	-40.256	-28.219	-35.941	-30.073	-39.082
5	-28.753	-36.716	-28.859	-33.823	-26.545	-34.580	-28.052	-35.040
6	-37.424	-47.591	-48.161	-63.378	-34.807	-46.333	-40.131	-52.434
7	-5.378	-23.956	-65.593	-87.662	-27.478	-63.510	-32.816	-58.376
8	29.530	-12.828	-70.019	-119.998	34.337	-8.004	-2.051	-46.943
9	75.397	23.415	-42.634	-128.211	75.157	32.934	35.973	-23.954
10	105.818	52.573	24.054	-33.393	99.636	28.658	76.503	15.946
11	128.006	75.065	65.239	8.752	123.009	60.049	105.418	47.955
12	133.659	83.334	109.003	56.494	131.800	82.903	124.821	74.244
13	119.079	71.268	133.927	86.926	118.786	68.875	123.931	75.690
14	121.901	67.451	137.443	96.251	82.535	38.814	113.960	67.505
15	65.534	26.353	170.212	110.913	49.628	11.533	95.124	49.600
16	14.736	-19.658	108.758	82.228	44.338	-19.377	55.944	14.398
17	-25.547	-53.519	51.757	29.545	-44.061	-79.372	-5.950	-34.448
18	-83.435	-121.591	-13.926	-37.696	-80.802	-108.940	-59.388	-89.409
19	-71.732	-94.795	-72.173	-97.101	-69.811	-96.129	-71.239	-96.008
20	-56.549	-73.064	-58.061	-75.306	-58.252	-80.348	-57.620	-76.240
21	-58.665	-76.920	-53.234	-70.318	-52.072	-68.794	-54.657	-72.011
22	-44.217	-58.397	-45.085	-61.169	-46.389	-60.947	-45.231	-60.171
23	-39.593	-50.581	-38.237	-49.776	-37.027	-47.323	-38.286	-49.227

The hourly values of ground heat flux as calculated by solving the surface energy budget equation for the three sols representing spring season are shown in Table 5.20

Table 5.20 Ground Heat Flux for Summer

LMST (h)	Sol 234 (W/m^2)		Sol 251 (W/m^2)		Sol 270 (W/m^2)		Average (W/m^2)	
	Max	Min	Max	Min	Max	Min	Max	Min
0	-65.288	-82.020	-61.426	-79.976	-63.649	-79.976	-63.454	-80.657
1	-59.980	-78.495	-60.040	-75.670	-61.593	-75.670	-60.537	-76.611
2	-57.179	-76.222	-56.361	-71.833	-60.212	-71.833	-57.917	-73.296
3	-54.172	-70.635	-55.356	-72.444	-57.236	-72.444	-55.588	-71.841
4	-49.637	-63.972	-48.453	-64.426	-52.273	-64.426	-50.121	-64.274
5	-44.593	-59.760	-50.346	-66.241	-49.352	-66.241	-48.097	-64.081
6	-40.096	-54.184	-40.404	-55.887	-44.048	-55.887	-41.516	-55.320
7	19.678	7.398	20.361	7.692	12.040	7.692	17.359	7.594
8	101.884	91.026	105.504	78.622	104.401	78.622	103.930	82.757
9	161.703	136.027	168.137	142.886	168.095	142.886	165.978	140.600
10	184.369	148.969	187.007	149.194	195.166	149.194	188.847	149.119
11	187.707	139.447	195.296	157.176	207.690	157.176	196.898	151.266
12	166.004	117.859	180.799	134.834	207.339	134.834	184.714	129.176
13	154.873	108.017	155.851	113.874	175.842	113.874	162.189	111.922
14	109.542	68.845	104.460	66.194	113.304	66.194	109.102	67.078
15	38.723	-4.338	41.700	3.860	44.658	3.860	41.694	1.127
16	-28.353	-69.727	-30.041	-73.383	-0.570	-73.383	-19.655	-72.165
17	-72.510	-107.308	-96.247	-134.956	-70.862	-134.956	-79.873	-125.740
18	-130.686	-161.818	-131.543	-163.488	-111.480	-163.488	-124.570	-162.931
19	-107.564	-135.544	-109.096	-135.436	-106.288	-135.436	-107.650	-135.472
20	-91.549	-113.840	-91.174	-116.718	-90.378	-116.718	-91.034	-115.759
21	-73.853	-95.246	-82.869	-105.101	-73.183	-105.101	-76.635	-101.816
22	-69.482	-87.774	-69.288	-87.513	-70.344	-87.513	-69.704	-87.600
23	-63.910	-78.064	-66.724	-83.127	-62.535	-83.127	-64.390	-81.440

The hourly values of ground heat flux as calculated by solving the surface energy budget equation for the three sols representing autumn season are shown in Table 5.21

Table 5.21 Ground Heat Flux for Autumn

LMST (h)	Sol 440 (W/m^2)		Sol 441 (W/m^2)		Sol 443 (W/m^2)		Average (W/m^2)	
	Max	Min	Max	Min	Max	Min	Max	Min
0	-53.522	-71.315	-50.650	-90.834	-48.671	-92.349	-50.948	-84.833
1	-52.136	-67.640	-50.993	-65.778	-48.187	-102.475	-50.439	-78.631
2	-49.890	-67.054	-44.994	-92.940	-46.368	-85.016	-47.084	-81.670
3	-44.174	-91.300	-44.037	-87.247	-44.969	-85.953	-44.394	-88.167
4	-41.509	-88.767	-47.003	-63.832	-44.298	-60.144	-44.270	-70.914
5	-43.083	-85.757	-44.685	-60.989	-44.838	-60.204	-44.202	-68.983
6	-46.054	-61.656	-42.567	-86.759	-44.556	-88.831	-44.392	-79.082
7	-1.376	-37.759	-4.983	-20.320	-4.167	-13.264	-3.509	-23.781
8	67.321	30.660	44.663	-16.136	55.399	16.264	55.794	10.263
9	105.196	47.146	92.873	48.666	100.223	55.508	99.430	50.440
10	144.503	104.242	130.558	85.283	128.928	88.031	134.663	92.519
11	167.142	131.269	137.025	91.582	134.723	87.911	146.297	103.587
12	164.727	125.298	136.854	93.941	136.683	93.287	146.088	104.175
13	149.294	108.324	122.714	82.748	124.466	82.648	132.158	91.240
14	98.181	64.187	103.934	66.062	92.383	56.724	98.166	62.324
15	66.942	26.882	51.363	15.095	49.716	12.012	56.007	17.997
16	-3.582	-42.085	-5.414	-45.638	9.039	-31.908	0.014	-39.877
17	-64.848	-102.140	-64.845	-102.567	-65.208	-101.670	-64.967	-102.126
18	-87.539	-130.127	-88.712	-128.831	-81.511	-125.559	-85.921	-128.173
19	-69.410	-91.383	-72.107	-94.837	-75.169	-114.207	-72.229	-100.142
20	-61.494	-101.539	-61.714	-97.575	-65.020	-81.588	-62.743	-93.568
21	-57.222	-77.998	-59.682	-80.767	-57.801	-96.436	-58.235	-85.067
22	-55.567	-75.358	-56.233	-74.323	-54.147	-92.505	-55.316	-80.729
23	-53.437	-73.056	-54.296	-69.304	-55.107	-75.589	-54.280	-72.650

The hourly values of ground heat flux as calculated by solving the surface energy budget equation for the three sols representing winter season are shown in Table 5.22

Table 5.22 Ground Heat Flux for Winter

LMST (h)	Sol 610 (W/m^2)		Sol 620 (W/m^2)		Sol 631 (W/m^2)		Average (W/m^2)	
	Max	Min	Max	Min	Max	Min	Max	Min
0	-26.677	-35.880	-27.718	-38.286	-35.695	-51.621	-30.030	-41.929
1	-22.310	-29.613	-27.202	-35.633	-35.207	-50.057	-28.239	-38.434
2	-20.148	-26.410	-24.452	-31.125	-35.336	-49.804	-26.645	-35.780
3	-20.812	-28.643	-20.302	-24.755	-35.381	-52.324	-25.498	-35.241
4	-21.889	-30.736	-17.334	-21.339	-31.369	-43.148	-23.531	-31.741
5	-22.123	-30.384	-25.551	-30.369	-29.920	-40.297	-25.865	-33.683
6	-29.260	-38.738	-33.201	-44.154	-33.610	-46.148	-32.023	-43.013
7	-20.064	-72.660	-10.146	-22.524	-3.546	-20.113	-11.252	-38.432
8	39.143	-1.773	13.388	-33.532	48.153	10.623	33.561	-8.227
9	47.556	3.220	37.481	-23.332	86.094	47.068	57.044	8.986
10	90.540	47.150	77.188	32.386	84.411	29.589	84.046	36.375
11	94.500	44.904	95.743	50.812	102.010	52.159	97.417	49.292
12	105.257	65.637	104.558	64.220	104.590	59.765	104.802	63.207
13	102.952	56.054	92.059	50.894	105.835	74.367	100.282	60.438
14	89.134	50.204	94.390	50.003	80.167	48.298	87.897	49.502
15	44.849	14.770	70.979	43.812	42.621	12.736	52.816	23.772
16	17.337	-2.374	31.165	6.776	17.633	-26.766	22.045	-7.454
17	-42.255	-62.401	-42.448	-65.423	-55.277	-91.783	-46.660	-73.202
18	-57.029	-70.538	-52.949	-68.808	-73.988	-96.934	-61.322	-78.760
19	-43.131	-54.969	-45.436	-61.345	-56.749	-75.930	-48.439	-64.082
20	-39.273	-53.825	-41.614	-55.558	-51.280	-70.654	-44.056	-60.013
21	-38.470	-49.775	-31.446	-40.821	-45.881	-61.043	-38.599	-50.546
22	-34.431	-45.657	-30.319	-35.931	-38.856	-52.076	-34.535	-44.555
23	-27.106	-36.883	-30.320	-39.654	-38.084	-51.586	-31.837	-42.708

A plot of the net surface energy fluxes in spring and summer is shown in Fig 5.10 and Fig 5.11.

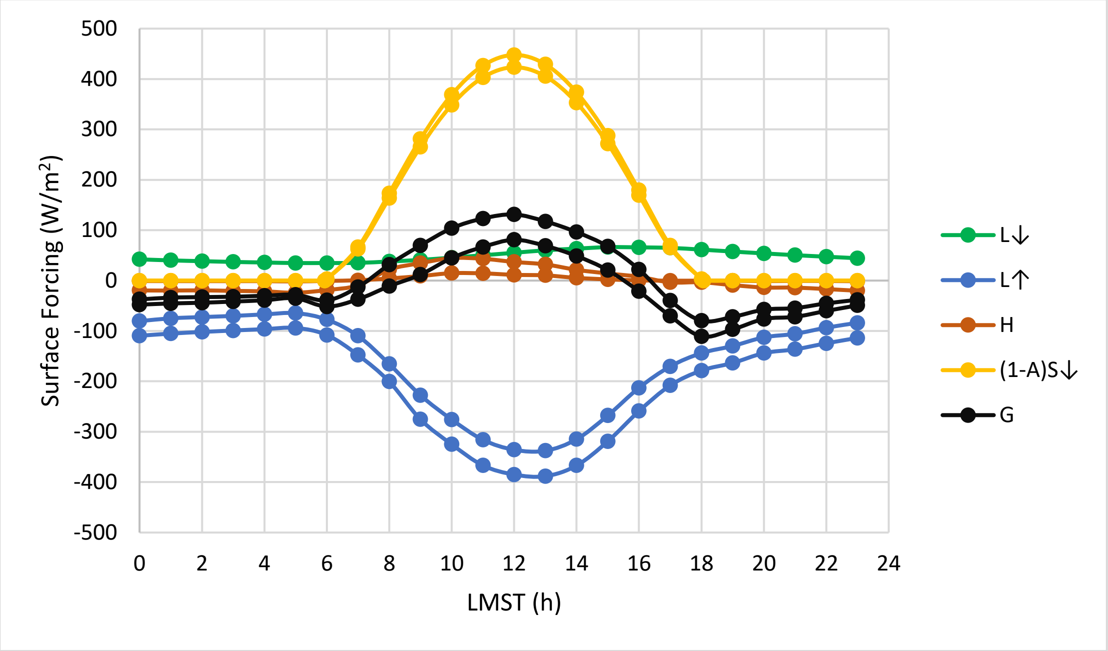

Fig 5.10 Surface energy fluxes in spring

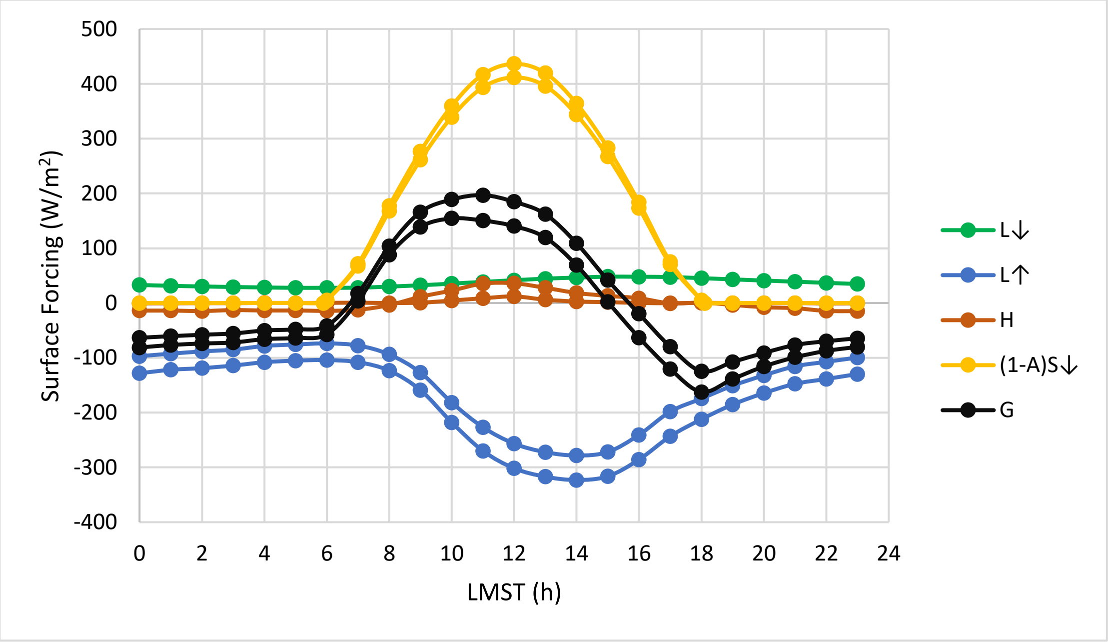

Fig 5.11 Surface energy fluxes in summer

A plot of the net surface energy fluxes in autumn and winter is shown in Fig 5.12 and Fig 5.13.

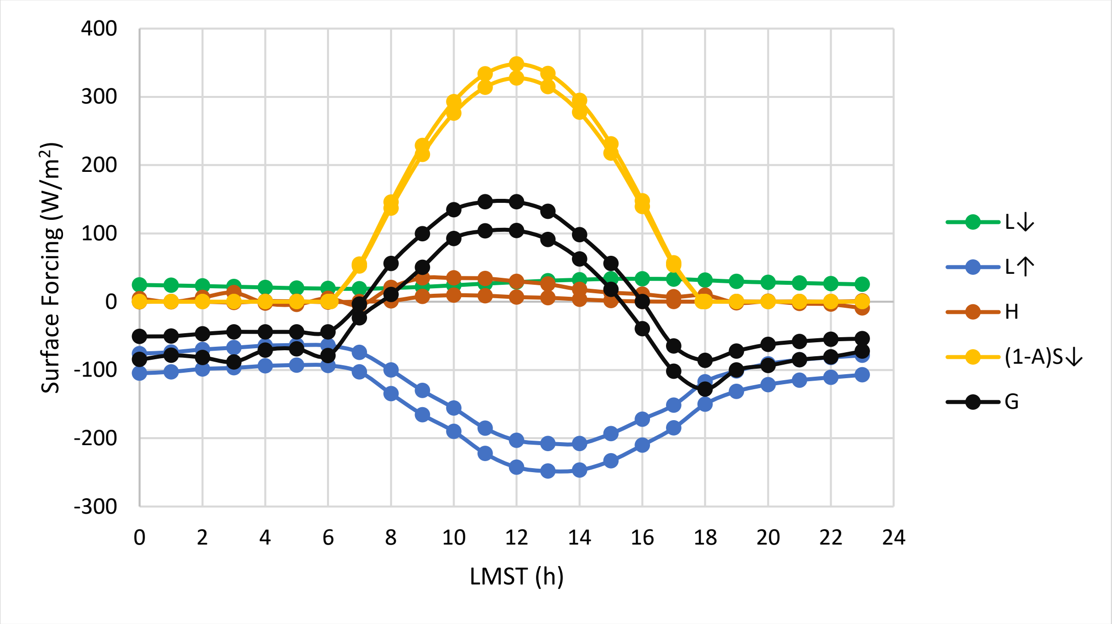

Fig 5.12 Surface energy fluxes in autumn

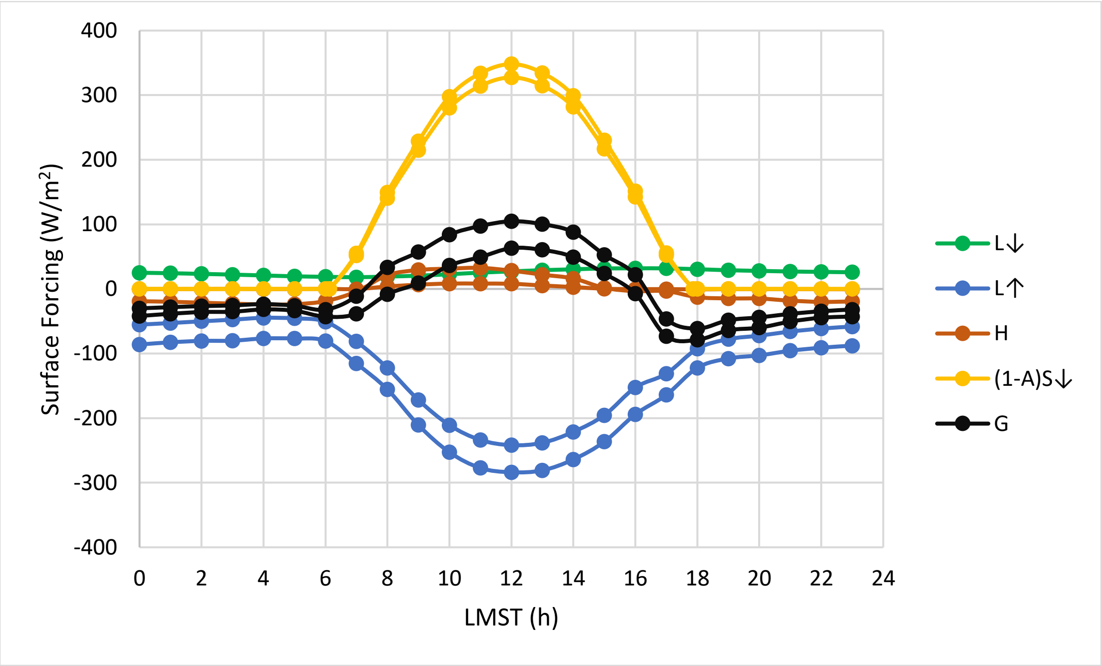

Fig 5.13 Surface energy fluxes in winter

The diurnal and seasonal variation of maximum and minimum ground heat flux is shown in Fig 5.14 and Fig 5.15.

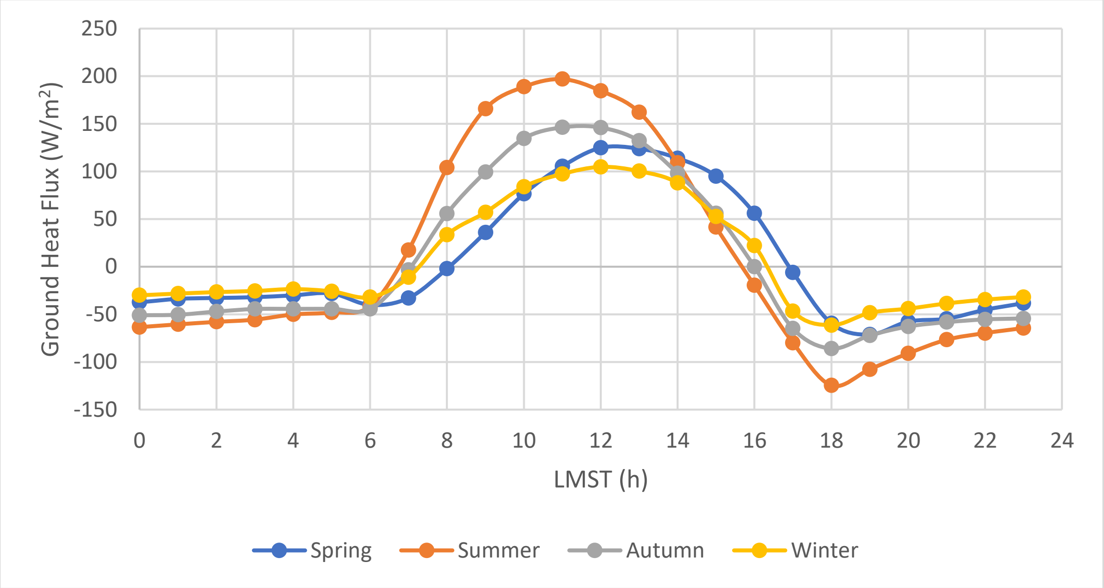

Fig 5.14 Diurnal variation of maximum ground heat flux

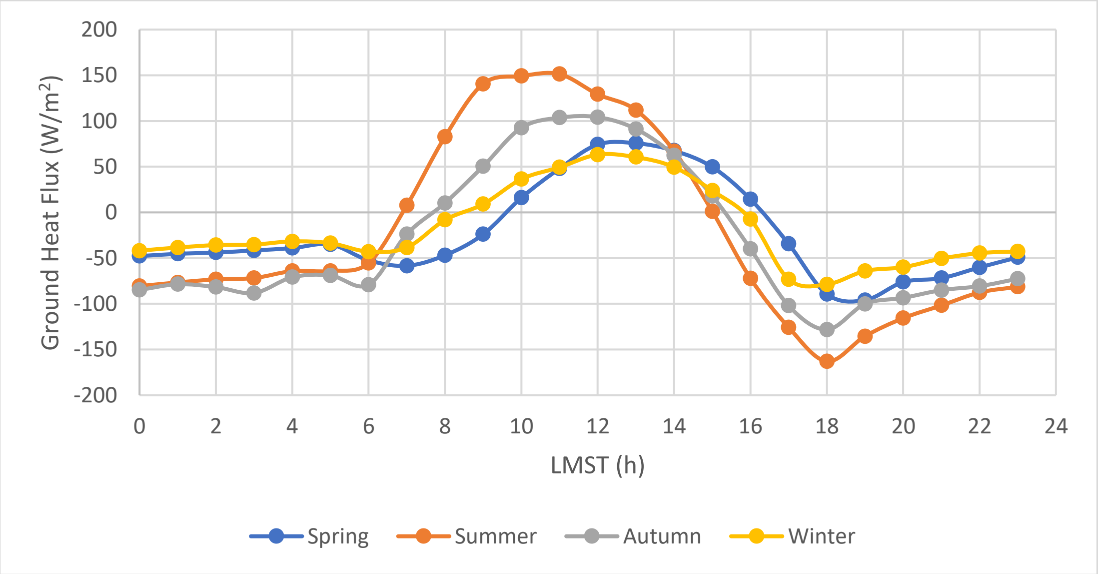

Fig 5.15 Diurnal variation of minimum ground heat flux

It is seen that the dominant terms of the SEB are downwelling SW radiation and upwelling longwave radiation which are at least ten times higher than the remaining terms. It is to be noted that though the magnitudes of downwelling longwave radiation and sensible heat flux are high (around 50W/m^2 and 20W/m^2 respectively), they are not significant enough to distinctly influence the nature of variation of the energy budget. Maximum ground heat storage is found to occur in the summer season, followed by autumn, spring and winter.

A positive value of ground heat storage indicates surface heating and a negative value indicates cooling. Cooling of the surface occurs during the night-time and is caused predominantly by greater magnitude of upwelling longwave radiation whereas heating of the surface occurs during the day and is caused due to greater downwelling radiations.

5.2 Curiosity derived thermal inertia calculations

Based on the corresponding MastCam images obtained for the sols selected for the study, the following values of volumetric heat capacity are taken.

Table 5.23 Parameters used for solving heat conduction equation

Sol	T_{gmean} (K)	T_{gmean} (min.) (K)	T_d (K)	Volumetric heat capacity ρC_p ($J\ m^{-3}\ K^{-1}$)
108	233.811	195.498	215	1.30×10^6
110	234.312	195.485	215	1.30×10^6
112	234.546	194.540	215	1.30×10^6
234	232.309	200.203	217	1.70×10^6
251	232.343	200.240	217	1.70×10^6
270	230.413	202.016	217	1.70×10^6
440	218.666	194.336	207	1.60×10^6
441	220.259	194.129	207	1.60×10^6
443	220.745	194.209	207	1.60×10^6
610	214.640	179.413	198	1.25×10^6
620	215.078	177.417	198	1.25×10^6
631	218.665	185.424	202	1.25×10^6

The Mastcam and Navcam images based on which volumetric heat capacity values were estimated are shown in Fig 5.12, Fig 5.13 and Fig 5.14. It is seen that a dense lacustrine mudstone deposit is found in Yellowknife Bay and Coopers Town whereas a sparse distribution of basaltic rock material is found in Point Lake and near Mt. Remarkable. Therefore, higher volumetric heat capacities are assumed in Sols 234, 251, 270 (Yellowknife Bay) and Sols 440, 441 and 443 (Coopers Town) when compared to the other sols chosen for study.

Sol 108 (0108ML0006830000103244E01_DRXX)

Sol 110 (0110ML0006860010103449E01_DRXX)

Sol 112 (0112ML0006910030103669E01_DRXX)

Fig 5.16 MASTCAM images acquired on Sol 108, Sol 110 and Sol 112

Sol 234 (0234MR0011140300203161E02_DRLX)

Sol 251 (0251ML0011790000106115E01_DRXX)

Sol 270 (0270ML0011820000106131C00_DRCX)

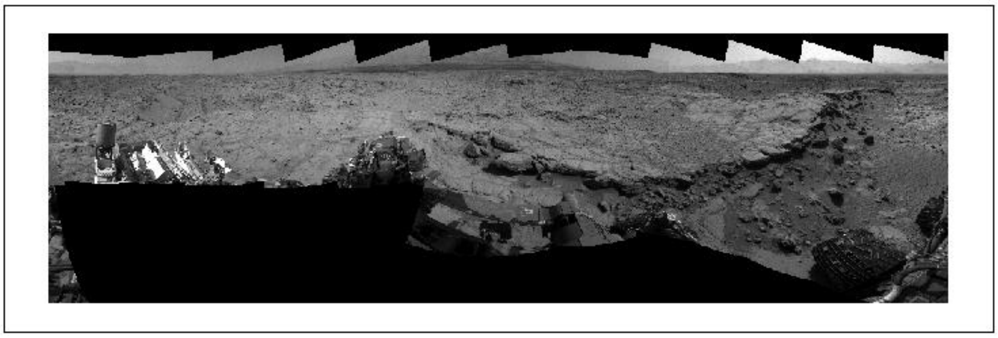

Sol 441 (N_A000_0440_ILT022CYP_S_0000_UNCORM2)

Fig 5.17 MASTCAM images acquired on Sol 234, Sol 251, Sol 270 and NAVCAM mosaic acquired on Sol 441

Sol 610 (0610ML0025680000301576E01_DRXX)

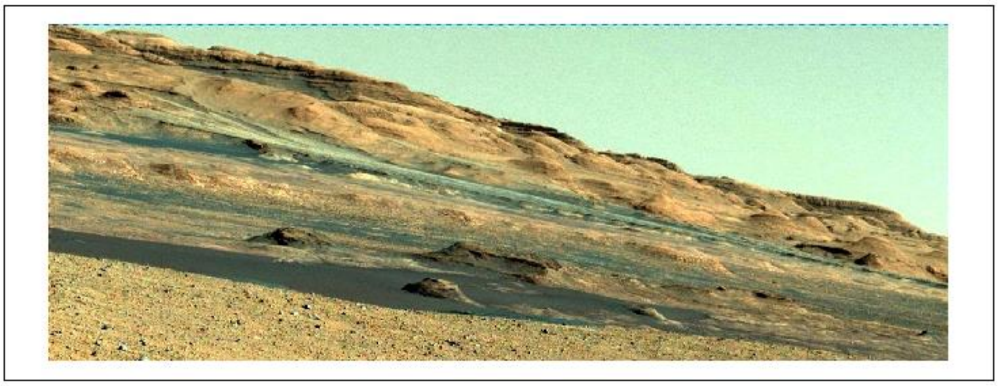

Sol 620 (0620ML0026030040205113E01_DRXX)

Sol 631 (0631ML0026080000302421E01_DRXX)

Fig 5.18 MASTCAM images acquired on Sol 610, Sol 620 and Sol 631

G* is calculated using Eqn. 23 and plotted along with average value of G at different thermal inertia values on a diurnal basis for each sol in Fig 5.19 to Fig 5.30.

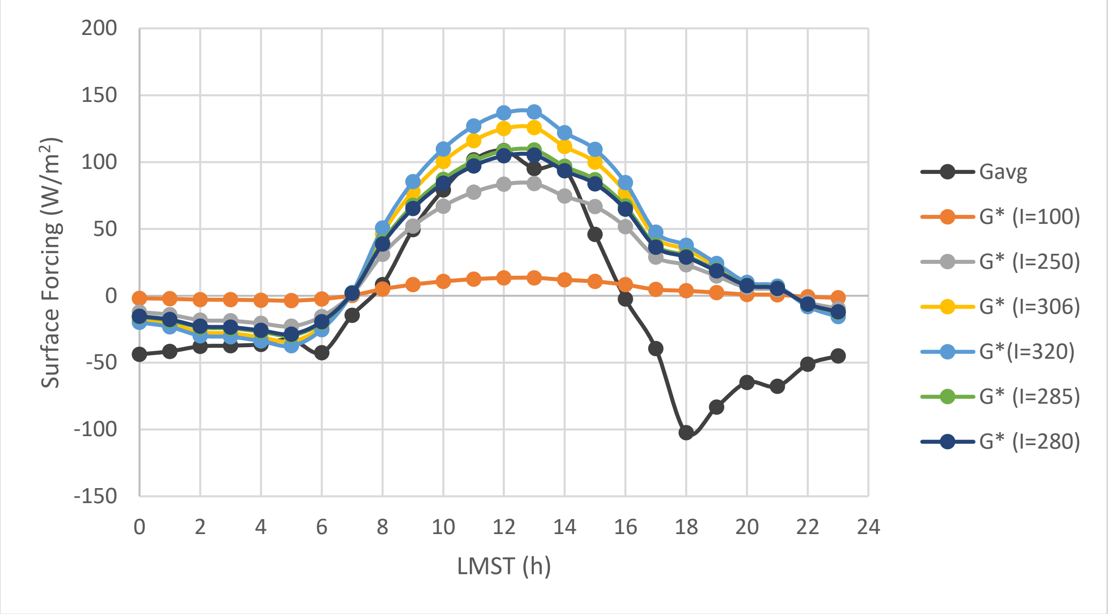

Fig 5.19 Comparison of G and G* (Sol 108)

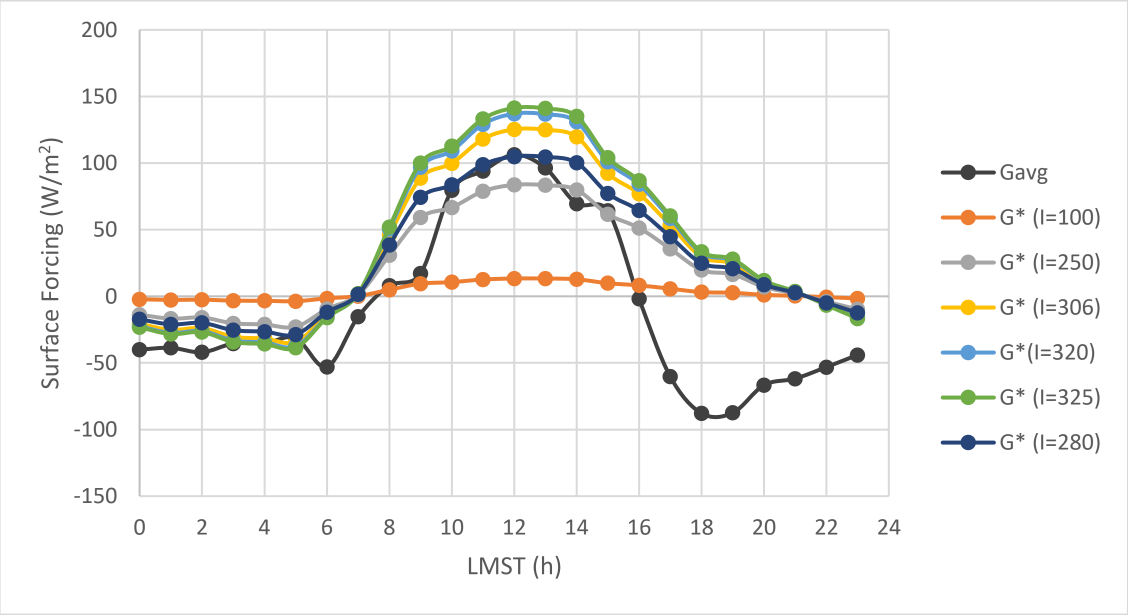

Fig 5.20 Comparison of G and G* (Sol 110)

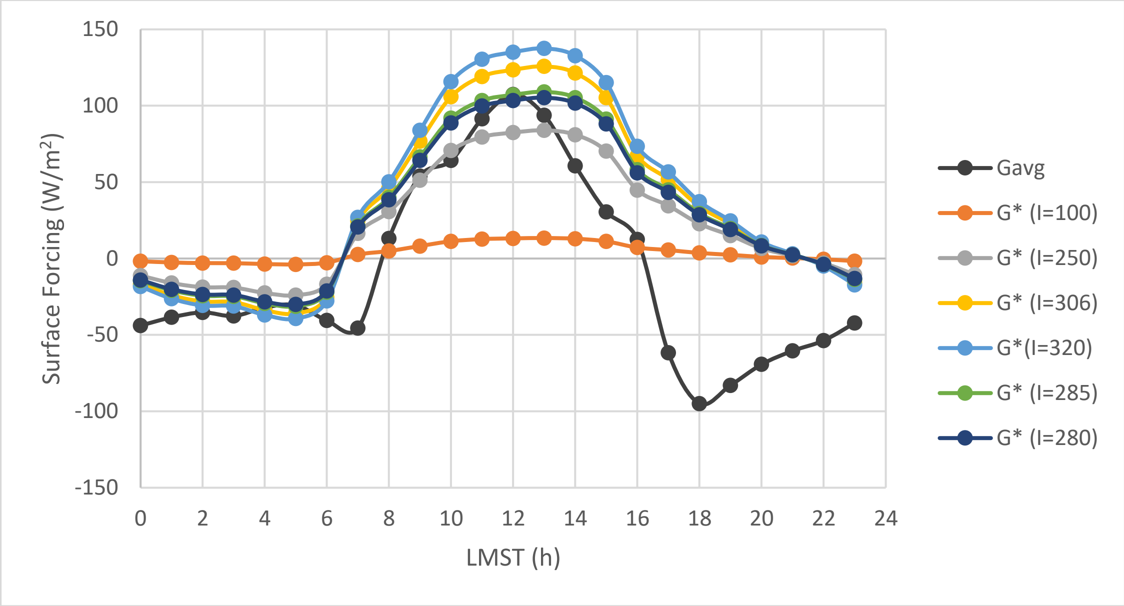

Fig 5.21 Comparison of G and G* (Sol 112)

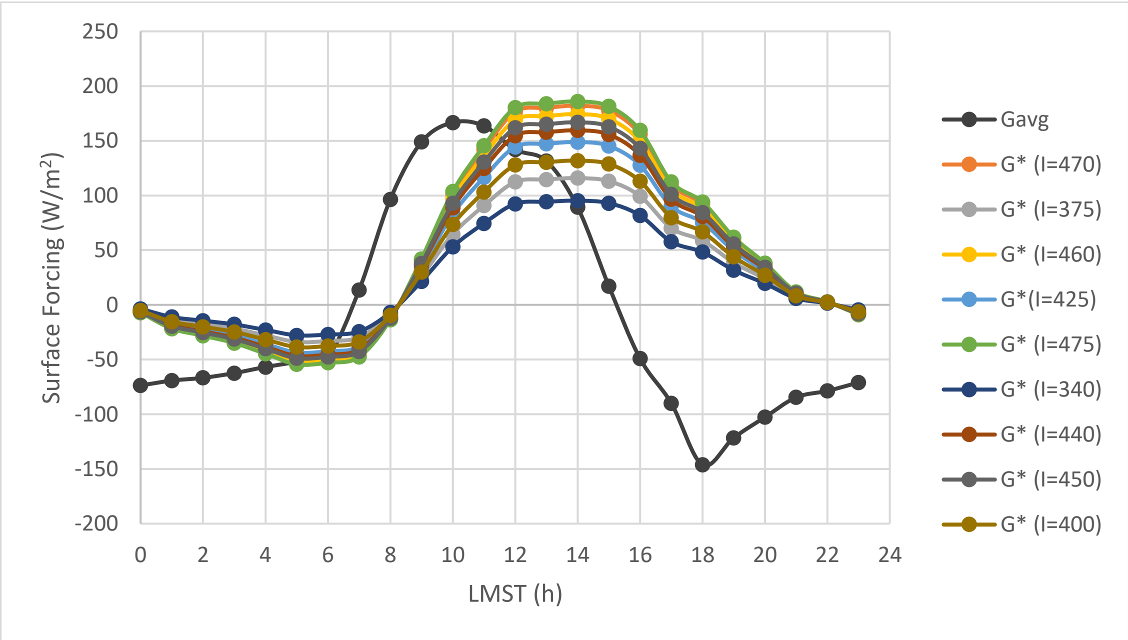

Fig 5.22 Comparison of G and G* (Sol 234)

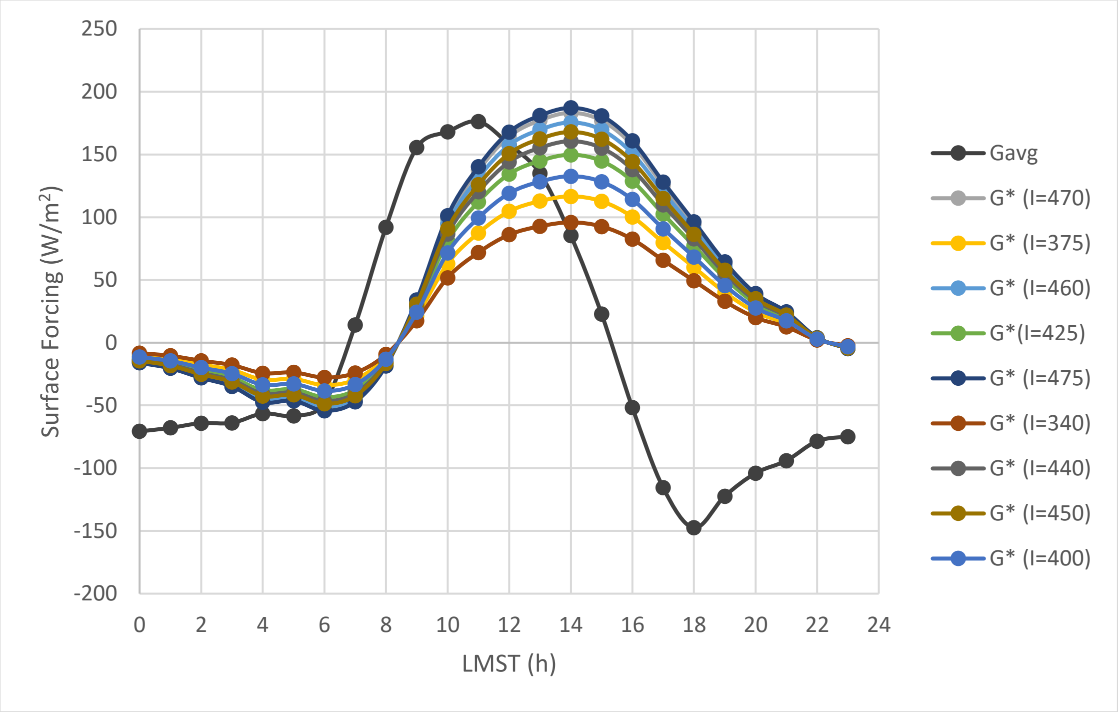

Fig 5.23 Comparison of G and G* (Sol 251)

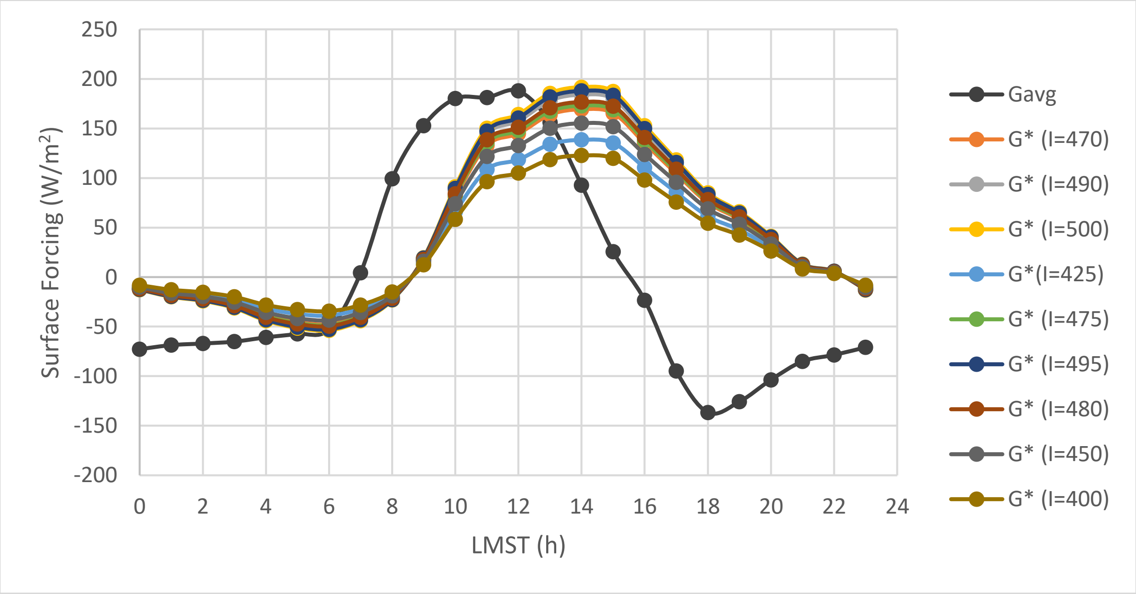

Fig 5.24 Comparison of G and G* (Sol 270)

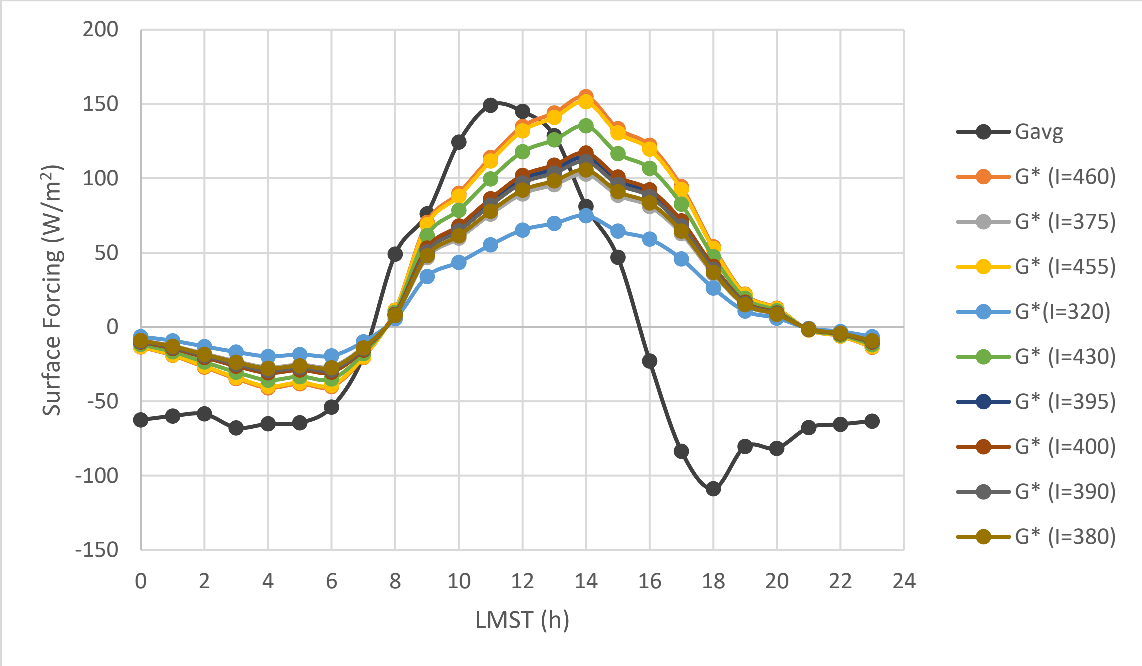

Fig 5.25 Comparison of G and G* (Sol 440)

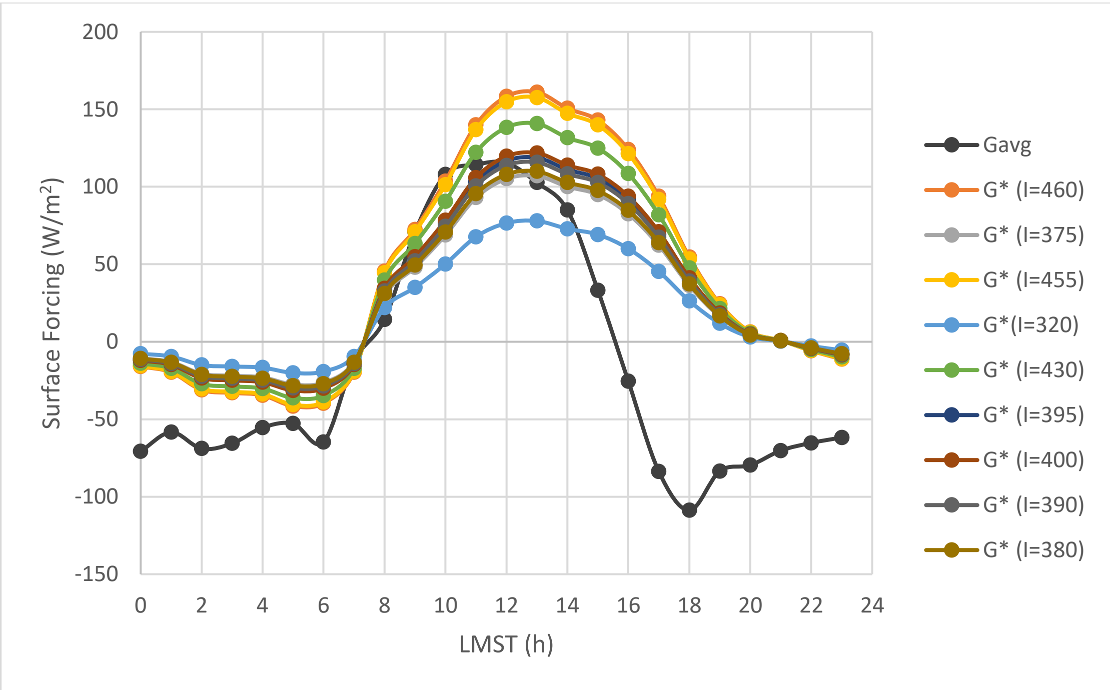

Fig 5.26 Comparison of G and G* (Sol 441)

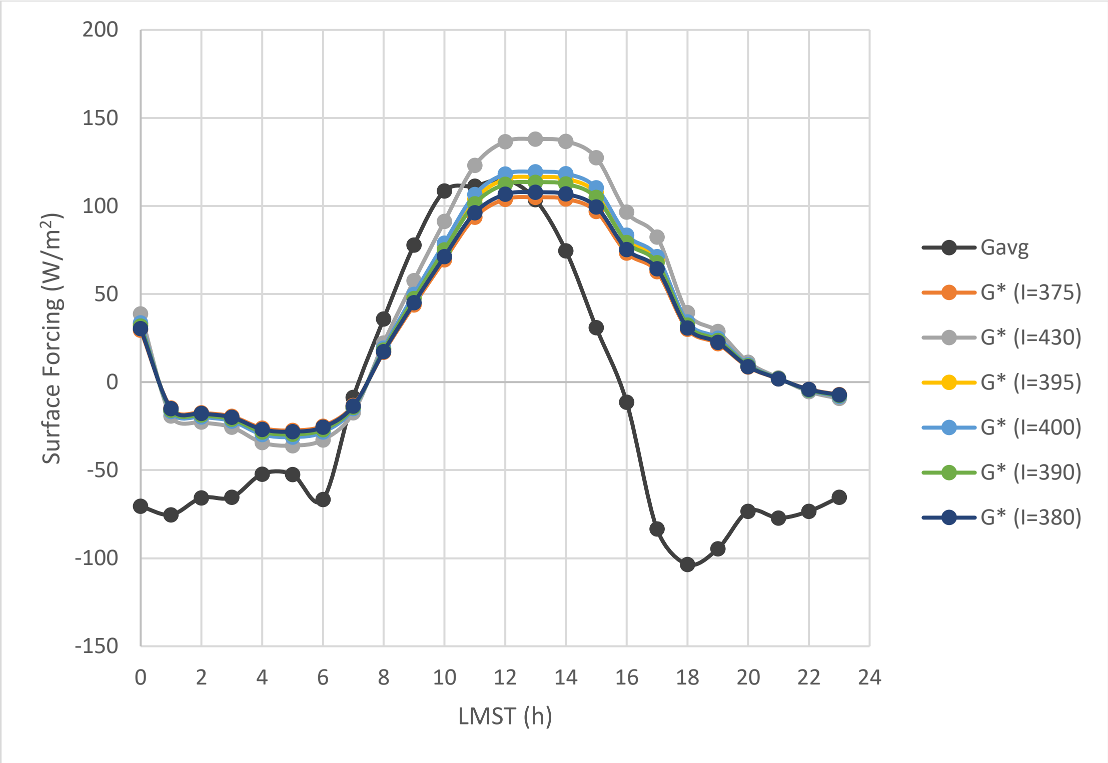

Fig 5.27 Comparison of G and G* (Sol 443)

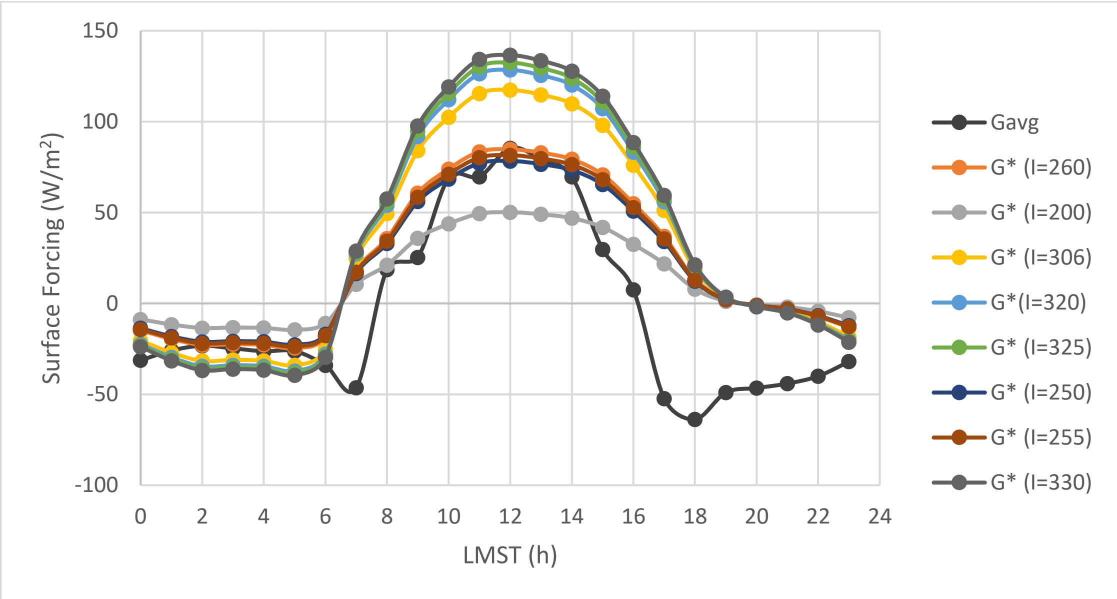

Fig 5.28 Comparison of G and G* (Sol 610)

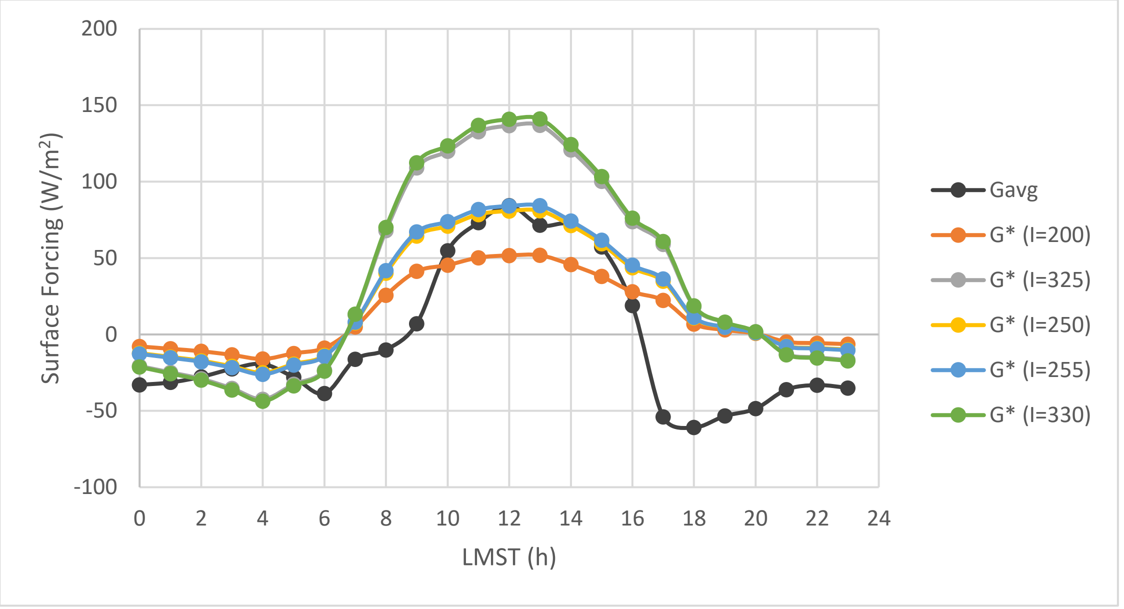

Fig 5.29 Comparison of G and G* (Sol 620)

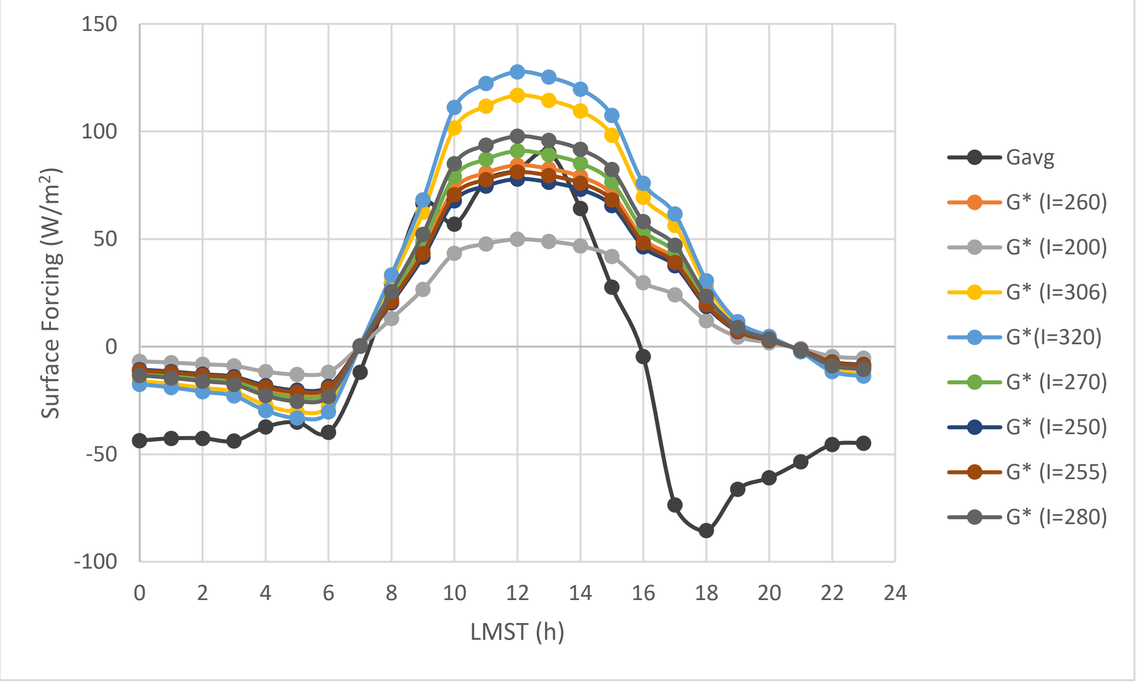

Fig 5.30 Comparison of G and G* (Sol 631)

The values of thermal inertia obtained by comparing G and G* for each sol is shown in Table 5.24

Table 5.24 Curiosity derived thermal inertia values for each sol

Location	Sol	Thermal inertia ($J\ m^{-2}\ K^{-1}\ s^{-1/2}$)	Average thermal inertia ($J\ m^{-2}\ K^{-1}\ s^{-1/2}$)	Average uncertainty in estimation (%)
Point Lake	108	285	283.333	12.35
	110	280		
	112	285		
Yellowknife Bay	234	460	475	4.54
	251	470		
	270	495		
Coopers Town	440	455	415	6.76
	441	395		
	443	395		
Mt. Remarkable	610	260	261.666	10.54
	620	255		
	631	270		

Thermal inertia is the ability of a surface to store heat during the day and re-radiate it during the night. It is defined as the degree of slowness with which the temperature of a body approaches that of its surroundings. Higher the thermal inertia, greater is the heat entrainment by the surface. Greater the particle size, greater will be its density and thermal heat capacity and thereby, greater will be its thermal inertia. Hence, as expected, greater values of thermal inertia are obtained for Yellowknife Bay and Cooperstown, which comprise of dense lacustrine mudstone strata when compared to the sparse distribution of basaltic rocks over Point Lake and Mt. Remarkable.

These values are in excellent concordance with the computations made by Vasavada et al. (2017) shown in Table 5.25.

Table 5.25 Thermal inertia calculations by Vasavada et al. (2017)

Sol	Geological interpretation	Albedo	Average thermal inertia (J m^{-2} K^{-1} $s^{-1/2}$)
103-110	Unsorted loose material	0.19	250
167-271	Lacustrine mudstone (Bedrock with fines)	0.22	430
441-452	Varied terrain	0.16	430
610-629	Unsorted loose material	0.21	250

5.3 THEMIS derived thermal inertia

The thermal inertia was processed from five night-time THEMIS images at different solar longitudes and their results are tabulated in Table 5.26. It is to be noted that, due to non-availability of THEMIS data in the winter season over Gale crater, thermal inertia in winter could not be calculated.

Table 5.26 THEMIS derived thermal inertia

Dataset ID	L_s (°)	LMST (h)	Thermal Inertia (J m^{-2} K^{-1} $s^{-1/2}$)			
			Point Lake	Yellowknife Bay	Coopers Town	Mt. Remarkable
I35195003	12.07	3.40	518.638	521.374	357.217	446.978
I54144002	95.26	5.41	576.340	581.795	456.333	440.340
I49174003	244.49	4.48	317.475	334.724	230.888	221.652
I50098003	292.15	3.83	387.191	396.063	253.442	266.430
I01350002	352.92	3.25	505.113	560.889	337.677	393.029

The thermal inertia maps generated from the five chosen THEMIS night time images are shown in Fig 5.31, Fig 5.32, Fig 5.33, Fig 5.34 and Fig 5.35.

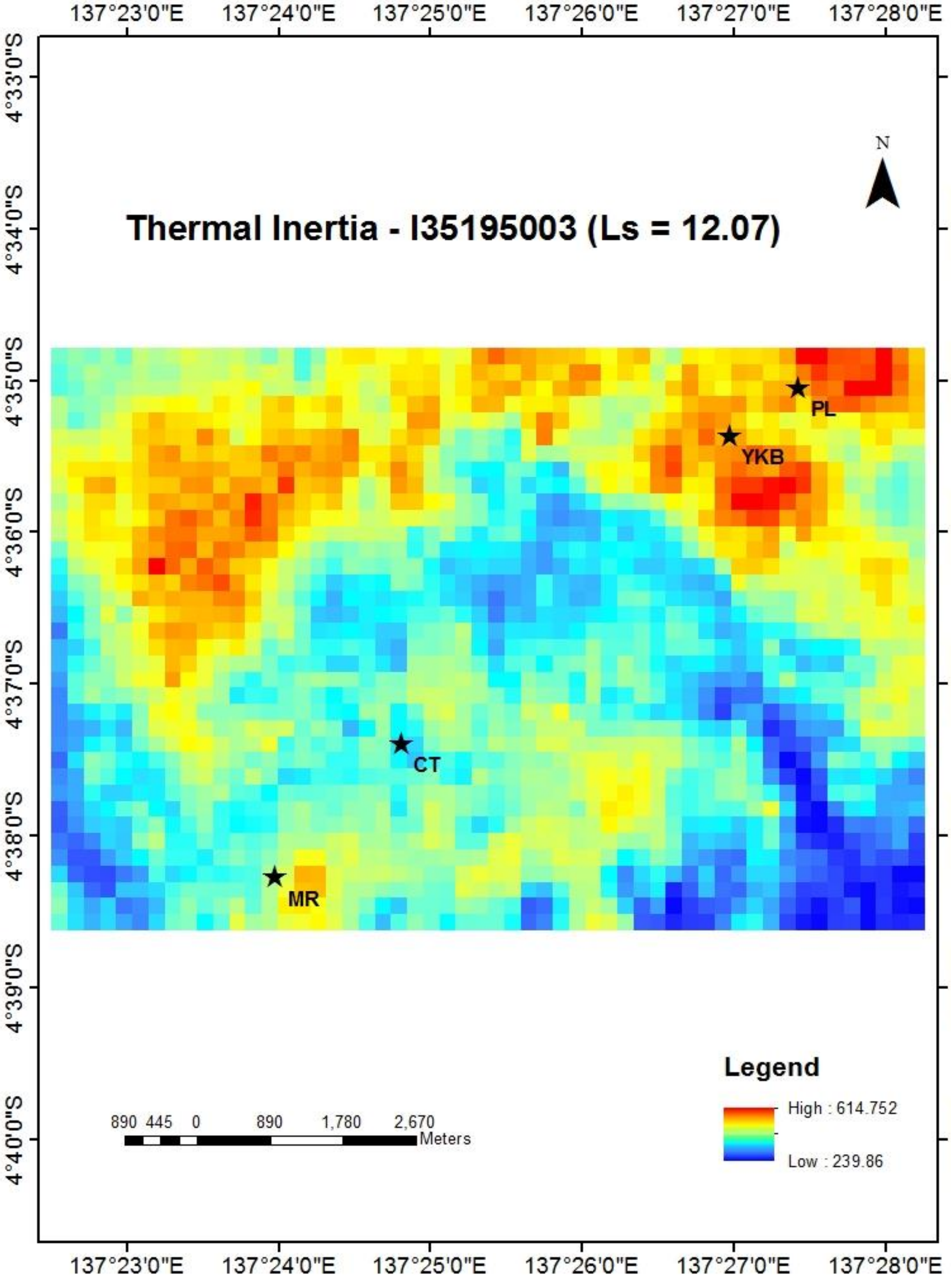

Fig 5.31 Thermal inertia - I35195003

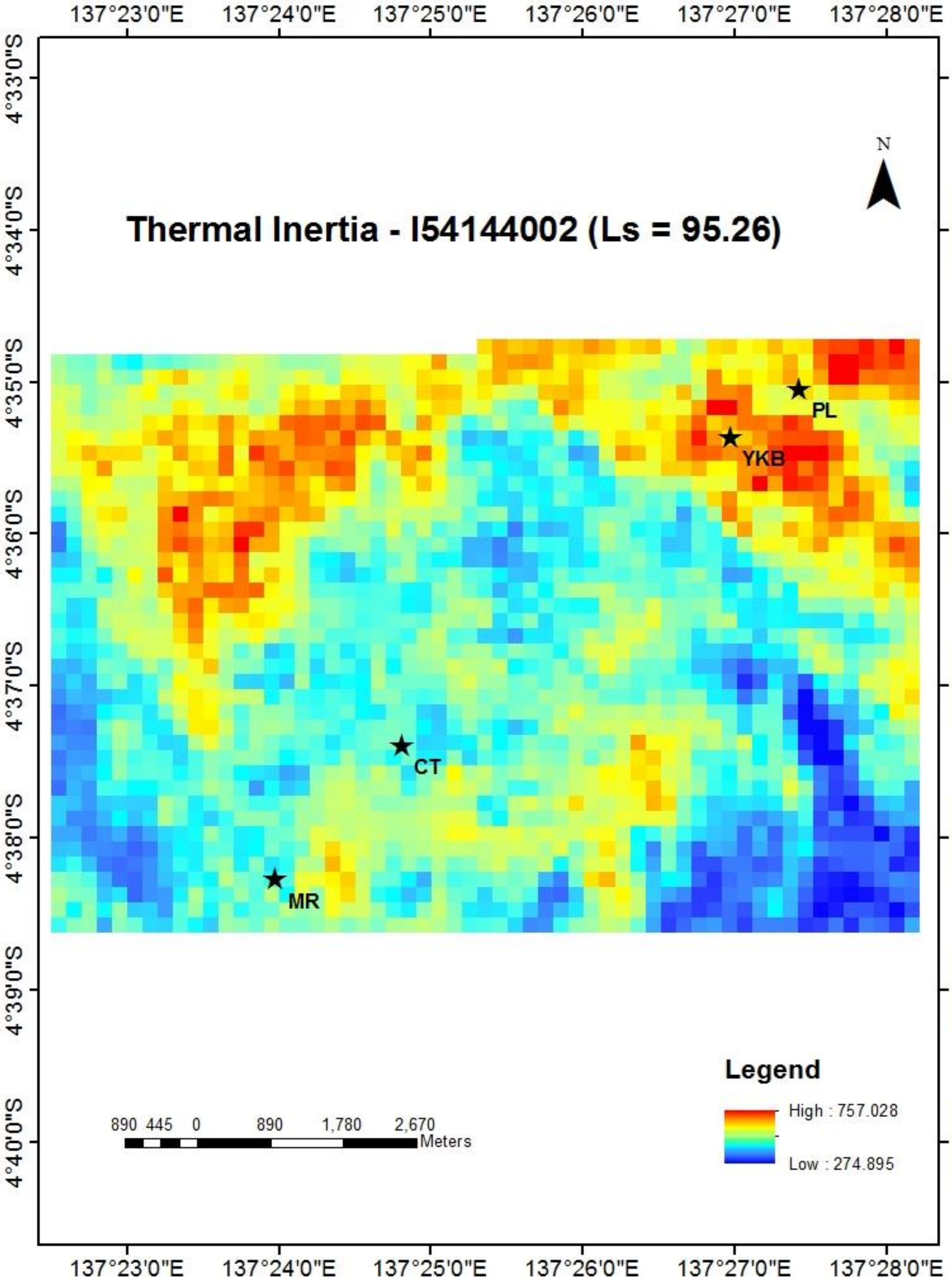

Fig 5.32 Thermal inertia - I54144002

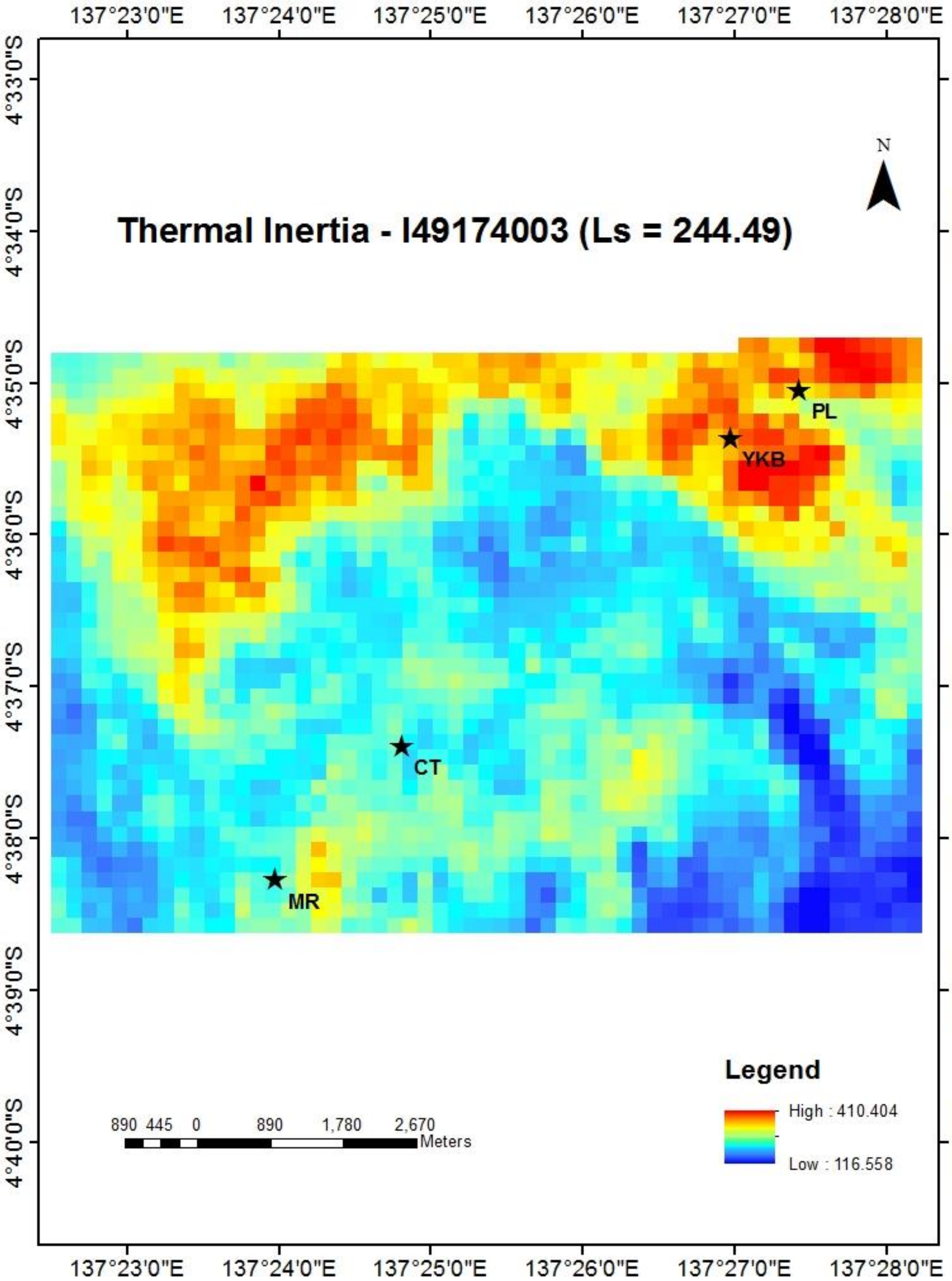

Fig 5.33 Thermal inertia - I49174003

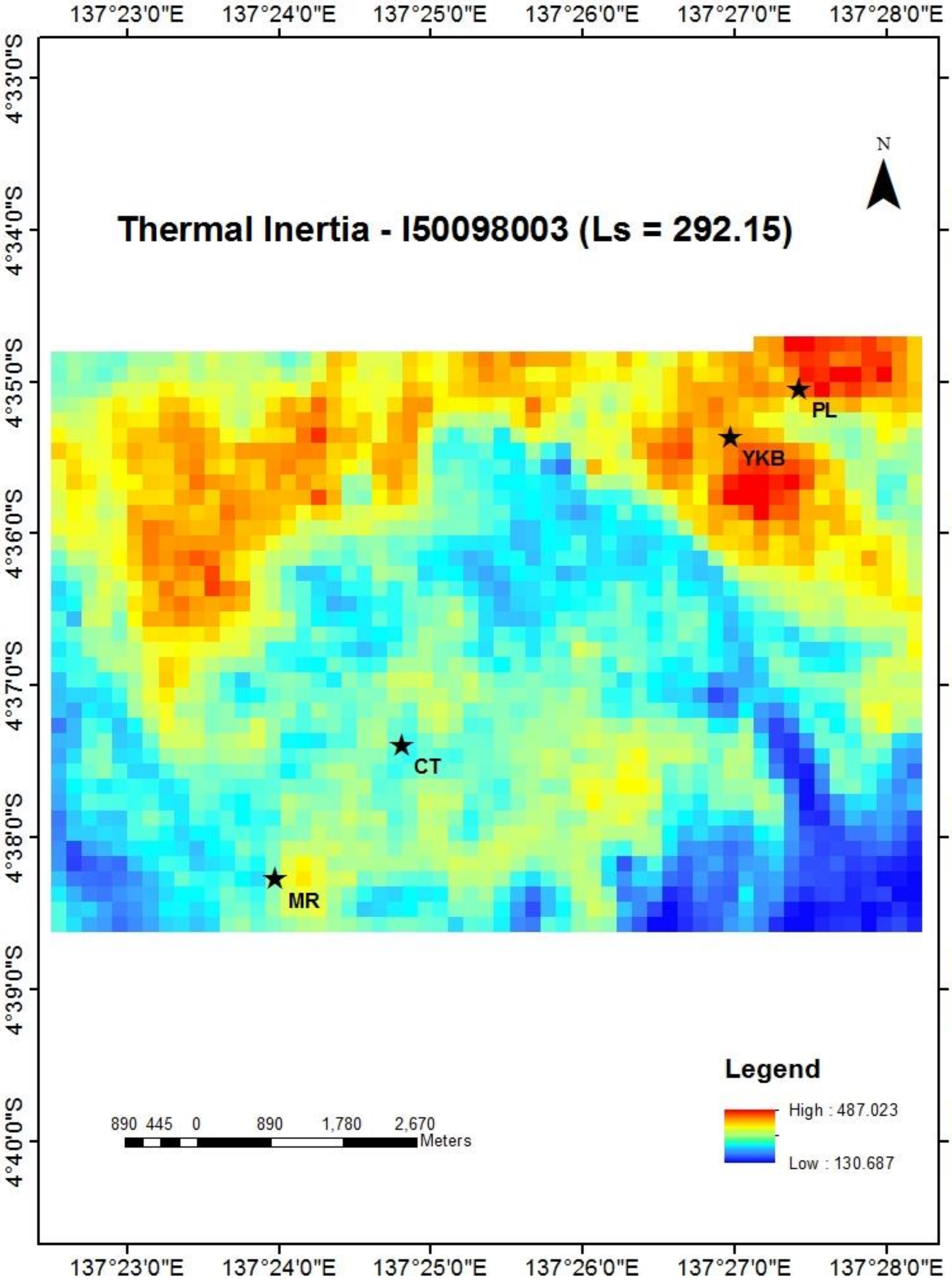

Fig 5.34 Thermal inertia – I50098003

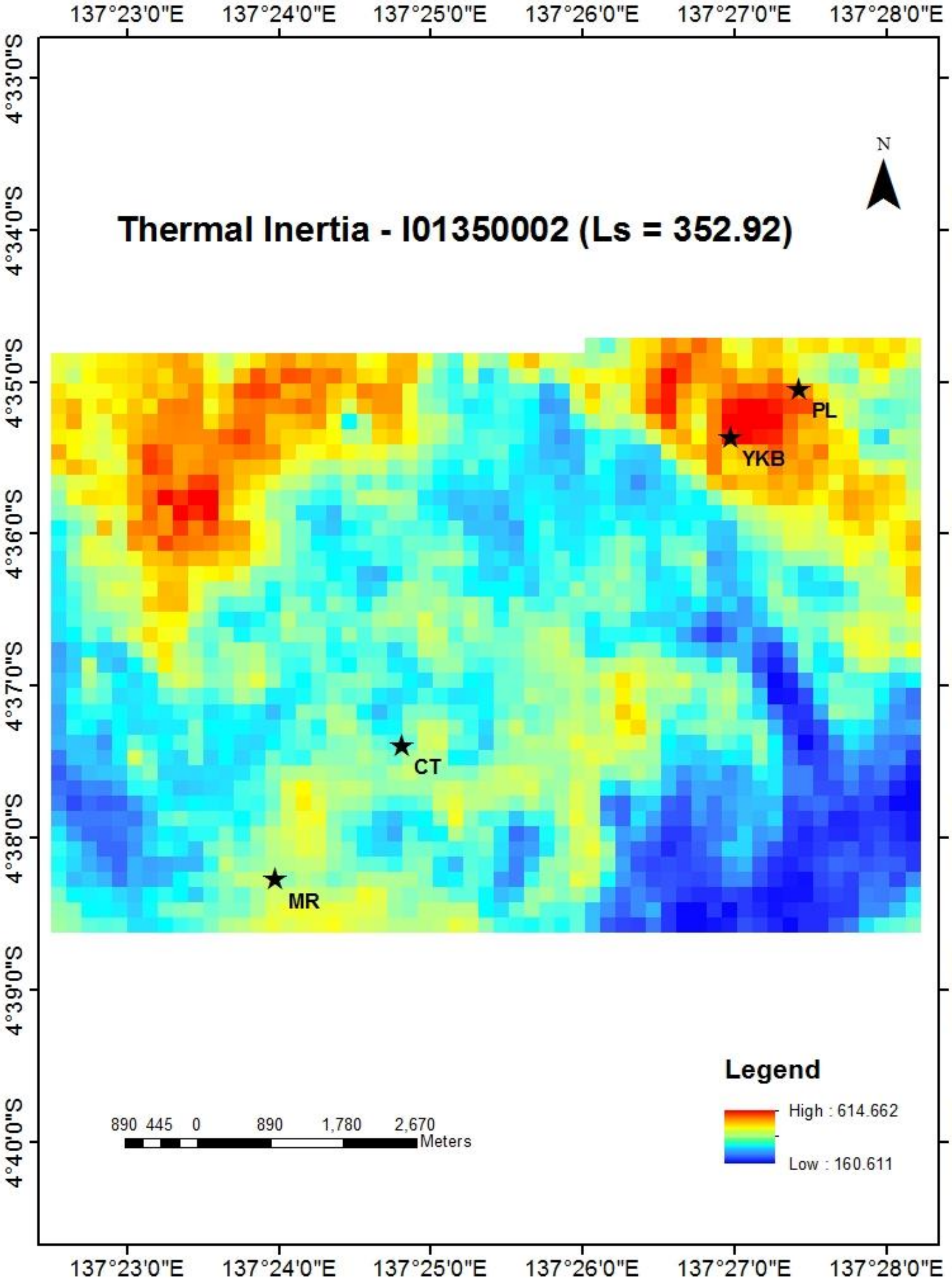

Fig 5.35 Thermal inertia – I01350002

It is seen here that thermal inertia is not constant over varying solar longitudes, as thought so. A plot of the variation of thermal inertia at the four chosen study locations shows that the thermal inertia variation is sinusoidal with minimum thermal inertia occurring at solar longitudes of 250° to 270° (Fig 5.36).

A study of the nature of Mars' seasonal cycle indicates that the dust season extends from L_s = 180° to L_s = 360°, covering the spring and summer seasons in the Southern hemisphere. As the dust season progresses, greater quantity of dust is deposited on the Martian surface, thereby obscuring and covering the bed rock lying underneath. Dust or any other fine grained soil matter do not have as much capability as large hard rocks to store heat, thereby reducing the thermal inertia of the top layer of the surface.

As heavy gusts of winds continue to blow through the end of summer into autumn, the deposited dust is slowly removed by the wind and the underlying bedrock is exposed, thereby increasing the thermal inertia of the top surface layer.

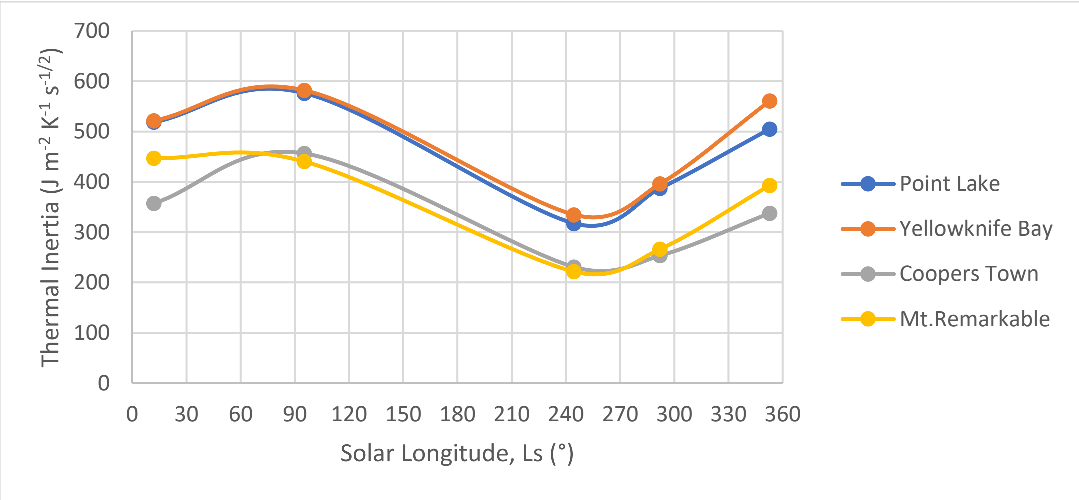

Fig 5.36 Seasonal variation of thermal inertia at the four study locations

There may be three potential causes for seasonal variations of thermal inertia (Fergason, 2013):

1. Sub-surface layering
2. Atmospheric variations
3. Omission of critical physics in the thermal models

Sub-surface layers of different physical properties such as a thin dust layer overlying bedrock contribute to the observed surface temperature and therefore thermal inertia in a non-linear manner. A one layer model may not accurately produce diurnal/seasonal changes in surface temperatures under these conditions and this will result in different thermal inertia values to be derived for different seasons for the same surface.

Atmospheric variations also change with season and if not adequately accounted for in the thermal model, can result in seasonal changes in thermal inertia that could be misinterpreted as subsurface layers.

Moreover, omission of important physical phenomena such as water-ice clouds or near surface winds and the effect of their turbulence from thermal models can also cause inaccuracies in surface temperature and hence thermal inertia.

Seasonal changes were also observed by Putzig et al. (2005). He observed a seasonal variation of around 200 tiu in mid latitude and 600 tiu or greater in the polar regions.

The thermal inertia obtained by processing THEMIS images is valid only for that season in which the thermal image has been acquired. Hence, thermal inertia at a single location alone can be compared with Curiosity derived thermal inertia as measurements by Curiosity at the four locations chosen for study, lie in four different seasons.

Thermal inertia values were also obtained by running a thermal model on THEMIS night-time images. The values obtained are in very good agreement with Curiosity derived thermal inertia values for the locations chosen for study with an error less than 20% (Table 5.27).

Table 5.27 Comparison of Curiosity and THEMIS derived thermal inertia

Location	Season	L_s (°)	Curiosity TI ($J\ m^{-2}\ K^{-1}\ s^{-1/2}$)	THEMIS TI ($J\ m^{-2}\ K^{-1}\ s^{-1/2}$)	Percent error (%)
Point Lake	Spring	244.49	283.333	317.475	12.05
Yellowknife Bay	Summer	352.92	475.000	560.889	18.08
		292.15		396.063	16.61
Coopers Town	Autumn	12.07	415.000	357.217	13.92
		95.26		456.333	9.95

5.4 Particle size estimation from THEMIS thermal inertia

The range of thermal inertias for different particle sizes as per the USGS classification scheme calculated using Eqn. 26 is shown in Table 5.28. The mean atmospheric pressure is kept at 800 Pa (~6 torr) and the average volumetric heat capacity of the area is taken to be 1.3×10^{6} J m^{-3} K^{-1}.

Table 5.28 Characteristics of Martian surface materials based on USGS soil classification scheme

Particle Size (μm)	Description	Thermal Inertia (J m^{-2} K^{-1} $s^{-1/2}$)
< 2	Clay	< 85.648
2 - 75	Silt and Dust	85.648 – 197.126
75 - 425	Fine Sand	197.126 – 293.772
425 - 2000	Medium Sand	293.772 – 419.486
2000 - 4750	Coarse Sand	419.486 – 511.823
4750 - 20000	Gravel	511.823 – 712.390
> 20000	Boulders	> 712.390

For the THEMIS images chosen for study, soil characterization maps were prepared based on Table 5.28. During the dust season, owing to the effect of global wide dust storms coupled with heavy turbulent winds, the surface is covered with fine sand and dust. As the dust season recedes, the fine material is carried away by wind thereby exposing the bedrock and other coarser soil grains, thereby producing a higher value of thermal inertia. This is represented by the maximum % cover of fine grained soil in I49174003 (L_s = 244.49°) which gradually reduces until it becomes almost negligible in I54144002 (L_s = 95.26°) with the surface being covered with coarser soil grains.

Fig 5.37, Fig 5.38, Fig 5.39, Fig 5.40 and Fig 5.41 show the map of surface characteristics generated from the THEMIS thermal inertia images.

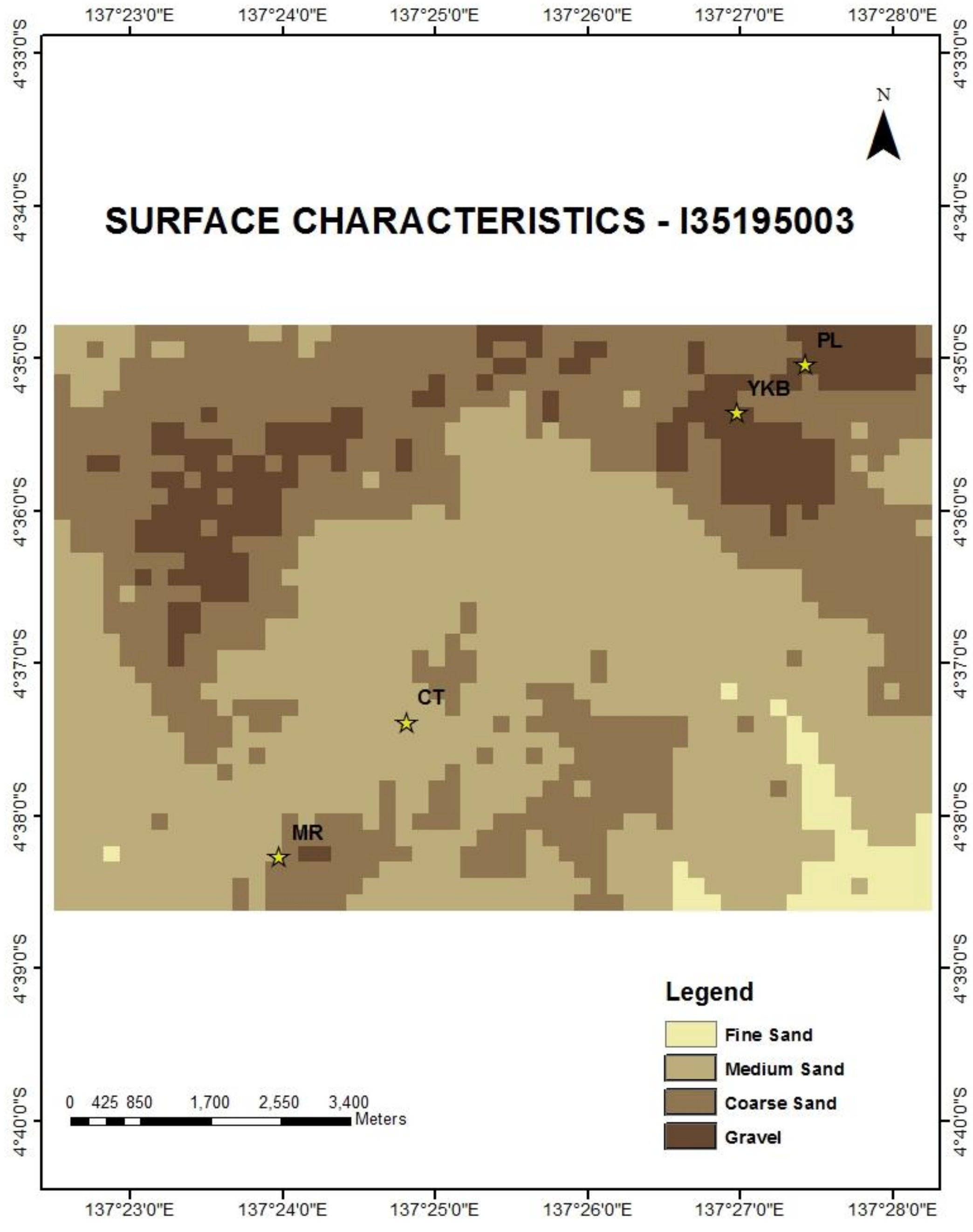

Fig 5.37 Surface Characteristics – I35195003 (L_s = 12.07°)

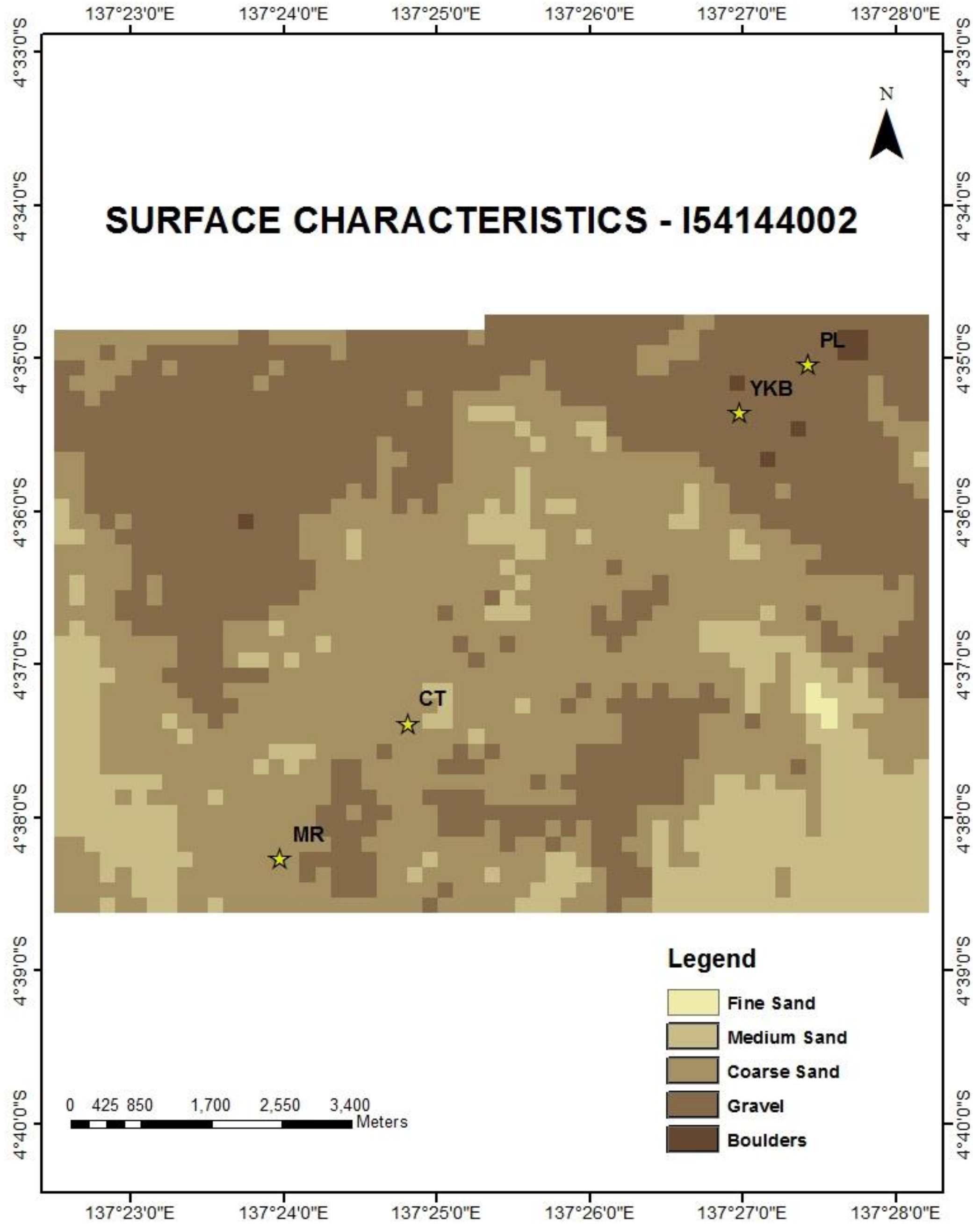

Fig 5.38 Surface Characteristics – I54144002 (L_s = 95.26°)

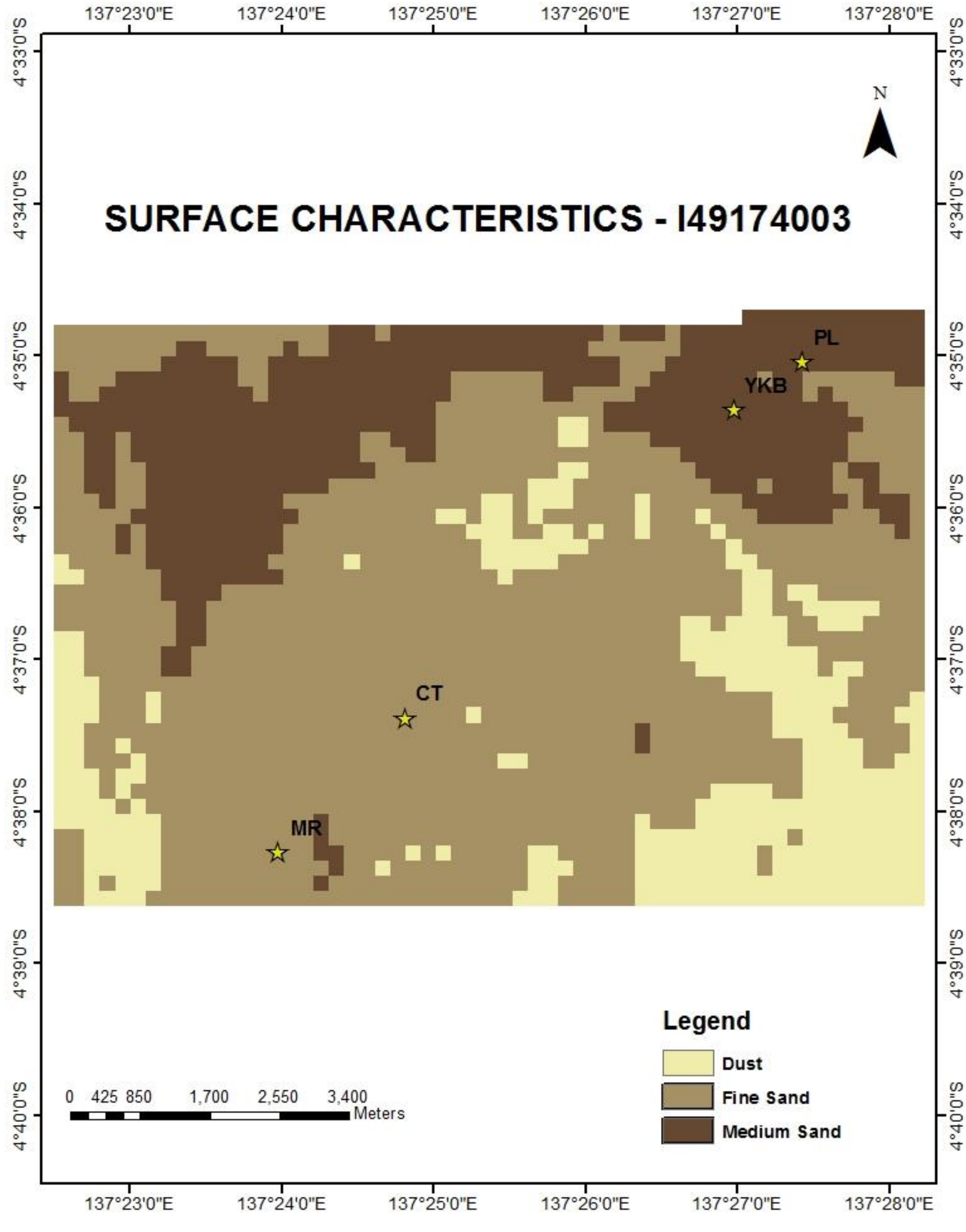

Fig 5.39 Surface Characteristics – I49174003 (L_s = 244.49°)

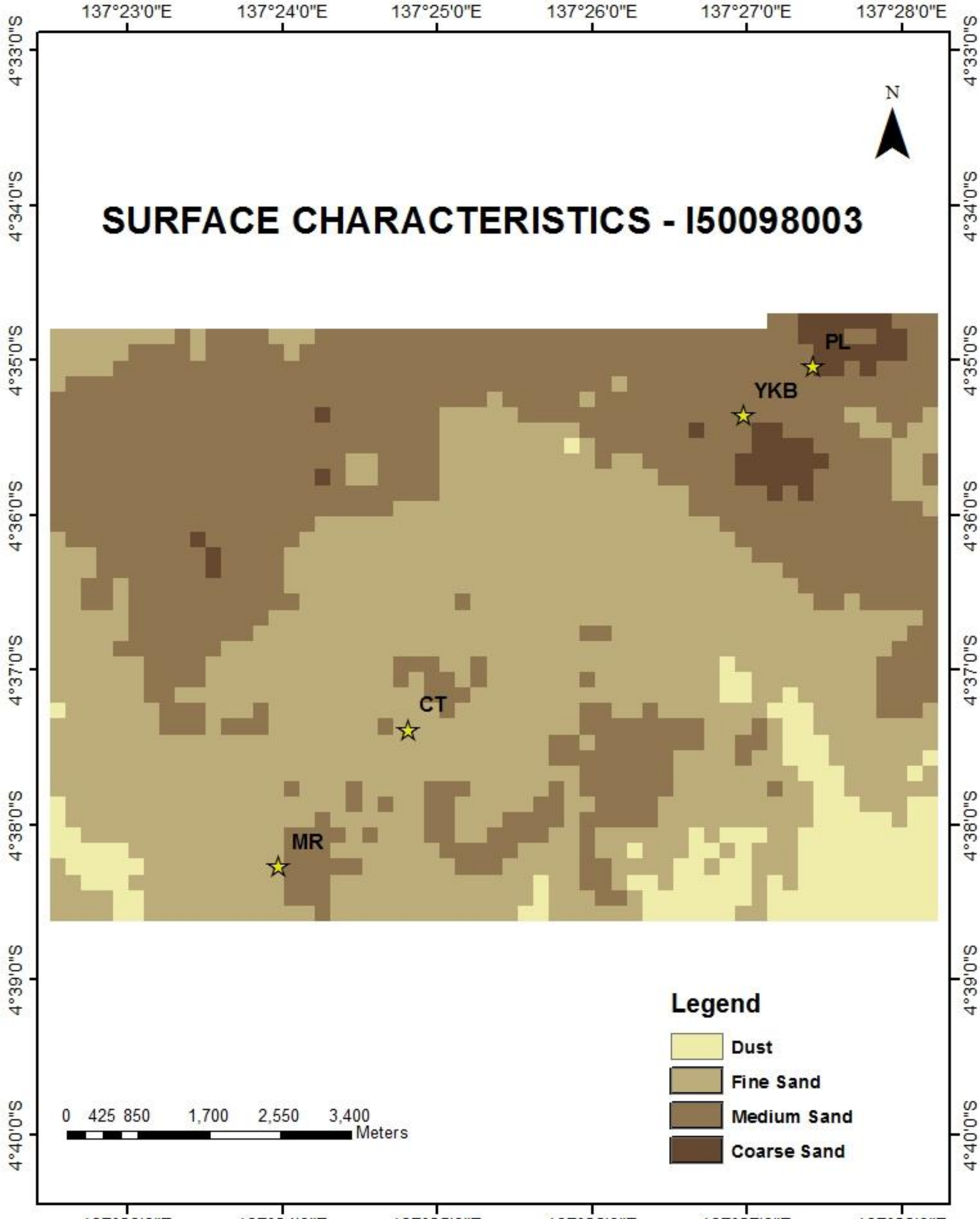

Fig 5.40 Surface Characteristics – I50098003 (L_s = 292.15°)

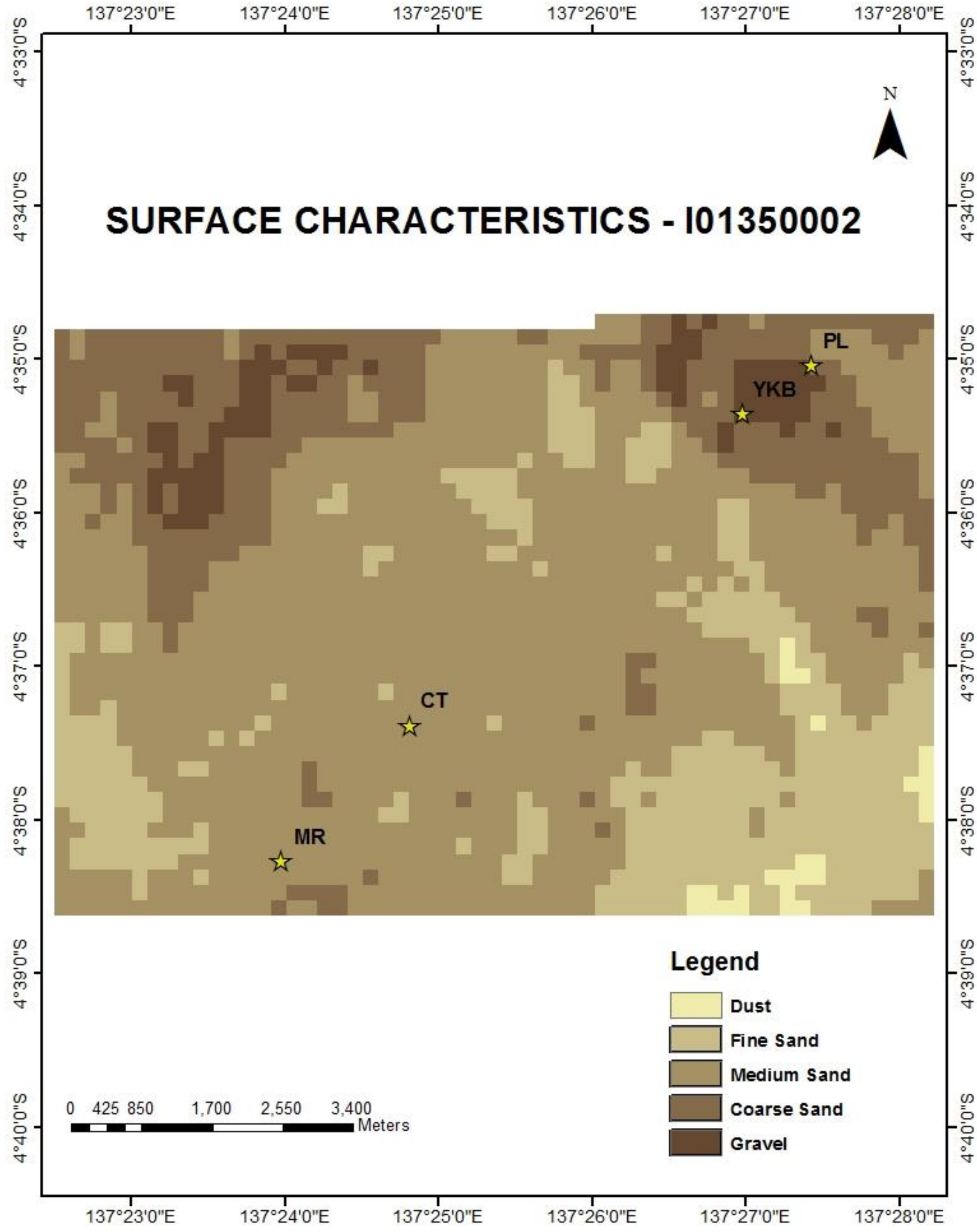

Fig 5.41 Surface Characteristics – I01350002 (L_s = 352.92°)

5.5 Interpretation of thermal inertia regions

5.5.1 Low thermal inertia regions

Low thermal inertia materials insulate the deeper subsurface from surface temperature variations. Lower thermal inertia, indicates smaller grain sizes that effectively fill up the pore space isolating the subsurface from the atmosphere. Large diurnal changes in surface temperature are observed.

Point Lake and the area near Mount Remarkable are found to be low thermal inertia regions.

5.5.2 High thermal inertia regions

High thermal inertia materials provide the warmest subsurface temperatures with utmost the top 20m depth which is the maximum depth of seasonal thermal wave. They effectively transfer the solar insolation through the regolith. Thereby, large diurnal changes in surface temperatures are not observed.

Yellowknife Bay and Coopers Town are found to be high thermal inertia regions.

Chapter 6

CONCLUSIONS

6.1 Surface Energy Fluxes

The estimation of surface energy balance is important to study the energy exchange processes and boundary layer dynamics of any planetary body. It plays a significant role in regulating the near surface thermal behaviour. A seasonal study of the surface energy budget components throws some light on the thermal environment in Mars in different seasons.

Curiosity rover observations enables this study to be performed at high observational accuracy. Measurements from Ground Temperature Sensor, Pressure Sensor, Wind Sensor and Air Temperature Sensor are used to calculate surface energy fluxes in Point Lake, Yellowknife Bay, Coopers Town and Mt. Remarkable regions, which is traversed by the rover in spring, summer, autumn and winter seasons.

Spring is the shortest but hottest season of the Martian year. It experiences the highest magnitude of surface energy fluxes. Average maximum surface and atmospheric temperatures range around 285 K and 260 K respectively. Spring also experiences the highest diurnal variation in temperatures, roughly around 90 K.

Mars is closer to the Sun for most parts of spring when compared to that of summer, thereby causing the atmosphere to emit the highest magnitude of longwave radiation. Spring also marks the onset of global wide dust storms and is the most affected season due to dust absorption, with almost 34% of solar insolation getting trapped in the atmosphere.

Southern summers are at least 10 sols longer than spring. Surface temperatures rise up to around 275 K, almost 5 to 10 K lesser than spring. The diurnal variation of temperature is comparatively lesser in summer i.e. of the order of 75 K. the effect of global wide dust storms gradually recede through the summer and the winds thereby become less turbulent. The percent dust absorption is roughly around 32%, a tad lower than that of spring. With decrease in concentration of dust particles as represented by the lower dust optical depth, the longwave radiation emitted by the atmosphere also reduces and hence, summer has a lower downwelling longwave radiation than that of spring. Lower surface temperatures, however, create an imbalance between solar insolation and emitted surface longwave radiation, thereby allowing greater flux to be stored as ground heat.

Autumn forms the longest season of the Martian year, with the season spanning around 193 sols. The surface temperatures reach a maximum of around 255 K at noon. Autumn also experiences the least diurnal variation in ground temperature roughly around 60 K. The aphelion tends to occur in late autumn and it is seen that the Mars – Sun distance tends to be larger for most part of autumn than winter. This results in autumn experiencing the least upwelling longwave radiation. However, an irregularity in sensible heat flux variation is seen at night time.

Winter in the southern hemisphere spans roughly around 179 sols. It experiences the least diurnal insolation period and is least affected by dust. Temperatures can go as low as 177 K and as high as 265 K., thereby showing an increased diurnal variation of temperature. It is to be noted that Martian atmospheric conditions do not vary much and are somewhat stable in the autumn and winter months, as determined by similar magnitudes of surface energy budget components. Since the magnitude of all fluxes are low, the resulting ground heat storage is also low.

6.2 Thermal Inertia

The one-dimensional heat conduction was solved with appropriate boundary conditions and inputs from Curiosity Ground Temperature Sensor (GTS) to obtain the magnitude of ground heat storage, which was also obtained by solving the surface energy budget. Comparing the two, the thermal inertia of the surface for each sol was obtained at an overall relative uncertainty of 8.55%.

Thermal inertia values were also obtained by running a thermal model on THEMIS night-time images. The values obtained were in very good agreement with Curiosity derived thermal inertia values for the locations chosen for study with an error less than 20%. However, it was observed that thermal inertia is not constant for a particular surface with respect to time, as thought of previously. A plot of the variation of thermal inertia at the four locations shows a sinusoidal variation of thermal inertia peaking at L_s = 95° to 100° and dipping at around L_s = 250° to 270°, roughly near the perihelion of the Martian year.

Thermal inertia from THEMIS was first calculated by Fergason et al. (2006a) at an accuracy of 20% and a precision of about 10 – 15%. He later modified the thermal model adopted and brought down the uncertainty of his computation to 20%. The jENVI scheme used in this study also gives thermal inertia values with an accuracy at par with that of Fergason et al. (2012). Accuracy assessment is done with Curiosity derived thermal inertia where subtle factors like wind turbulence, diurnal variation of dust opacity, pressure and atmospheric temperature measurements are incorporated thereby reducing the degree of uncertainty in thermal inertia estimation.

The thermal inertia generated is used to derive particle sizes to enable surface characterization of the study area using an empirical equation developed by Presley (2002). The thermal inertia ranges for different particle sizes based on USGS soil classification system at an average atmospheric pressure of 6 torr and average volumetric heat capacity of 1.3×10^6 J m^{-3} K^{-1} are calculated and the THEMIS derived thermal inertia images are reclassified based on the ranges obtained. It is seen that the surface is covered by dust and fine sand owing to deposition during the dust seasons which gradually reduces as the global wide dust storms recede.

Derivation of accurate temperature and thermophysical properties helps us understand the past and present geologic processes on the Martian surface through definitive identification of bedrock and recognition of indurated surfaces, unconsolidated fines and dust. Most thermal inertia values are derived using a one dimensional thermal model and the values thus obtained often correlate well with the surface textures and morphology as observed in visible images.

Understanding the spatial distribution and variation of Mars' surface materials is an important task as it can be used to plan site selection for future Mars missions. It can provide a detailed information on engineering requirements for landing instrumentation so as to enable safe landing and take-off (if needed) and selection of sites of scientific interest. (i.e. Places where outcrops are present are more likely to be chosen as landing sites as significant amount of geologic data can be obtained).

6.3 Future Scope

Mars is geologically complex and single-layer models may not truly provide a representation of surface and sub-surface properties. Thermal inertia values derived using one-layer thermal models can commonly produce variations in thermal inertia as large as 300 J m^{-2} K^{-1} $s^{-1/2}$ that are often seasonally repeatable. These variations can lead to ambiguous interpretations of the surface and negatively impacts our ability to confidently interpret the surface properties of Mars.

Subsurface layering and other important physical processes like water-ice cloud formation and near surface winds along with effects of their turbulence could be incorporated into the thermal model so that thermal inertia computations become more trustworthy. Moreover, a global albedo layer derived from THEMIS data at a spatial resolution of 100m could be used to replace the much coarser 3km TES bolometric albedo global mosaic to enhance computational accuracy of thermal inertia.

High resolution thermal inertia estimation is very important and the key to understanding Mars' geology and surface processes effectively.

LIST OF PUBLICATIONS

Papers in International Peer-Reviewed Journals

1. Rangarajan, V.G., Ghosh, M. (2020). Seasonal thermal inertia variations at Gale crater: Role of active surface deposition phenomena. *Icarus 337*, 113499, 1-10. doi.org/10.1016/j.icarus.2019.113499

Related Conference Abstracts

1. Rangarajan, V.G., Ghosh, M. (2019). Localised seasonal dust deposition activity at Gale crater: Inferences from thermal inertia. *50th Lunar and Planetary Science Conference, Woodlands, TX* (abstract #1330).
2. Rangarajan, V.G., Ghosh, M. (2018). Seasonal variations of SEB components over Gale crater, *European Planetary Science Congress 2018, Berlin* (abstract #14) (Poster)

REFERENCES

Journal References

Blake, D.F., Morris, R.V., Kocurek, G., Morrison, S.M., Downs, R.T., Bish, D., Ming, D.W., Edgett, K.S., Rubin, D., Goetz, W., Madsen, M.B., Sullivan, R., Gellert, R., Campbell, I., Treiman, A.H., McLennan, S.M., Yen, A.S., Grotzinger, J., Vaniman, D.T., Chipera, S.J., Achilles, C.N., Rampe, E.B., Sumner, D., Meslin, P.-Y., Maurice, S., Forni, O., Gasnault, O., Fisk, M., Schmidt, M., Mahaffy, P., Leshin, L.A., Glavin, D., Steele, A., Freissinet, C., Navarro-Gonzalez, R., Yingst, R.A., Kah, L.C., Bridges, N., Lewis, K.W., Bristow, T.F., Farmer, J.D., Crisp, J.A., Stolper, E.M., Des Marais, D.J., Sarrazin, P., MSL Science Team, (2013). Curiosity at Gale Crater, Mars: Characterization and Analysis of the Rocknest Sand Shadow. Science, **341 (6153)**, pp. 1–7, doi:10.1126/science.1239505.

Bonan, Gordon, (2002), Surface Energy Fluxes, Ecological Climatology: Concepts and Applications, First Edition, Cambridge University Press, pp. 209-247.

Bose, S., Sinha, R.K., Murty, S.V.S., (2015), Estimation of thermal inertia, sensible heat and latent heat over three landing sites on Mars, 46th Lunar and Planetary Science Conference.

Burch, J.L., Angelopoulos, V. (Eds.), (2009). The THEMIS Mission. Springer New York, New York, NY.

Christensen, P. R., and H. H. Kieffer, (1979). Moderate resolution thermal mapping of Mars: The channel terrain around the Chryse Basin, J. Geophys. Res., **84(B14)**, 8233–8238.

Christensen, P. R., and H. J. Moore, (1992). The Martian surface layer, in Mars, edited by H. H. Kieffer et al., Univ. of Ariz. Press, Tucson, pp. 686–729.

Christensen, P.R., Bandfield, J.L., Hamilton, V.E., Ruff, S.W., Kieffer, H.H., Titus, T.N., Malin, M.C., Morris, R.V., Lane, M.D., Clark, R.L., Jakosky, B. M, Mellon, M. T., Pearl, J. C., Conrath, B. J., Smith, M. D., Clancy, R. T., Kuzmin, R. O., Roush, T., Mehall, G. L., Gorelick, N., Bender, K., Murray, K., Dason, S., Greene, E., Silverman, S., and Greenfield, M., (2001). Mars Global Surveyor

Thermal Emission Spectrometer experiment: investigation description and surface science results. Journal of Geophysical Research: Planets **106**, 23823–23871.

Davy, R., Davis, J.A., Taylor, P.A., Lange, C.F., Weng, W., Whiteway, J., Gunnlaugson, H.P., (2010). Initial analysis of air temperature and related data from the Phoenix MET station and their use in estimating turbulent heat fluxes. Journal of Geophysical Research **115**. E00E13, doi:10.1029/2009JE003444.

Edgett, K. S., and P. R. Christensen, (1991). The particle size of Martian aeolian dunes, J. Geophys. Res., **96**, 22,765–22,776.

Fergason, R. L., (2013), Understanding seasonal variations in thermal inertia on Mars, American Geophysical Union Fall Meeting Abstracts, ISBN: 2013AGUFM.P43C2025F

Fergason, R. L., P. R. Christensen, and H. H. Kieffer (2006a), High-resolution thermal inertia derived from the Thermal Emission Imaging System (THEMIS): Thermal model and applications, J. Geophys. Res., **111**, E12004, doi:10.1029/2006JE002735.

Fergason, R., P. Christensen, M. Golombek, and T. Parker (2012). Surface properties of the Mars Science Laboratory candidate landing sites: Characterization from orbit and predictions, Space Sci. Rev., **170(1–4)**, 739–77

Fergason, R.L., Christensen, P.R., Kieffer, H.H., (2006). High-resolution thermal inertia derived from the Thermal Emission Imaging System (THEMIS): Thermal model and applications, Journal of Geophysical Research: Planets, **111**, pp.1-22.

Forget, Francois, Hourdin, Frédéric, Fournier, Richard, Hourdin, Christophe, Talagrand, Olivier, Collins, Matthew, Lewis, Stephen R., Read, Peter. L., Huot, Jean-Paul, (1999), Improved general circulation models of the Martian atmosphere from the surface to above 80 km, Journal of Geophysical Research, **104**, Issue E10, p.24155-24176, doi:10.1029/1999JE001025

Gómez-Elvira, J., Armiens, C., Castañer, L., Domínguez, M., Genzer, M., Gómez, F., Haberle, R., Harri, A.-M., Jiménez, V., Kahanpää, H., Kowalski, L., Lepinette, A., Martín, J., Martínez-Frías, J., McEwan, I., Mora, L., Moreno, J., Navarro, S., de Pablo, M.A., Peinado, V., Peña, A., Polkko, J., Ramos, M., Renno, N.O., Ricart, J., Richardson, M., Rodríguez-Manfredi, J., Romeral, J., Sebastián, E., Serrano, J., de la Torre Juárez, M., Torres, J., Torrero, F., Urquí, R., Vázquez, L., Velasco, T., Verdasca, J., Zorzano, M.-P., Martín-Torres, J. (2012), REMS: The Environmental Sensor Suite for the Mars Science Laboratory Rover. Space Science Reviews **170**, 583–640.doi:10.1007/s11214-012-9921-1

Haberle, R. M., H. C. Houben, R. Hertenstein, and T. Herdtle (1993), A boundary-layer model for Mars-comparison with Viking lander and entry data, J. Atmos. Sci., **50**, 1544–1559.

Haberle, Robert. M., McKay, C.P., Pollack, J.B., Gwynne, O.E., Atkinson, H.D., Appelbaum, J., Landis, G.A., Zurek, Richard. W., Flood, D.J., (1993), Atmospheric effects on utility of solar power on Mars, NASA Technical Reports, NASA Ames Research Center, 845-885.

Hébrard, E., Listowski, C., Coll, P., Marticorena, B., Bergametti, G., Määttänen, A., Montmessin, F., Forget, F., 2012. An aerodynamic roughness length map derived from extended Martian rock abundance data. Journal of Geophysical Research: Planets **117**, pp.01-26. doi:10.1029/2011JE003942

Jakosky, B. M., and M. T. Mellon, High-resolution thermal inertia mapping of Mars: Sites of exobiological interest, (2001), J. Geophys. Res., **106 (10)**, 23887-23907.

Jakosky, B. M., and P. R. Christensen, (1986). Global duricrust on Mars: Analysis of remote sensing data, J. Geophys. Res., **91(B3)**, 3547– 3560.

Jakosky, B. M., M. T. Mellon, H. H. Kieffer, P. R. Christensen, E. S. Varnes, and S. W. Lee, (2000). The thermal inertia of Mars from the Mars Global Surveyor Thermal Emission Spectrometer, J. Geophys. Res., **105**, 9643–9652.

Jones, E., (2012). Two complementary approaches in refining the search for liquid water and habitable environments on present-day Mars. Ph.D Thesis, Research School of Astronomy and Astrophysics, Australian National University.

Jones, E., Caprarelli, G., Mills, F., Doran, B., Clarke, J., (2014). An Alternative Approach to Mapping Thermophysical Units from Martian Thermal Inertia and

Albedo Data Using a Combination of Unsupervised Classification Techniques. Remote Sensing **6**, 5184–5237. doi:10.3390/rs6065184

Kieffer, H. H., J. S. C. Chase, E. D. Miner, F. D. Palluconi, G. Munch, G. Neugebauer, and T. Z. Martin, (1976). Infrared thermal mapping of the Martian surface and atmosphere: First results, Science, **193**, 780–786.

Kieffer, H. H., J. S. C. Chase, E. Miner, G. Munch, and G. Neugebauer, (1973). Preliminary report on infrared radiometric measurements from Mariner 9 spacecraft, J. Geophys. Res., **78**, 4291–4312.

Kieffer, H. H., T. Z. Martin, A. R. Peterfreund, B. M. Jakosky, E. D. Miner, and F. D. Palluconi, (1977). Thermal and albedo mapping of Mars during the Viking primary mission, J. Geophys. Res., **82**, 4249–4292.

L.W. Ksanfomaliti, V.I. Moroz, (1975) Infrared radiometry from Mars 5, Space Investigations, **13**, 1, 77-83 (in Russian).

Lemoine, F.G., Smith, D.E., Rowlands, D.D., Zuber, M.T., Neumann, G.A., Chinn, D.S., Pavlis, D.E., (2001). An improved solution of the gravity field of Mars (GMM-2B) from Mars Global Surveyor: Journal of Geophysical Research, v. **106**, no. E10, p. 23,359–23,376.

Määttänen, A., and H. Savijärvi (2004), Sensitivity tests with a one-dimensional boundary-layer Mars model, Boundary Layer Meteorology., **113(3)**, pp. 305–320.

Madeleine, J. B., Forget, F., Millour, E., Montabone, L., Wolff, M. J, (2011), Revisiting the radiative impact of dust on Mars using the LMD Global Climate Model, Journal of Geophysical Research, **116**, Issue E11, doi:10.1029/2011JE003855.

Martínez, G.M., Rennó, N., Fischer, E., Borlina, C.S., Hallet, B., de la Torre Juárez, M., Vasavada, A.R., Ramos, M., Hamilton, V., Gomez-Elvira, J., Haberle, R.M., (2014). Surface energy budget and thermal inertia at Gale Crater: Calculations from ground-based measurements, Journal of Geophysical Research: Planets **119**, 1822–1838. doi:10.1002/2014JE004618

Meadows and Crisp, (1996), Ground-based near-infrared observations of the Venus night side: The thermal structure and water abundance near the surface, Journal of Geophysical Research., **101**, 4595–4622.

Mellon, M. T., B. M. Jakosky, H. H. Kieffer, and P. R. Christensen, (2000). High resolution thermal inertia mapping from the Mars Global Surveyor Thermal Emission Spectrometer, Icarus, **148**, 437–455.

Mena-Fernandez, S., Xie, H., (2005), Understanding the Olympus Mons and Valles Marineris using THEMIS imagery, 26th Lunar and Planetary Science Conference.

Millour, E., Forget, F., Spiga, A., Navarro, T., Madeleine, J.B., Montabone, L., Pottier, A., Lefevre, F., Montmessin, F., Chaufray, J.Y., Lopez-Valverde, Gonzalez-Galindo, F., Lewis, C.F., Read, P.L., Huot, J.P., Desjean, M.C., (2015), The Mars Climate Database (MCD version 5.2), European Planetary Science Congress, EPSC Abstracts, Vol **10**, EPSC2015-438

Möhlmann, D. (2004), Water in the upper Martian surface at mid-and low-latitudes: Presence, state, and consequences, Icarus, **168(2)**, 318–323.

Moroz, V.I., (1976). The atmosphere of Mars. Space Science Reviews, **19**, pp.763-843, doi:10.1007/BF00173706

Moroz, V.I., Ksanfomaliti, L.V., (1972). Preliminary results of astrophysical observations of Mars from Mars-3. Icarus, **17**, 408–422.

Neugebauer, G., Miinch, G., Kieffer, H., Chase, S.C., Jr., Miner, E., (1971). Mariner 1969 Infrared Radiometer Results: Temperatures and Thermal Properties of the Martian Surface. The Astronomical Journal, **76**, 719.

Neumann, G. A., D. E. Smith, and M. T. Zuber, (2003). Two Mars years of clouds detected by the Mars Orbiter Laser Altimeter, J. Geophys. Res., **108(E4)**, 5023, doi:10.1029/2002JE001849.

Neumann, G.A., Rowlands, D.D., Lemoine, F.G., Smith, D.E., and Zuber, M.T., (2001). Crossover analysis of Mars Orbiter Laser Altimeter data: Journal of Geophysical Research, v. **106**, no. E10, p. 23,753–23,768.

Presley, M. A. and Christensen, P. R. (1997). Thermal conductivity measurements of particulate materials 2. Results, Journal of Geophysical Research E: Planets, **102(E3)**, 96JE03303, pp. 6551-6566.

Presley, M. A., (1995) Thermal conductivity measurements of particulate materials: Implications for surficial units on Mars, Ph.D. dissertation, Ariz. State Univ., Tempe.

Presley, M. A., (2002). What can Thermal Inertia do for you? 33rd Lunar and Planetary Science Conference.

Presley, M. A., and R. E. Arvidson, (1988). Nature and origin of materials exposed in the Oxia Palus-Western Arabia-Sinus Meridiani region, Mars, Icarus, **75**, 499–517.

Putzig, N. E., M. T. Mellon, K. A. Kretke, and R. E. Arvidson (2005), Global thermal inertia and surface properties of Mars from the MGS mapping mission, Icarus, **173**, 325–341.

Putzig, N., Mellon, M., (2007). Apparent thermal inertia and the surface heterogeneity of Mars. Icarus **191**, 68–94.

Savijärvi and Määttänen., (2010). Boundary-layer simulations for the Mars Phoenix lander site, Quarterly Journal of the Royal Meteorological Society **136**, 1497–1505, doi:10.1002/qj.650

Savijärvi, H. (1995), Mars boundary layer modeling: Diurnal moisture cycle and soil properties at the Viking lander 1 site, Icarus, **117(1)**, 120–127.

Savijärvi, H. (1999), A model study of the atmospheric boundary layer in the Mars Pathfinder lander conditions, Q. J. R. Meteorol. Soc., **125(554)**, 483–493.

Savijärvi, H., Crisp, D., Harri, A.-M., (2005). Effects of CO_2 and dust on present-day solar radiation and climate on Mars, Quarterly Journal of the Royal Meteorological Society **131**, 2907–2922. doi:10.1256/qj.04.09

Savijärvi, H., Kauhanen, J., (2008), Surface and boundary-layer modelling for the Mars Exploration Rover sites, Quarterly Journal of the Royal Meteorological Society **134**, 635–641, doi:10.1002/qj.232.

Selene, (2005), “Analysing temperature and mineral composition of Olympus Mons and Valles Marineris”, Project dissertation at University of Texas at San Antonio

Smith, D.E., Zuber, M.T., Frey, H.V., Garvin, J.B., Head, J.W., Muhleman, D.O., Pettengill, G.H., Phillips, R.J., Solomon, S.C., Zwally, H.J., Banerdt, W.B., Duxbury, T.C., Golombek, M.P., Lemoine, F.G., Neumann, G.A., Rowlands, D.D., Aharonson, Oded, Ford, P.G., Ivanov, A.B., Johnson, C.L., McGovern,P.J., Abshire, J.B., Afzal, R.S., and Sun, Xiaoli, (2001). Mars Orbiter Laser Altimeter—Experiment summary after the first year of global mapping of Mars: Journal of Geophysical Research, v. **106**, no. E10, p. 23,689–23,722.

Stull, Roland, (1988), An Introduction to Boundary Layer Meteorology, Kluwer Academic Publishers, pp. 177–180, ISBN 978-90-277-2769-5.

Sutton, Jordan. L., Leovy, C. B., Tillman, J. E., (1978), Diurnal Variations of the Martian surface layer: Meteorological parameters during the first 45 sols at two Viking lander sites, Journal of Atmospheric Sciences, Vol **35**, pp. 2346-2355.

V I Moroz, L V Ksanfomality, A É Nadzhip, ""Mars-3": Astrophysical Studies of the Lower Atmosphere and the Surface of the Planet", SOV PHYS USPEKHI, 1974, **16** (5), 741–742, doi: https://doi.org/10.1070/PU1974v016n05ABEH004160

Vasavada, A.R., Piqueux, S., Lewis, K.W., Lemmon, M.T., Smith, M.D., (2017). Thermophysical properties along Curiosity’s traverse in Gale crater, Mars, derived from the REMS ground temperature sensor. Icarus **284**, 372–386.

Vicente-Retortillo, Á., Valero, F., Vázquez, L., Martínez, G.M., (2015), A model to calculate solar radiation fluxes on the Martian surface, Journal of Space Weather and Space Climate **5**, A33. doi:10.1051/swsc/2015035

Wang, J., Bras, R.L., Sivandran, G., Knox, R.G., (2010). A simple method for the estimation of thermal inertia, Geophysical Research Letters Vol.**37**.

Wentworth, C. K., (1922). A Scale of Grade and Class Terms for Clastic Sediments. Journal of Geology **30(5)**, pp. 377-392

Wessel, Paul, and Smith, W.H.F., (1998). New, improved version of Generic Mapping Tools released: Eos, Transactions of the American Geophysical Union, Vol. **79**, No. 47, p. 579.

Zimbelman, J. R., and H. H. Kieffer, (1979). Thermal mapping of the northern equatorial and temperate latitudes of Mars, J. Geophys. Res., **84**, 8239–8251.

Webpage References

Curiosity (rover), last updated on 14 December 2016 (**https://en.wikipedia.org/wiki/Curiosity_(rover)**)

Curiosity Rover Drive Log, last updated on 22 April 2017, (**http://curiosityrover.com/tracking/drivelog.html**)

Gale (Crater), last updated on 18 March 2017 (**https://en.wikipedia.org/wiki/ Gale_(crater)**)

Geocentric Ephemeris for the Sun, Moon and Planets courtesy of Fred Espenak - 2012, 2013 and 2014. (**http://www.astropixels.com/ephemeris/planets/mars2012.htm**)

Lunar and Planetary Science Laboratory, High Resolution Imaging Science Experiment, last updated 2017. (**http://www.uahirise.org/**)

Mars Climate Database, Martian Seasons and Solar Longitude, last updated 2017 (**http://www-mars.lmd.jussieu.fr/mars/time/solar_longitude.html**)

Mars Space Facts, last updated 2017 (**http://space-facts.com/mars/**)

Volumetric Heat Capacity, last updated on 11 February 2017 (**https://en.wikipedia.org/wiki/Volumetric_heat_capacity#Thermal_inertia)**